Understanding and tuning sliding friction

Liefferink, R.W.

Publication date
2021

Document Version
Final published version

Citation for published version (APA):
Liefferink, R. W. (2021). *Understanding and tuning sliding friction*. [Thesis, fully internal, Universiteit van Amsterdam].

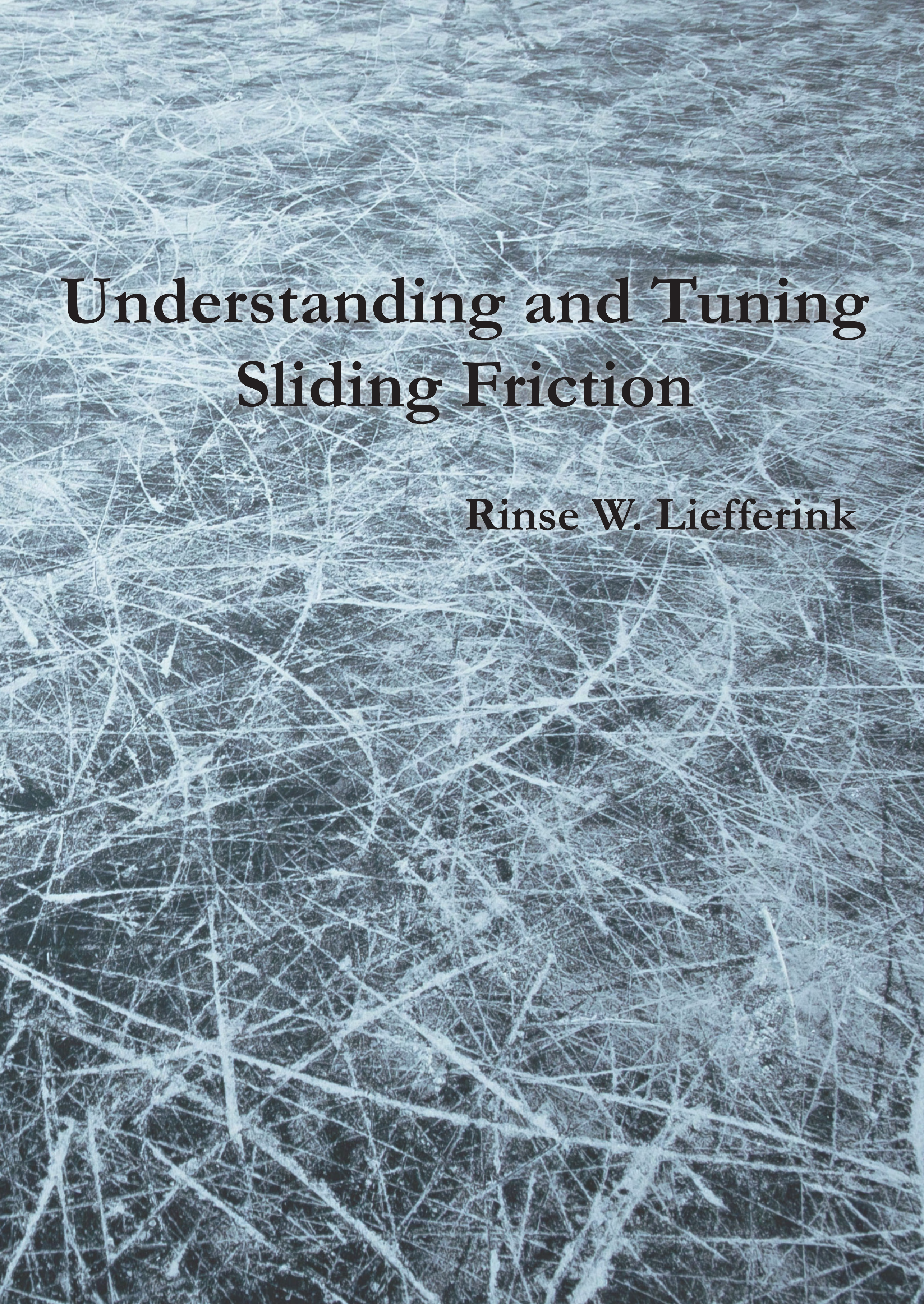

Understanding and Tuning Sliding Friction

Rinse W. Liefferink

Understanding and Tuning Sliding Friction

Rinse W. Liefferink

Understanding and Tuning Sliding Friction

ACADEMISCH PROEFSCHRIFT

ter verkrijging van de graad van doctor
aan de Universiteit van Amsterdam
op gezag van de Rector Magnificus
prof. dr. ir. K.I.J. Maex
ten overstaan van een door het College voor Promoties ingestelde commissie,
in het openbaar te verdedigen in de Agnietenkapel
op donderdag 3 juni 2021, te 16.00 uur

door

Rinse Willem Liefferink

geboren te Nijmegen

Promotiecommissie

Promotor:	prof. dr. D. Bonn	Universiteit van Amsterdam
Copromotores:	dr. C.J.M. Coulais	Universiteit van Amsterdam
	dr. B.A. Weber	Universiteit van Amsterdam
Overige leden:	prof. dr. S. Woutersen	Universiteit van Amsterdam
	prof. dr. J.W.M. Frenken	Universiteit van Amsterdam
	dr. E. Lerner	Universiteit van Amsterdam
	prof. dr. E.H.G. Backus	Universiteit van Amsterdam
	dr. A. Fall	Laboratoire Navier, CNRS
	prof. dr. L. Bocquet	École Normale Supérieure, Paris
	prof. dr. J.F. Molinari	École Polytechnique Fédérale de Lausanne

Faculteit der Natuurwetenschappen, Wiskunde en Informatica

UNIVERSITY OF AMSTERDAM

Het onderzoek gepresenteerd in dit proefschrift is uitgevoerd bij:
Soft Matter Group, Van der Waals-Zeeman Institute/Institute of Physics, Universiteit van Amsterdam, Science Park – 1098 XH Amsterdam.
Het hier beschreven onderzoek/de uitgave van dit proefschrift werd mede mogelijk gemaakt door steun van Royal Dutch Shell, FundRef PT 67354

ISBN: 978-94-6419-198-1

Cover design: Vera van Winkelen & Rinse Liefferink
Photo from: pip / photocase.com

Electronic version of this thesis can be found at http://dare.uva.nl

The author can be reached at: rinseliefferink@gmail.com

Contents

CHAPTER 1

Introduction

1.1 From sliding a bookcase over the floor to skating on ice: What controls the sliding friction?

When one tries to slide a bookcase over the floor, a force prevents it from moving. No matter what — and in which direction — it will act to hold the bookcase in place. The resistance to sliding, *the friction force*, can be overcome if one push hard enough and, obviously, it would have helped if one had emptied the bookcase first.

Although friction is a part of everyday life, the physics behind it is still not properly understood. For example, is the force required to slide a bookcase over the floor dependent on the number of legs? Intuitively we could argue that with more legs, the area within which friction is generated has been increased. This is not true, sliding a bookcase on its side, or with eight furniture legs instead of four, results in a similar friction force. While the contact area, i.e., the number of furniture legs, may not directly influence the friction, the interface does: the geometry of the surfaces and its roughness control the friction force. Sliding furniture with pointy legs over a floor with little irregularities can be very difficult and, horribly, can lead to scratches on the floor. Furthermore, the type of floor strongly influences the experienced resistance; a wooden, tile, or carpet flooring, or — why not? — an icy surface influence how hard one has to push.

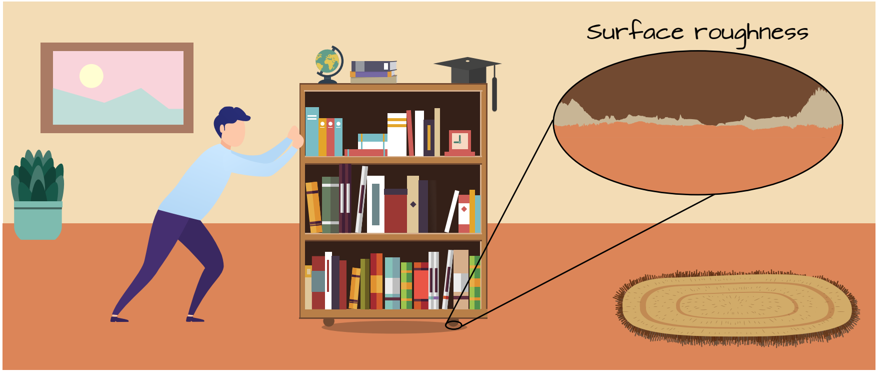

Figure 1.1: How to slide a bookcase over the floor?

In this thesis, we make a contribution to answering the seemingly simple question, 'What controls sliding friction?' We aim to bridge the gap between macroscopic observed sliding friction and the underlying microscopic behaviour at the interface between the sliding surfaces (the 'interface geometry'). We use a combination of experimental and numerical techniques and focus on the sliding friction for three very different types of surfaces, namely (wet) sand, ice, and a collection of artificial surfaces whose geometry we can precisely control. (i) We perform sliding friction experiments on partially water-saturated sand. Adding water to sand strongly influences the mechanical behaviour of this granular material; a sandcastle can be constructed only with sand to which some, but not too much, water is added to. We show that, together with the slider geometry, the water fraction determines how hard it is to slide over the sand and how deep the trace that is left after passing is. (ii) In addition, we measure the slipperiness of ice and discuss why this surface is extraordinary slippery. We 'skate' on a miniature ice skating rink and measure the sliding friction on ice as a function of temperature, contact pressure, and speed. In our experiments, we show that ice is not always slippery: The slipperiness of ice can be suppressed by increasing the contact pressure, set by the geometry of skate and its surface roughness, or lowering the temperature. (iii) In the final chapter of the thesis, we explore how one can tune the sliding friction using geometrically controlled surfaces. We demonstrated that well-designed surface roughness and control of the (mis)match the surface roughness on the sliders allows one to vary the friction force by more than an order of magnitude.

1.2 Sliding friction in the past

Overcoming the resistance to sliding when moving objects relative to each other, was — and still is — a costly problem; it has been estimated that a third of the world energy consumption is spent on friction and wear [1]. The study of sliding friction, wear, and lubrication is called tribology, this term was coined in the 20th century [2]. The prefix *tribo-* is Greek for rubbing; the field was initially defined as "the science and technology of interacting surfaces in relative motion and of related subjects and practices." Although this definition came much later, the applications or problems of tribology are ancient. A famous example comes from ancient Egypt. Various tomb drawings demonstrate how the ancient Egyptians transported large stones and even complete statues on sledges pulled by many men [3–5]. Intriguingly, in one of these drawings, one person pours water onto the sandy surface in front of the sledge (see Fig. 4.1 in Chapter 4 for one of these tomb drawings). Water may influence the friction between a sledge and the sand. This is like walking on the beach: slightly wet sand makes the walk easier than dry sand. The addition of some — but not too much — water to sand can therefore make the transportation of statues over sand easier [6]. The tomb drawings suggest, although still widely debated [5,7–9], that the Egyptians already made use of this knowledge and can be considered as some of the earliest tribologists.

The moving of large stones and colossal cultural statues has been reported frequently [10]. Many (tribological) solutions have been developed and applied, ranging from simple manpower and a sledge to the use of log rollers, horsepower, and spiked-wheeled cars. Another creative solution was developed in the 15th century: Chinese builders transported a massive stone over a distance of 70 km using an artificial ice road to build the famous Forbidden City [11]. This imperial palace complex in Beijing was constructed between 1406 and 1420 and was in use by many emperors up to 1912. A quarried stone with a weight of 300 tons was heaved to the Forbidden City using rolling logs in summer. In winter, workers poured water

Figure 1.2: *'The Large Stone Carving'* (left) is placed as a ramp flanked by stairs towards the Hall of Preserving Harmony, *Baohe dian* (right top). The heaviest stone of the Forbidden City is 16 m by 3 m by 1.7 m with a weight of 200 tons [10]. It originally weighted roughly 300 tons; when it was re-hewn in 1761, its weight was reduced to about 200 tons. The chiselled ornamentations on the stone include the dragon (right bottom), the symbol of celestial power. The pictures are from www.dpm.org.cn.

along the transportation road to create a slippery ice track and slide the huge block along the ice. Once the rock was in place, it formed a ramp flanked by stairs towards the Hall of Preserving Harmony (*Baohe dian*) as can be seen in Figure 1.2. In Ming dynasty times, the emperor was brought from his residence, the Palace of Heavenly Purity in the inner court, to this hall in the outer court before attending a grand ritual or ceremony to change into ceremonial robes. It has been argued that the Chinese builders preferred wooden logs and slippery ice as the load was too heavy for wheeled carriages [11].

1.3 The laws of friction, a macroscopic approach

Leonardo da Vinci (1452–1519) can be seen as the father of modern tribology. In his notebooks an incredible amount of tribological studies are discussed: He reported studies in friction, wear, and bearings which include a full circular ball bearing design [12, 13]. In his sliding experiments, a block is horizontally pulled over a substrate with the use of weights, a connecting string, and a pulley (see Fig. 1.3). The observations of da Vinci, however, remained unpublished in his notebooks and were only re-discovered in the 1960s [14]. Independently, 200 years later Guillaume Amontons arrived at similar conclusions for the sliding friction of dry solids [15]. After the contribution of Charles-Augustin de Coulomb in 1785, their findings can be summarised in three laws:

- The friction force is directly proportional to the normal force
- Friction is independent of the apparent area of contact between the two surfaces
- Dynamic friction is independent of the sliding speed

The laws of friction were the result of simple sliding experiments with wooden blocks: The friction doubles if two identical blocks are stacked, the friction is independent of the face of the block on which it is sliding, and friction is not affected by the sliding speed. These empirical laws are obeyed in most dry sliding systems and, due to the proportionality of the friction force F to the normal force N, allows the definition of the *friction coefficient*:

$$\mu := \frac{F}{N}\,, \tag{1.1}$$

The friction coefficient is often quantified for surfaces sliding over each other and enables prediction of the friction force. When the coefficient of friction is known, the friction force can be calculated if the normal force is measured.

Da Vinci did derive Amontons' laws based on his experiments performed two centuries before Amontons work. However, he had a different third law of friction; he stated that the resistance to sliding has a constant value of $\mu = 0.25$. This finding is quite striking as some materials are certainly more slippery than others: Steel on ice has a friction coefficient near zero, whereas a rubber shoe on the pavement has good grip due to a high friction coefficient. The fascinating inconsistency between da Vinci's results and modern tribology has been resolved by Dowson et al. [16]. They re-performed da Vinci's experiments roughly 500 years later, including an attempt of recreating the sliding setup. For various objects they quantified the material-dependent friction coefficient μ. Only when they performed their experiments with dry wood that were handled and sullied by hand, the performed measurements indeed correspond to a friction coefficient of roughly 0.25. Dowson et al. wrote: [the

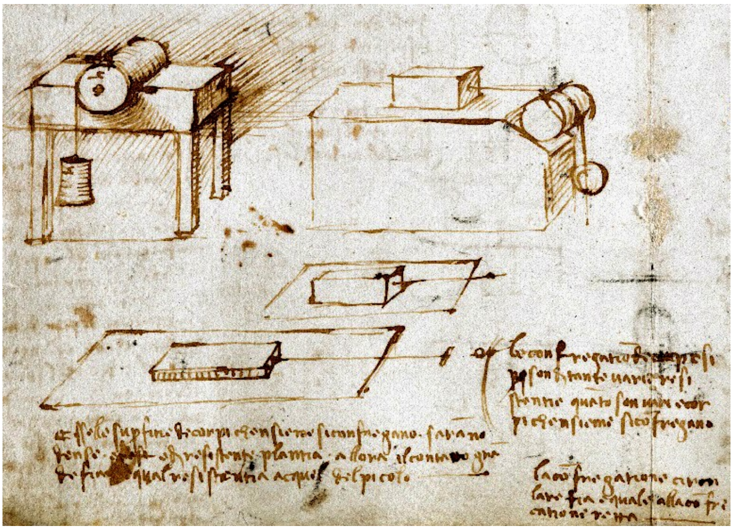

Figure 1.3: Original sketches from Leonardo da Vinci for his experiments on friction that were reported in his notebooks *Codex Atlanticus* and *Codex Arundel* [12, 13, 17]. In the right top, he measured sliding friction between a block and a flat surface with the use of weights and a pulley system where he calibrated how much weight is necessary to maintain the block sliding at a constant speed. On the bottom, the sliding of wooden blocks with various widths and lengths is illustrated. Da Vinci also reported on (lubricated) rolling friction: In the left top, a cylinder is illustrated that is placed in a shaped cavity and is rotated with weights.

sliding surfaces] “were intentionally exposed to fingerprint oils and airborne dust, resulting in a ‘sullied’ environment.” A small layer of oil (i.e., finger fat) and dust lubricates the wood-on-wood sliding experiments. “Such a procedure of sample preparation is entirely reasonable for the time period and suggests an active, dusty, and dynamic laboratory environment.” [16]. Friction, therefore, often depends on the experimental conditions. It also teaches us that modern lab experiments, experiments performed in a clean and well-controlled environment, cannot always be directly converted to real-life situations.

1.4 Towards a microscopic picture of friction

1.4.1 The real contact area

In order to understand sliding friction in more detail, there is a need to bridge the gap between the macroscopic and the microscopic scales. One of the intriguing questions, raised after performing sliding experiments on the macroscale, is why the sliding friction is independent of the contact area? Intuitively, one could argue that when the contact area increases, the friction should increase proportionally. The key ingredient here is surface roughness. Although the friction force is independent of the apparent contact area, i.e., the area that appears to be in contact when surface roughness is not considered, it is in fact proportional to the so-called Real Contact Area (RCA). The irregularities of the surfaces touch and push on each other and the formed real contact area is directly proportional to both the normal and the friction force. The friction, therefore, is the result of shearing the microscopic contact points over each other; see Figure 1.1 for an illustration of the formed contact between a furniture leg and the floor.

The real contact area was quantified by Bowden and Tabor in the early twentieth century [18,19]. They performed loading experiments and measured the electrical conductivity at the metal-metal interface. They observed that just a fraction of the apparent contact actually touches. Bowden described this in a BBC radio program (1950): “... putting two solids together is rather like turning Switzerland upside down and standing it on Austria – their area of intimate contact will be small.” [20]. The performed tests also demonstrated that the real contact area, the ‘mountains’ of the surfaces in contact, at the metal-metal interface was proportional to the load pressing the two surfaces together. As the real contact area is proportional to the load (RCA $\propto N$) and the friction force needed to shear the microscopic contact points is also proportional to the real contact area ($F \propto \mathrm{RCA}$), they immediately arrived at Amontons' laws: The friction force increases linearly with the normal force and is independent of the contact area ($F \propto N$).

1.4.2 Contact mechanics

The growth of the real contact area with the normal force does depend largely on the surface materials and their roughness. The study of contact mechanics focuses on the deformation of solids when they are loaded. The metal-on-metal loading experiment from Bowden and Tabor emphasised the influence of plasticity. The rough surfaces are brought into contact and, consequently, first the highest 'mountains' will touch and experience a large contact pressure. When this contact pressure exceeds the yield stress of the material, the highest 'mountains', called asperities, will irreversibly deform. The asperities in contact will flatten out, and more contact spots between the asperities of the surfaces will form. The increased real contact area lowers the contact pressure until the yield stress is not exceeded anymore and the surfaces are in mechanical equilibrium. The experimental results led Bowden and Tabor to conclude that, for a rough-on-rough contact, the pressure is constant at the yield stress and, consequently, the real contact area increases proportionally with the normal force [19].

The Bowden-Tabor theory was, however, conflicting with elastic Hertz theory which describes that for a sphere touching a flat surface the real contact area grows sublinearly with the loading force and, therefore, is inconsistent with Amontons' laws. Hertz developed a theory in 1882 that describes the contact formation between smooth and non-adhering elastic surfaces [21, 22]. He proposed that surfaces reversibly deform as a rubber ball pressed onto a table: The curved elastic surface is flattened out and, after unloading, relaxes back to its initial form. Many theories are introduced to avoid some of the assumptions inherent to Hertz theory, which include surface roughness, adhesion, and plasticity. Greenwood and Williamson did, for example, apply Hertz theory on the asperity-scale [23]. They approximated a rough surface as a distribution of spherical asperities that all individually deform based on Hertz theory. They found that under these assumptions, the real contact area is proportional to the applied load [22]. However, it is widely accepted — including by Greenwood himself [24] — that modelling the real contact area with the macroscopic (non-adhesive) Hertzian theory on the asperity-level is limited. The surface height variations on the nanoscale, the asperities on the asperities [25], and the influence of plasticity limit the application and highlight the influence of the broad domain of length scales of the surface roughness. The real contact area must be determined for surface height variations in the range from the atomic level up to the macroscopic size of the slider geometry [26].

Many authors have contributed to the field of contact mechanics in an attempt to include all realistic effects: elasticity, plasticity, and adhesion [27–32]. Recently, the pioneering work of Persson (2002) provided an alternative model that considers the fractal nature of surfaces — the asperities on the asperities — and also predicts a linear dependence between the real contact area and the normal force [33]. Furthermore, experimental techniques, such as (frustrated) total internal reflection microscopy [34, 35] and fluorescence microscopy [36, 37] allow surpassing the existing limitations and enable quantifying the real contact area which, normally, is difficult to measure as it is buried between the two loaded surfaces. We can attempt to summarise saying that elastic, elastoplastic or plastic behaviour in the micro-contacts can largely depend on the normal force while at the macroscopic level the approximation of a linear increase of the contact area with normal force is regularly observed for many surfaces of practical interest.

1.4.3 Shearing the surfaces

The contact mechanics, the deformation of solids in contact, teaches us that the real contact area at the sliding interface strongly depends on the surface topography [38]. The friction force therefore results from the resistance to slide these loaded asperities over each other. The development of the atomic force microscope made it possible to study sliding friction at the atomic scale; one surface is pushed with a cantilever on another surface where the deflection of the cantilever, which acts as a spring, can be converted to the exerted contact forces [39]. These sliding experiments serve as a model experiment for single asperity contact where the measured friction force as a function of the sliding distance displays the atomic-scale periodicity [40]. Various studies emphasise the influence of energy dissipation, phonon-phonon interaction, thermal vibrations and, in particular, adhesive interactions on the sliding friction [40–42]. The adhesive interactions between loaded asperities results in ‘glueing’ them together, e.g., by the van der Waals forces [33]. Adhesion can increase the sliding friction significantly; a smooth elastic rubber can reach a friction coefficient of around 2 [43]. In contrast, a lack of adhesive friction can result in extremely low friction. This so-called structural lubricity can be achieved for periodic surfaces where, based on their commensurability at the nanoscale, the real contact area and the resulting number of adhesive bonds is low [44]. The adhesive friction force is therefore dependent on the interface geometry.

In addition to adhesive friction, the resistance to sliding can also be the result of plastic deformation. The shear stress on rough surfaces can result in plastic flow; the yield stress of the softest material is exceeded and will irreversibly flow. This plastic deformation can occur on the atomic-level — wearing off atom by atom — or in larger chunks resulting in the formation of debris particles [45–49]. The latter can result in abrasive wear: scratching the floor when sliding a bookcase over it, or the gradual reduction of the tread on a tire in contact with the road. Plastic deformation is not limited to asperity interactions, it can also occur on the scale of the slider geometry. A rigid slider can, when loaded on a softer surface, indents the surface and plough through it laterally. Bowden, Moore, and Tabor performed sliding experiments with metals and wrote: “It is suggested that in general the frictional force between clean metal surfaces is made up of two parts. The first is the force required to shear the metallic junctions formed between the surfaces; the second is the ploughing force required to displace the softer metal from the path of the harder.” [45]. Plastic deformation of the surfaces does therefore occur on various length scales. The surface topography, together with loading force and the hardness of the materials, controls the wear track and, subsequently, the ploughing force.

1.5 Understanding friction from the microscopic to the macroscopic scale

The macroscopic approach, first described by Leonardo da Vinci, has shown us that the sliding friction between two surfaces increases proportionally to the normal force and is independent of the apparent area of contact. The friction coefficient can be defined as the ratio of the friction force and normal force. A microscopic approach teaches us that the microscopic surface topography, the irregularities of the surfaces, determine where the surfaces make contact when loaded and where the consequent sliding friction occurs. The macroscopic measured friction therefore results from shearing the microscopic contact points between the surfaces over each other.

In this thesis, we aim to bridge the gap between the macroscopically observed sliding friction and the underlying microscopic behaviour. We measured the sliding friction at the macroscopic scale and combine mechanical tests, surface topography quantification, and contact mechanics calculations, to connect our large-scale observations to the underlying microscale mechanisms. We focus on the influence of interface topography, the geometry of the surfaces and their surface roughness, for three very different types of surfaces.

(i) We discuss the sliding friction on partially water-saturated granular materials, specifically sand. Sand is a loose material that consists of a mixture of grains with sizes that can vary from a micrometre up to a few millimetres. Adding a small quantity of water to sand strongly influences the mechanical behaviour. The formation of capillary bridges between the grains results in a capillary pressure causing an attractive force between the grains: a cohesive network of grains that are connected with liquid bridges is formed [50]. However, adding too much water to sand results in coalescence of the capillary bridges and thereby decreases the strong binding between the grains. The influence of pouring water onto sand — from a dry pile of sand up to a muddy surface — has been observed for the stiffness of the mixture [6,51]. The elastic shear modulus varies nonmonotonically with the addition of water and has an optimum when some, but not too much, water is added. Here, we question the role of the slider geometry dragged over wet sand, to aim for a deeper understanding of the sliding friction.

(ii) We discuss the sliding friction on ice that, as any ice skater has observed, is a surface that is extraordinary slippery. The question *why* ice is so slippery has been debated for more than 150 years. Furthermore, ice friction is generated by an interface that includes many discrete contact points, due to the surface irregularities on the ice and slider. Understanding how this extended interface impacts the slipperiness of ice remains difficult to address because the interface is buried between two bulk materials. With the use of sliding experiments and contact mechanics calculations, we aim for a deeper understanding on how the surface irregularities of the surfaces shear over each other.

(iii) We explore how we can tune the sliding friction with geometrically controlled surfaces. Even in everyday scenarios, one can observe that two smooth surfaces slide more easily over each other than two rough ones. However, at the microscopic scale the opposite can be observed: periodic roughness can decrease the sliding friction drastically [44]. The commensurability of periodic nanoscale surfaces can result in a low amount of adhesive interaction and, therefore, direct variation of the commensurability enables the sliding friction to be controlled [52,53]. Here, we question the influence of macroscopic periodic roughness and their commensurability on the sliding friction.

1.6 Scope of this thesis

In this thesis, we discuss the macroscopic observed sliding friction and the underlying microscopic behaviour. First, in **Chapter 2**, we discuss the experimental and numerical techniques that are used in the main research chapters (Chapters 3 to 6). We discuss the two tribometers used to perform sliding tests, as well as the quantification of penetration hardness, the characterisation of surface topography, and the numerical techniques used to calculate the contact mechanics.

In **Chapter 3** we discuss the ploughing through dry and wet sand. We perform experiments where we drag a hemisphere over wetted sand and measure the friction as a function of the water volume fraction. The slider sinks into the water-sand mixture and, consequently, ploughs through the sand which leaves a deep trace after its passage. The measured friction is greatly impacted by both the water fraction in sand and the chosen geometry: The water fraction controls the hardness of the water-sand mixture and the geometry of the slider, together with its load, controls the contact pressure imposed on the wet sand. We observe that both the trace left in the sand after sliding the hemisphere and the hardness of the water-sand mixture vary significantly with the water volume fraction. Adding a small amount of water results in an optimum in the hardness and a resulting minimum in the sliding friction. We present a ploughing model for the sphere-on-flat geometry that captures the observed ploughing friction through wet sand.

In **Chapter 4** we continue the discussion of partially water-saturated sand and relate it to the performed transportation of statues by the ancient Egyptians. A Tomb drawing suggests that water is poured in front of the sledge which is pulled with the use of manpower. Indeed, adding a bit of water decreases the sliding friction as we observe — in agreement with earlier studies — for sliding a ‘statue’ over wet sand in miniature. However, pouring more water to sand results in a muddy surface that increases the sliding friction again. We discuss the influence of the mechanical behaviour of (wet) sand on sliding a sledge over sand and show that ploughing greatly impacts the sliding friction. Pouring a limited amount of water to sand can reduce the ploughing, thereby decreasing the pulling force required to slide a sledge on sand.

In **Chapter 5** we discuss the slipperiness of ice. Ice friction is critical to winter sports, glacier movement, and transportation risks. We combine sliding experiments, a ‘skate’ sliding on a miniature ice skating rink, with contact mechanics calculations and hardness tests to study this system. We discover that ice friction is low because of the diffusive motion of surface ice molecules, combined with the exceptional hardness of ice close to its melting point. It is not always easy to skate on ice, the slipperiness of ice can be suppressed by a high contact pressure or a low temperature.

In **Chapter 6** we explore how one can tune friction with the use of geometrically patterned surfaces. Sliding friction is often specific to the material and surface properties and can be hard to predict. Depending on the application, either high friction for grip, or low friction for easy sliding can be desired. We fabricate sliders with artificial macroscopic surface patterns and explore how the surface roughness controls the sliding friction. We show that direct variation of the designed surface roughness allows the friction force to be varied by more than an order of magnitude. In addition, with the use of Kirigami metamaterial surfaces the friction can be tuned externally by a direct variation of its surface roughness.

CHAPTER 2

Experimental and computational techniques

This chapter gives a brief description of the experimental and computational techniques that are used for the research presented in Chapters 3 to 6. We discuss the two custom-made tribometers used for the horizontal sliding tests (performed in Chapters 3, 4 and 6) and circular sliding tests (performed in Chapter 5). Before (and after) sliding, the hardness and the microscopic surface topography of the sliding surfaces are quantified; We briefly discuss the methods that were used to do so here. In addition, we introduce the computational techniques that were used to quantify the contact mechanics of a (spherical) slider on a flat surface (used in Chapter 5).

2.1 Sliding friction

The sliding experiments are performed with two custom-made tribometers: (a) horizontal (linear) sliding, based on a commercially available tensile tester, and (b) circular sliding where a commercially available rheometer is converted to a tribometer.

2.1.1 Horizontal sliding

A typical sliding experiment is performed by sliding an object with a certain load on top of a horizontal flat surface, see Figure 2.1 for a schematic illustration of the experimental setup. This custom-made tribometer is based on a commercially available tensile tester, which consists of a load cell coupled to a stepper motor. We have used the ZwickRoell Z2.5 tensile tester with an HBM Z6FD1 load cell (precision of 5 mN, maximum load of 100 N, sampling rate of 50 Hz), initially built to uniaxially stretch or compress materials to characterise their mechanical properties. The tensile tester is placed on its side and pulls with a coupled rod or stiff cord on the top surface with a preset speed in the range of 1 μm/s up to 13 mm/s. To pull horizontally, the

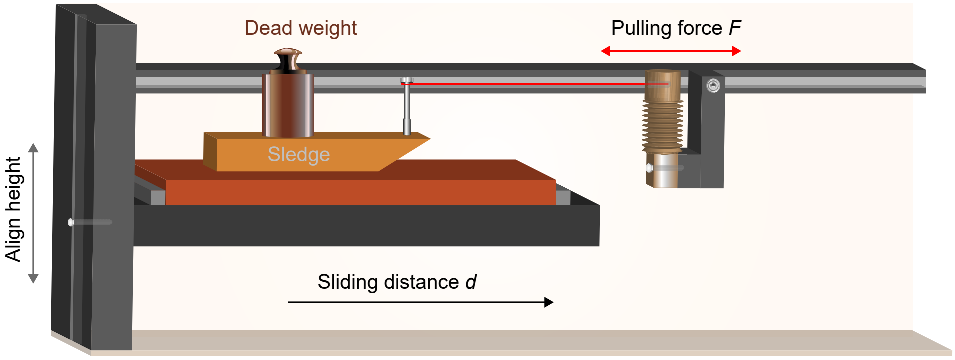

Figure 2.1: Schematic illustration of the experimental setup for horizontal sliding tests. A slider, for example a sledge, is pulled horizontally over a surface with the use of a stepper motor. The load cell allows us to monitor the pulling force F and sliding distance d for an imposed sliding speed v and normal force N. The latter is varied with placing dead weights on top of the slider.

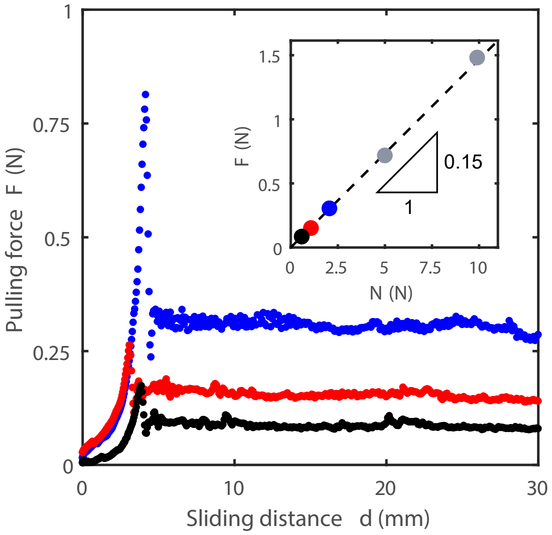

Figure 2.2: Pulling force F as a function of sliding distance d for a sledge sliding on a flat surface. The slider, including certain load placed on top of it, is pulled horizontally with a sliding speed of 1 mm/s over the fixed bottom plate. Both solids are 3D printed plastics with the commercially available resin named *Clear* (see Section 6.2 for more details). After approximately 5 mm, a stable pulling force is found which represents the dynamic friction force. In black, red, and blue circles the measured pulling force is given for a normal force of, respectively, 0.58 N, 1.07 N and 2.05 N. Inset: The measured friction force F as a function of the imposed normal force N. The dashed line represents the fit $F = \mu N$ with $\mu = 0.147 \pm 0.006$.

bottom surface can be aligned vertically.

In Figure 2.2 the pulling force F as a function of sliding distance d is given for a typical horizontal sliding experiment. Here, a plastic-on-plastic (3D printed with the commercial available resin named *Clear*, see Section 6.2 for more details) sliding experiment is performed at various imposed normal forces N. After approximately 5 mm, a stable pulling force is reached corresponding to the dynamic friction force. From these experiments, the friction force as a function of the normal force can be plotted as given in the inset of Figure 2.2. Consequently, the friction coefficient μ, the ratio of the friction force and normal force, can be calculated: $\mu = 0.147 \pm 0.006$.

2.1.2 Circular sliding

The circular sliding experiments are performed by a commercially available rheometer (Anton Paar, Dynamic Shear Rheometer 502). This rheometer imposes a rotational torque to the measuring system, which is a cylinder with a bottom plate or (truncated) cone that is perfectly aligned with the rotation axis. The rheometer measures the angular displacement and normal force (in the range of 1 mN up to 50 N with a resolution of 0.5 mN) and, with the use of a quick feedback loop, a constant sliding velocity can be imposed. Rheometers are built to perform rheology tests on (complex) fluids. The rheometer can apply, and measure torques from 1 nNm up to 230 mNm and, therefore, are very suitable to use as a custom-made tribometer.

To perform the circular sliding experiments, a slider is clamped at the bottom of the measuring system at a well-defined distance (on the order of $2 - 5$ mm) from the rotation axis and pressed against the countersurface; see Figure 2.3. The imposed rotational speed and measured torque can be converted into a sliding velocity v and friction force F where the former can be varied from 10^{-6} up to 10^{-1} m/s. During sliding, the normal force (mN precision) is measured and can be controlled by vertically displacing the rheometer (with sub-μm precision) while holding the

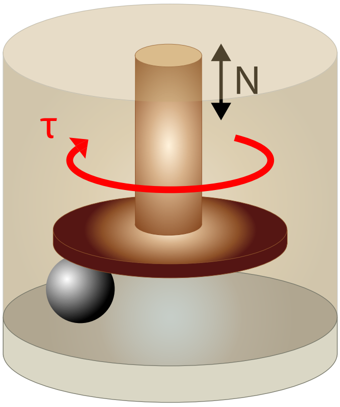

Figure 2.3: Schematic illustration of the setup to perform circular sliding experiments. A slider, here a sphere, is clamped off-axis at the bottom of the measuring system of the rheometer where, for an imposed rotation speed, the torque τ and normal force N are monitored. The normal force can be adjusted manually by vertically displacing the rheometer (with sub-μm precision). In Chapter 5, the setup is used for ice friction measurements where the setup is thermally isolated and cooled from below.

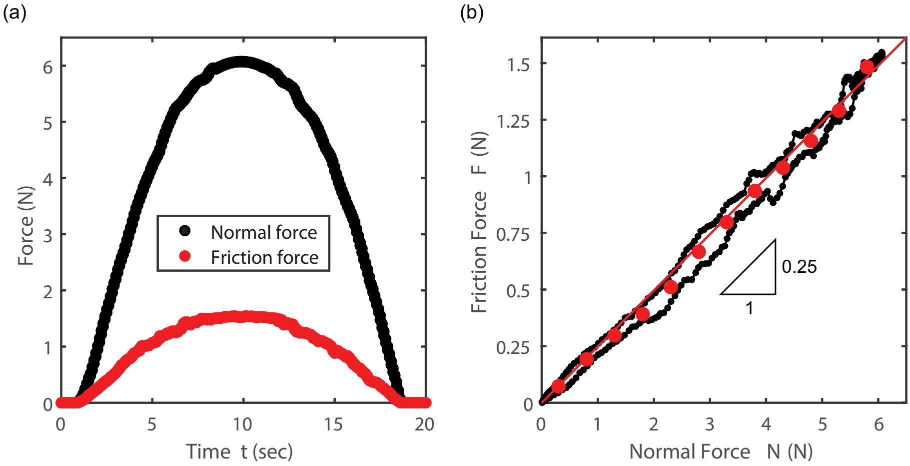

Figure 2.4: (a) Friction (red) and normal (black) force as a function of the time t when sliding a 2 mm stainless steel sphere over a lead surface. The sphere is rotated with a controlled sliding speed of 0.4 mm/s and is in contact with the lead surface for about 20 seconds due to misalignment between the rotation plane of the sphere and the lead surface. (b) Friction force as a function of the normal force where the black circles are the measured data as presented in (a). The red line is a linear fit of the data to calculate the friction coefficient, here $\mu = 0.248 \pm 0.001$. The red circles represent an average of the measured data for steps of $dN = 0.5$ N in normal force.

flat surface in place. In Figure 2.4(a) the friction force F (red circles) and normal force N (black circles) as a function of the time t are given for a typical circular sliding experiment: A 2 mm stainless steel sphere is dragged on a lead surface with a sliding speed of 0.4 mm/s. The misalignment of the rotation axis of the sphere and the lead surface allows us to perform the sliding experiments over a range of normal forces. Only in a fraction of the circular sliding movement, the slider makes contact with the substrate that has its highest loading force N at the lowest point. In this example, the lowest point of the slider is reached after 10 seconds. The friction force increases linearly with the normal force [see Fig. 2.4(b)] and a friction coefficient of $\mu = 0.248 \pm 0.001$ can be found.

For the sliding experiments on ice, as performed in Chapter 5, the setup is thermally isolated and cooled with a coolant liquid (for a temperature between -15 °C and 0 °C) or liquid nitrogen (for a temperature between -110 °C and -15 °C). The temperature of the ice is measured with an embedded thermocouple close to the surface and controlled with the flow rate of cooling liquid.

2.2 Penetration hardness

The hardness of a material is the resistance to (local) plastic deformation as a result of normal (indentation) or tangential (abrasion) stress. Often the term hardness refers to the yielding compressive pressure of a solid; after (initial) elastic deformation due to the exerted stress, some solid materials deform irreversibly. Note that depending on the material, crack formation in a material and, subsequently, full fracture can already occur directly after elastic deformation. The onset of plastic deformation, including a quantification protocol, is complicated to define as it depends on the specific conditions: the material of the test-sample (viscoelastic behaviour, strain-hardening, purity, heterogeneity), the stress-inducer (geometry, thermal conductivity) and the external conditions (strain rate, geometry-size) [54,55].

For example, the hardness of a metal largely varies with the characteristic length scale on which it is measured [56]. On the nanoscale, the hardness is determined by the number of intermolecular bonds of the atoms arranged in a crystal lattice. On larger scales, the influence of polycrystallinity is amplified where the hardness is mainly set by the crystallographic defects [57]. A metal consists of crystalline grains in which point and line defects (mainly on the boundary of the grains) can result in movement and formation of dislocations that, consequently, can result in early plastic deformation and creep [58].

The quantification of hardness is therefore strongly dependent on the measurement protocol and should be chosen carefully to match the specific conditions of the application. For example, to test the abrasive hardness of minerals the Mohs scale for hardness can be applied: The hardness is categorised by investigating on which reference minerals — from soft talc up to hard diamond — the test sample leaves a scratch [59]. More quantitative test protocols, mainly in metallurgy, have been developed and performed to define hardness. Commonly used protocols (and corresponding scales) are based on Brinell, Vickers, Shore and Rockwell [54,60,61]. In these tests, the specific indenter geometry (pyramidal, spheres, cones), indenter size, strain rate and the loading time are defined.

In Chapters 3 to 5, we quantify the hardness for conditions which resemble the parameter ranges exercised in the friction experiments: normal force, length scale, indentation depth, normal- and tangential speed. The hardness can be evaluated from an indentation experiment where a spherical or conical indenter is pressed on the flat test-sample; for increasing loading force N the resulting plastic deformation depth δ is monitored. Here, the penetration hardness can be calculated based on the projected contact area A_c of the indenter on the test-sample and the loading force:

$$P_\mathrm{h} = \frac{N}{A_\mathrm{c}} \, . \tag{2.1}$$

See Figure 2.5 for a schematic illustration of the indentation experiment based on a spherical (radius R) or conical (apex angle α) indenter. The indentation experiments are performed with a tensile tester (see also Section 2.1.1) which pushes the indenter vertically into the sample. The monitored indentation depth δ can, for the given indenter-geometry, be converted to the contact area A_c. For a large range of indentation speeds (1 μm/s up to 13 mm/s) and indentation forces (maximum of 100 N with a precision of 5 mN), the loading and unloading can be monitored.
When performing an indentation experiment, the stiffness of the measurement system also has to be taken into account. The measurement system, i.e., the tensile tester including the indenter, elastically deforms for increasing load. To correct the measured indentation depth δ for this elastic behaviour of the system, a reference loading experiment specific for the indentation setup is performed without the sample. The indenter is loaded on the sample stage where normally the test sample is placed, see Figure 2.6 for a typical loading-unloading curve. Here, up to 30 N the loading

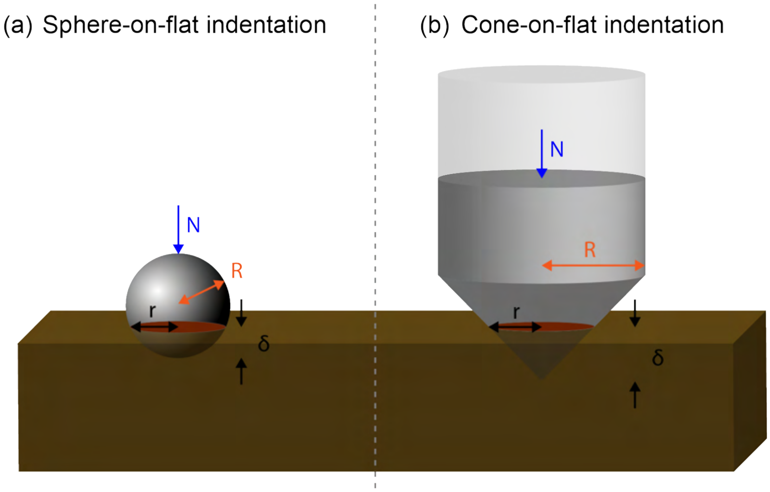

Figure 2.5: Schematic illustration of the indentation experiment performed with a spherical (a) or conical (b) indenter on a flat sample. For an increasing loading force N the indentation depth δ is monitored. The sphere (radius R) and cone (apex angle α and maximum radius R) indent the flat surface resulting in a projected contact area A_c with radius r.

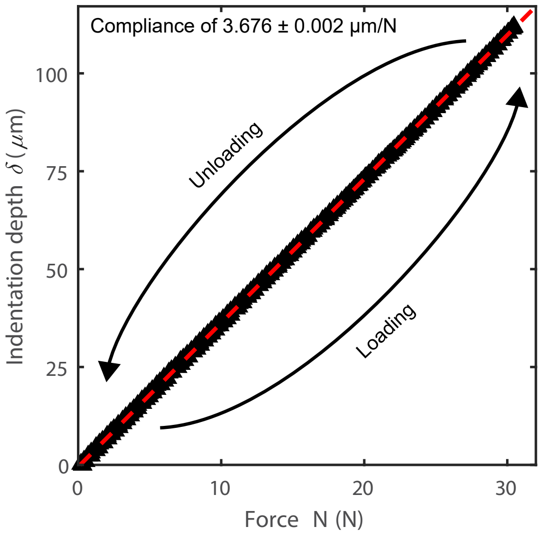

Figure 2.6: The indentation depth δ as a function of the loading force N to quantify the stiffness of the measurement system used for hardness tests. In this reference loading-unloading experiment, the indenter is loaded up to 30 N onto the sample stage, i.e., where normally the test-sample is placed. No significant hysteresis can be observed and, consequently, the compliance of the measurement system can be quantified with a linear fit, see the dashed line. In this example, the compliance is 3.676 ± 0.002 μm/N. Subsequently, when a hardness test is performed, the monitored indentation depth is corrected with the use of the measured compliance of the setup.

and unloading is monitored which, as no significant hysteresis is observed, is purely elastic. The measured slope of this reference experiment (red dashed line in Fig. 2.6) reveals the compliance (which is the inverse of the stiffness). In this example, the compliance of the measurement system is 3.676 ± 0.002 μm/N. When an indentation experiment is performed, we correct the monitored indentation depth with the use of the measured compliance of the specific setup.

In Figure 2.7, two typical indentation experiments are given for (a) a sphere indenting a lead surface and (b) a cone indenting a water-sand mixture (water volume fraction of $\phi_\mathrm{w} = 5\%$). Both indenters are made from stainless steel which is significantly harder than the samples which are going to be tested. The measured loading-unloading curve for both systems shows a large hysteresis; when the indenter starts to retract after loading, the measured force immediately drops to zero. This confirms that during loading, the test-sample has been plastically deformed.

Throughout the loading, the projected contact area A_c increases for the spherical and conical indenter. The contact area $A_\mathrm{c} = \pi r^2$, with r the radius of the projected circle, can be calculated based on the measured indentation depth δ. For a sphere-on-flat geometry [see Fig. 2.5(a)], we can write

$$\begin{aligned} r^2 &= 2R\delta - \delta^2 \\ &\approx 2R\delta\ . \end{aligned} \tag{2.2}$$

The approximation is valid for $\delta \ll R$. For the conical indenter, the contact radius can be written as

$$r = \tan(\tfrac{1}{2}\alpha)\delta\ . \tag{2.3}$$

Subsequently, the contact area for the specific geometries can be written in terms of

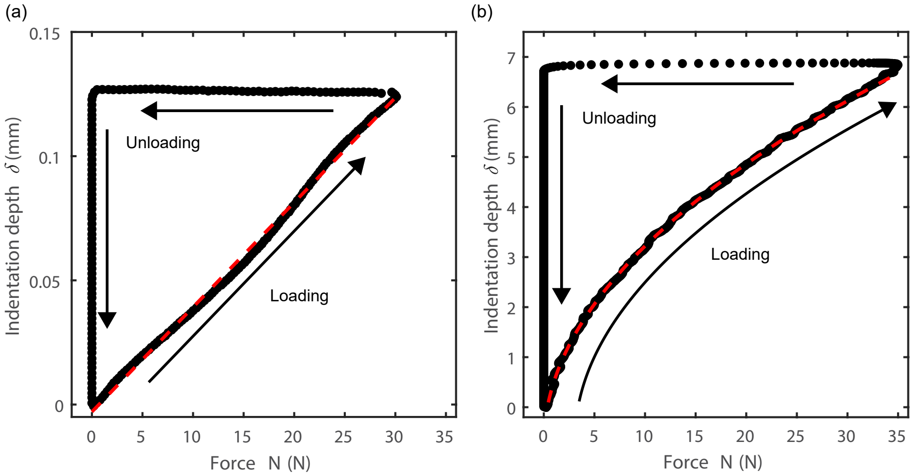

Figure 2.7: The indentation depth δ as a function of the loading force N for (a) a spherical indenter (radius $R = 2$ mm) pressed onto lead and (b) a conical indenter (apex angle $\alpha = 60°$) pressed onto a water-sand mixture (water fraction of $\phi_\mathrm{w} = 5\%$). The loading-unloading curves show full plastic indentation; when the indenter retracts after loading, the force drops immediately. The red dashed lines show fits based on Eqs. (2.6) and (2.7) that enables us to calculate the penetration hardness: Lead has a penetration hardness of $P_\mathrm{h} = 18.9 \pm 0.1$ MPa and the water-sand mixture has a penetration hardness of $P_\mathrm{h} = 63.4 \pm 0.3$ kPa.

the indentation depth as

$$\begin{aligned} \text{Sphere: } A_\mathrm{c} &= 2\pi R\delta \qquad (2.4)\\ \text{Cone: } \quad A_\mathrm{c} &= \pi \tan^2(\tfrac{1}{2}\alpha)\delta^2\,. \qquad (2.5) \end{aligned}$$

The penetration hardness can be calculated by fitting the following expressions on the measured loading-curve (red dashed lines in Fig. 2.7):

$$\begin{aligned} \text{Sphere: } \delta &= \frac{1}{2\pi R P_\mathrm{h}} N \qquad (2.6)\\ \text{Cone: } \quad \delta &= \frac{1}{\sqrt{\pi \tan^2(\tfrac{1}{2}\alpha) P_\mathrm{h}}}\sqrt{N}\,. \qquad (2.7) \end{aligned}$$

Therefore, the indentation depth increases either linearly or as a square root of the loading force, set by the geometry of the indenter. When the data as presented in Figure 2.7 are fitted, we find a penetration hardness of $P_\mathrm{h} = 18.9 \pm 0.1$ MPa for lead and $P_\mathrm{h} = 63.4 \pm 0.3$ kPa for the water-sand mixture.

The penetration hardness for a sphere-on-flat geometry [Fig. 2.5(a)] is calculated based on the approximation for the contact radius valid for $\delta \ll R$ as given in Equation (2.2). For the data presented in Figure 2.7(a), this approximation results in an underestimation of the penetration hardness of 2.6%; precise calculation based on Equation (2.2) results in a penetration hardness of $P_\mathrm{h} = 19.4 \pm 0.1$ MPa. The sphere-on-flat hardness test performed in Chapter 5 results in a relatively large hardness ($P_\mathrm{h} \sim 100$ MPa) and, therefore, has a small indentation depth δ compared with the hardness-tests on a lead surface. The approximation $\delta \ll R$ does therefore not result in a severe error.

Another sphere-on-flat hardness test which is often used is the Brinell hardness method. In contrast to the penetration hardness test with a spherical indenter, where the related area is the projected contact area, the Brinell hardness is calculated based on the curved contact area:

$$\begin{aligned} A_\mathrm{c} &= 2\pi R\delta \\ &= 2\pi R\left(R - \sqrt{R^2 - r^2}\right)\,. \end{aligned} \qquad (2.8)$$

Therefore, the Brinell pressure considers the radial stress in the test sample exerted by the spherical indenter. For the data presented in Figure 2.7(a), the Brinell hardness results in 18.82 ± 0.06 MPa, which is 2.9% less than the penetration hardness.

Somewhat surprising, the approximation made in Equation (2.2) makes that the contact areas as computed in the Brinell and penetration hardness calculations are now equivalent. In conclusion, the sphere-on-flat indentation experiments enable us to calculate the hardness where, for the regime $\delta \ll R$, the Brinell and penetration hardness method are equivalent.

2.3 Surface characterisation

One of the major parameters that determines friction is the microscopic surface topography of the sliding surfaces. Prior to a sliding test, we quantify the topography of our surfaces with a 3D laser-scanning profilometer (Keyence, VK-X1000). This contactless profilometer scans with an ultraviolet laser (wavelength of 404 nm) and measures the intensity of the reflection for every voxel (volumetric pixel). This

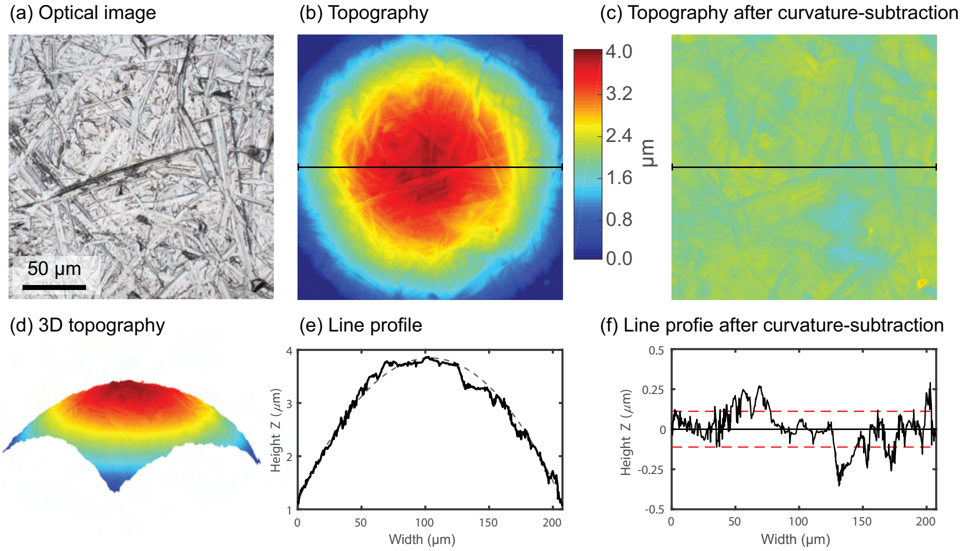

Figure 2.8: Quantification of the microscopic surface topography of a 2 mm radius stainless steel sphere based on 3D laser-scanning profilometry. (a) The optical image of the sphere for an area of 208 by 208 μm. (b-c) The height variation before and after subtraction of the macroscopic curvature of the sphere. (d) 3D presentation of the topography including the macroscopic curvature of the sphere. (e-f) The height Z as a function of the lateral direction before and after subtraction of the curvature. The red dashed line in (f) represents the root-mean-square height variation S_q.

intensity as a function of the axial direction has a peak where the surface is located. Therefore, by accurate peak detection of the reflected light, the height Z can be quantified as a function of the lateral directions X and Y.

The surfaces are scanned over an area of 208 μm by 208 μm with a lateral resolution of 138 nm/pixel and 20 nm resolution in the height direction. In Figure 2.8 a typical measured surface topography is plotted where a stainless steel sphere (radius of 2 mm) has been used. In addition to the height variation [Fig. 2.8(b)], a bright field image can be made, as shown in Figure 2.8(a). To quantify the microscopic surface height profile, the macroscopic curvature (if present) is subtracted from the measured height; see Figure 2.8(c). In Figure 2.8(e) and (f) the line profiles that, respectively, include or exclude the surface curvature are plotted. The microscopic surface roughness can be quantified with the root-mean-square (rms) surface height variation S_q. For the steel sphere, the calculated surface roughness after curvature subtraction is $S_\mathrm{q} = 112$ nm which is represented in Figure 2.8(f) with the red dashed lines.

2.4 Contact mechanics calculations

The resistance against sliding of two surfaces over each other can be understood as the resistance to shear the loaded microscopic contact points over each other. This can be quantified based on the stresses on the asperity contact area: the shear stress σ_s (tangential stress) and the local contact pressure P_c (normal stress). To understand the loading of the two surfaces in contact, we perform contact mechanics calculations. These calculations are performed in Chapter 5 for a sphere-on-flat (skate on ice) geometry to quantify the real contact area and local contact pressure based on the mechanical properties and measured surface topography. We use a tribology simulator (named TRIS, publicly available at Tribonet [62]) to solve the elastoplastic contact equations through a numerical boundary element model. Based on the mechanical properties and the surface topographies of the solid surfaces, the interfacial gap at each of the in-plane coordinates defined by the topography is calculated for a given normal force. Those locations at which the interfacial gap is zero form the area of real contact where, in addition, the local contact pressure is quantified. This calculation is performed by numerically solving the (elastic-fully plastic) half space model [63–66], which is explained (and experimentally validated) in more detail in References [62, 66, 67].

In Figure 2.9 a typical result of the numerical model is presented. For a sphere-

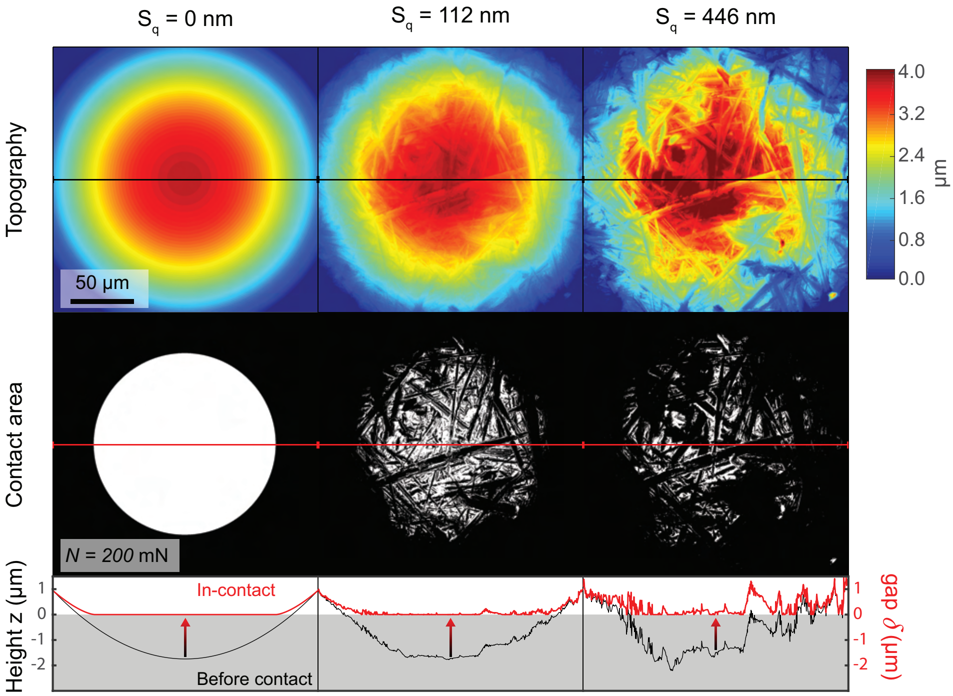

Figure 2.9: The surface topography and contact area when a smooth ($S_\mathrm{q} = 0$ nm), intermediate rough ($S_\mathrm{q} = 112$ nm) and very rough ($S_\mathrm{q} = 446$ nm) sphere (2 mm radius) are pressed on a smooth flat surface. The contact area (middle row) for the given surface topography (top row) is quantified with the Tribology Simulator [62]. In addition, the lowest row shows the surface topography height Z before contact (black line) and the gap size in-contact (red line) as a function of the width. The calculations are performed with an effective elasticity of $E^* = 0.84$ GPa and a hardness of the sphere and the smooth flat surface of, respectively, 100 MPa and 420 MPa.

on-flat contact system, the interfacial gap δ is calculated for a 2 mm radius sphere with various surface topographies: A perfectly smooth ($S_\mathrm{q} = 0$ nm), intermediate rough ($S_\mathrm{q} = 112$ nm) and very rough ($S_\mathrm{q} = 446$ nm) microscopic surface topography. The intermediate rough surface topography is the measured topography for the steel sphere as presented in Figure 2.8. The perfectly smooth and very rough surface topographies are based on artificially reducing/enhancing the measured stainless steel height variation $Z(x, y)$ with, respectively, a factor of 0 and 4.

When the spheres are pressed against a smooth flat surface, the real contact area can be quantified as shown in the middle row of Figure 2.9 for a load of 200 mN.

A circular contact area, with contact radius $r = 71\ \mu$m, is found for the perfectly smooth sphere. In contrast, a very rough sphere results in contact spots based on the asperities of the rough surface topography. The real contact area can then be quantified for increasing load N (see Fig. 2.10) which largely depends on the surface topography.

The calculations for the sphere-on-flat contact mechanics illustrate the influence of the microscopic surface topography and the loading force (often the gravitational force). Several theoretical frameworks are developed, which combine elasticity, plasticity, and adhesion, to capture the contact mechanics. Two models, fully elastic Hertzian contact and fully plastic contact, capture the, respectively, maximum and minimum of the real contact area which can be reached. We will briefly discuss the aforementioned models and compare them to the calculated contact area of the Tribology Simulator for increasing normal load; see Figure 2.10 where the Hertzian

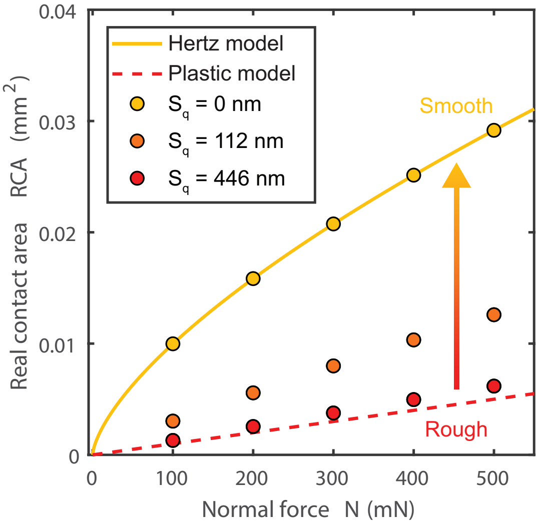

Figure 2.10: Real contact area RCA as a function of the load N for a sphere (radius of 2 mm) pressed on a flat surface. The yellow, orange, and red circles represent the numerically calculated contact area for spheres with a surface roughness of, respectively, 0 nm, 112 nm and 446 nm. The continuous and dashed lines represent, respectively, the elastic Hertzian contact area [Eq. (2.10)] and the contact area controlled by pure plasticity [Eq. (2.11) with a hardness of 100 MPa].

model and plastic contact model are represented as, respectively, the red and yellow lines.

Hertzian contact

As mentioned in Chapter 1, Hertz developed a theory in the late 19th century to describe the contact formation between smooth and non-adhering elastic bodies [21,22]. Based upon the classical theory of elasticity and continuum mechanics he describes the elastic, thus reversible, deformation of the solids based on their elastic properties, which enables us to calculate the contact area RCA and contact pressure P_{c}. The Hertzian model for a sphere on a flat surface gives the contact radius r as [21,22]:

$$r^3 = \frac{3RN}{4E^*}\,, \tag{2.9}$$

where R is the radius of the sphere and N the imposed loading force. The effective elasticity of the system is given as $\frac{1}{E^*} = \frac{1-\nu_1^2}{E_1} + \frac{1-\nu_2^2}{E_2}$ which is based on the Young's moduli E_1 and E_2 and the Poisson's ratios ν_1 and ν_2 of the two materials. The real contact area for a sphere pressed on a flat surface is

$$\mathrm{RCA} = \pi r^2 = \pi \left(\frac{3RN}{4E^*}\right)^{2/3} . \tag{2.10}$$

In Figure 2.10 the real contact area for the same conditions of the performed computational calculations ($E^* = 0.84$ GPa) is given in a continuous yellow line for increasing force N. As the model matches the calculated RCA for a perfectly smooth spherical slider, it illustrates that the computational technique results in a purely elastic contact. Therefore, the contact area is relatively large and increases sublinearly ($\mathrm{RCA} \propto N^{2/3}$) with the normal force.

Plastic contact

When two surfaces are pressed onto one another, the highest asperities of the two surface topographies will make contact and, consequently, experience a large contact pressure. As Bowden and Tabor already emphasised (see also Chapter 1), the asperities will irreversibly deform when the contact pressure exceeds the hardness of the material [19,22]. Plastic deformation of the asperities will continue up to the contact pressure is lowered down to the hardness. This flattens out of the asperities due to plastic deformation result in a contact area described as

$$\mathrm{RCA} = \frac{N}{P_\mathrm{h}}\,, \tag{2.11}$$

with P_h the lowest hardness of the materials in contact. In Figure 2.10 in the red dashed line, the contact area is plotted for a penetration hardness of $P_\mathrm{h} = 100$ MPa, as used in the numerical calculated contact area. It illustrates that the computational calculation for a very rough sphere ($S_\mathrm{q} = 446$ nm) pressed on a flat surface results in a contact area which is mainly the result of plastic indentation. Consequently, the contact area increases linearly with the normal force.

CHAPTER 3

Ploughing friction on wet sand

In this chapter, the friction for sliding a hemisphere over partially water-saturated granular materials is investigated as a function of the water volume fraction. We find that ploughing friction is the main sliding mechanism: The slider leaves a deep trace in the sand after its passage. In line with previous research and everyday experience, we find that the friction force varies nonmonotonically with the water volume fraction. The addition of a small amount of water makes the friction force sharply drop, whereas too much added water causes the friction force to increase again. We present a ploughing model that quantitatively reproduces the nonmonotonic variation of the friction force as a function of water volume fraction without adjustable parameters. In this model, the yield stress of the water-sand mixture controls the depth to which a hemispherical slider sinks into the sand and, consequently, also the force that is required to plough through the water-sand mixture.

3.1 Introduction

The mechanics of sliding over or digging in soil is crucial to many natural phenomena such as plant root growth [68–70], terradynamics [71,71] and antlion hunting strategies [72,73]. Industrially, very similar phenomena control processes in agriculture [74], the production of pharmaceuticals [75] or soil transport through pipes [76]: The importance of the manipulation of granular materials is difficult to overestimate since more than 10% of the world energy consumption is spent on it [77]. In all of the above phenomena and processes, the mechanics of granular materials is greatly impacted by the presence of small amounts of water.

When water is introduced to a granular system, liquid bridges form between neighbouring grains and bind them together, resulting in a cohesive material [50, 78–82]. The stiffness of a granular material, quantified, for instance, by the elastic shear modulus G', varies nonmonotonically with the addition of liquid [51]. The stiffness is optimal when small liquid bridges form between the grains, which results in attractive forces binding the granular material together. At higher water contents, the capillary bridges start to coalesce, thereby decreasing the shear modulus. This intricate interplay between mechanical strength and water content can be illustrated by building sandcastles with sand that has been wetted with a varying amount of water: The highest sandcastle is constructed by mixing the sand with some (but not too much) water [83].

Remarkably, sliding friction on water-sand mixtures follows very similar (nonmonotonic) behaviour in which the addition of a few percent of water can greatly reduce the friction while too much water makes the sand muddy and difficult to slide over [6]. In this chapter we present sphere-on-sand sliding experiments and show that the relation between the friction force and stiffness is fully described by a ploughing model that takes advantage of the simple sphere-on-flat geometry.

3.2 Experiments

In the sliding experiments, we use the custom-made tribometer (see Section 2.1.1 for more details) to horizontally slide a stainless steel hemisphere of radius $R = 52.5$ mm over a water-sand mixture [Fig. 3.1(a)]. The normal force N is controlled by filling the hemisphere with dead weights. At a sliding speed of 4 mm/s over a total sliding distance of 130 mm the friction force F is monitored. Variation of the sliding speed in the range from 0.1 mm/s to 13 mm/s does not lead to an appreciable change in friction force in this regime. All experiments are performed using polydisperse ($100 - 1000\ \mu$m grains) ISO 679 standard sand, which is first dried in an oven and cooled down to room temperature. Subsequently, the sand is thoroughly mixed with demineralised water and compacted by repeated tapping.

In addition to the forces, the final radius r of the track drawn in the water-sand mixture perpendicular to the movement is measured. This enables us to calculate the ploughing cross section A_P and the projected contact area A_c [Fig. 3.1(b-c)]. The penetration hardness, the contact pressure at yielding, can then be obtained from the contact area A_c: $P_\mathrm{h} = N/A_\mathrm{c}$. Note that, in contrast to the indentation experiments discussed in Section 2.2, the dynamic contact area while sliding is only based on the front part of the sphere: $A_\mathrm{c} = \frac{1}{2}\pi r^2$. Using varying dead weights, the normal force was varied from 2.5 N up to 16 N for each water-sand mixture and subsequently the

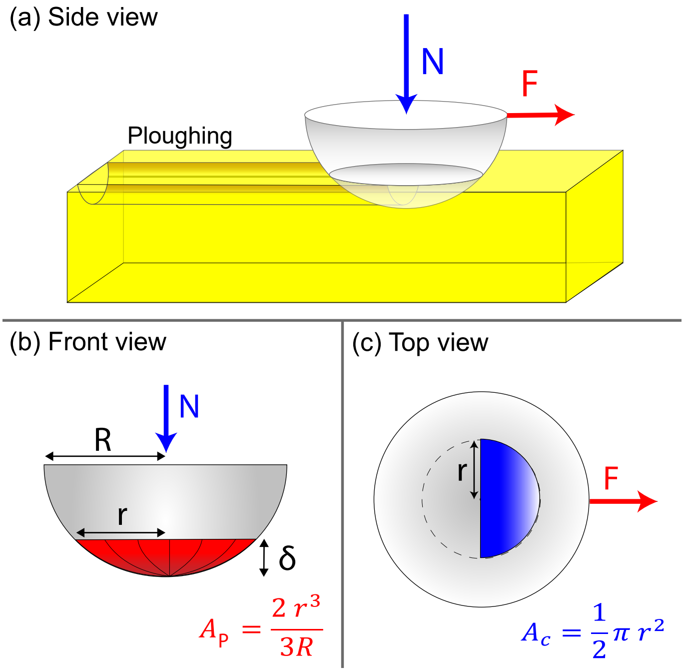

Figure 3.1: Schematic representation of the ploughing experiment. **a)** Side view: Normal (N) and frictional (F) forces which act on the sliding hemisphere. **b)** Front view: The hemisphere with radius R, where the ploughing cross section A_P (red) can be calculated using the track radius r. **c)** Top view: The hemisphere with the projected area of contact A_c (blue).

track radius is measured, and the average penetration hardness is calculated.

Furthermore, the ploughing cross section A_P can be calculated with the track radius r. The cross section can be written as $A_\mathrm{P} \approx \frac{4}{3} r\delta$ with the depth of penetration $\delta \approx \frac{r^2}{2R}$ if $\delta << R$. Consequently, the ploughing area is $A_\mathrm{P} = \frac{2r^3}{3R}$. Note that the assumption $\delta << R$ results in a relative error in A_P and μ [with Eq. (3.2)] of less than 4.5% for $r \leq 20$ mm ($\frac{r}{R} \leq 0.38$). However, for $r = 40$ mm, the relative error increases to 21%, which results in an underestimation of the friction coefficient for $\phi_\mathrm{w} = 0\%$ in Figure 3.2.

3.3 Results

3.3.1 Ploughing through wet sand

In agreement with earlier measurements [6], we find that the friction coefficient first decreases as more water is added to the sand, and then increases again (see Fig. 3.2). What mechanism drives this nonmonotonic variation of the friction force with water content? In each of the sliding experiments, the hemisphere creates a clear ploughing track, the width of which can be measured after the sliding stops. Interestingly, we find that the width of the ploughing track also varies nonmonotonically with the water volume fraction, just like the friction coefficient (Fig. 3.3): Sliding is more

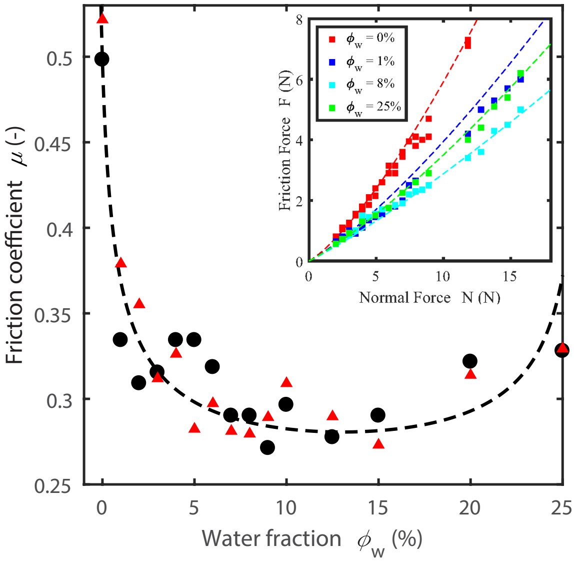

Figure 3.2: Evolution of the friction coefficient μ for the water volume fraction ϕ_w. The friction coefficient obtained from the measured friction force and fixed normal force ($N = 7.9$ N) in black circles display a nonmonotonic behaviour for increasing water fractions. With use of the ploughing model, the friction coefficient can be either modelled based on the ploughing track radius r [Eq. (3.2) in red triangles] or based on the penetration hardness P_h of the water-sand mixture [Eq. (3.3), dashed line]. The inset shows the friction force as function of the normal force for various water volume fraction experimentally (squares) and predicted by the ploughing model based on the penetration hardness P_h (dashed line).

difficult when the hemisphere sinks deeper into the sand.

The presence of a ploughing track indicates that during sliding, the water-sand mixture is plastically deformed in both the normal and tangential directions. To quantify the stresses involved in this plastic deformation we simply divide the external forces by the area on which they act. In the normal direction, the gravitational force that acts on the hemisphere is supported by the projected area of contact $A_c = \frac{1}{2}\pi r^2$ [see Fig. 3.1(c)] leading to an average contact pressure of $P_h = N/A_c$ which defines the penetration hardness of the water-sand mixture, P_h (Fig. 3.4). We find that the addition of some (but not too much) water has a dramatic effect on the penetration hardness of the compacted water-sand mixture: While dry sand can only support a stress of 3 kPa, ideally wetted sand supports up to 80 kPa of normal stress before showing a marked plastic deformation. When too much water is added to the sand, the mixture becomes muddy and the penetration hardness drops again to a value of 20 kPa at 25% water volume fraction.

The nonmonotonic behaviour of the penetration hardness is qualitatively similar

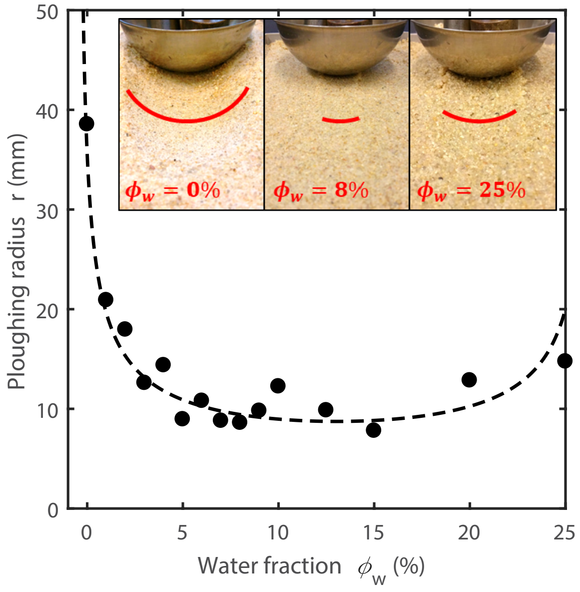

Figure 3.3: Ploughing radius r as a function of water volume fraction ϕ_w for a fixed normal force of $N = 7.9$ N. Like the friction coefficient, the ploughing track width (black circles) evolves nonmonotonically with the water content, also shown based on the ploughing model (dashed line, $r = \sqrt{\frac{N}{\frac{1}{2}\pi P_h(\phi_w)}}$). The inset shows images of the experiments for $\phi_w = 0, 8$ and 25% with red lines highlighting the ploughing tracks.

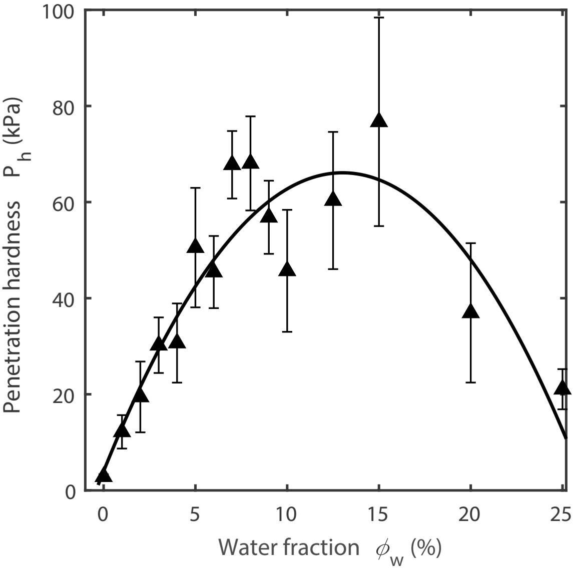

Figure 3.4: Penetration hardness P_h as a function of water volume fraction ϕ_w. The error bars represent the standard deviation. The solid line describes the data based on a first-order increase due to liquid bridge formation and an exponential decrease based on the coalescence of these liquid bridges.

to that of the elastic shear modulus. The physics behind the behaviour of the latter is fully (and quantitatively) understood: The initial increase when small amounts of water are added is due to the formation of more and more liquid bridges between neighbouring grains. The subsequent decrease at higher water content results from the filling up of the bridges: The smaller the liquid bridge, the higher the Laplace pressure holding two grains together and hence the stiffer the system; ultimately the coalescence of the liquid bridges at even higher water content leads to an even smaller modulus, as the Laplace pressure becomes very small [51]. The behaviour of the modulus can be roughly approximated by first a linear increase with increasing water content; for a fixed bridge volume the number of bridges scales linearly with the amount of fluid added [51]. For the decrease of the stiffness, the coalescence of the liquid bridges is the dominant effect; we can assume that this is a random (Poisson) process, so that an exponential decrease of the hardness should be observed for increasing water content. If we apply the same ideas to the penetration hardness, we get a very satisfactory description of the data, given by the solid line Figure 3.4.

3.3.2 The ploughing model

The penetration hardness then controls the depth to which the hemisphere penetrates the water-sand mixture. Therefore, if the load is varied, the contact area increases until the pressure again reaches the penetration hardness. Consequently, the ploughing track increases with increasing normal force, as is shown in Figure 3.5 for several water fractions. The dashed line represents the ploughing track radius based on the calculated average penetration hardness with $r(\phi_\mathrm{w}, N) = \sqrt{\frac{N}{\frac{1}{2}\pi P_\mathrm{h}(\phi_\mathrm{w})}}$. The ploughing motion of the hemisphere involves an analogous deformation in the tangential direction.

We now use a well-known method introduced for metal-on-metal ploughing [45,46] to calculate the ploughing force. Ploughing starts if the tangential pressure on the water-sand mixture exceeds its penetration hardness P_h; therefore, the ploughing force can be written in terms of the penetration hardness and the cross-sectional area

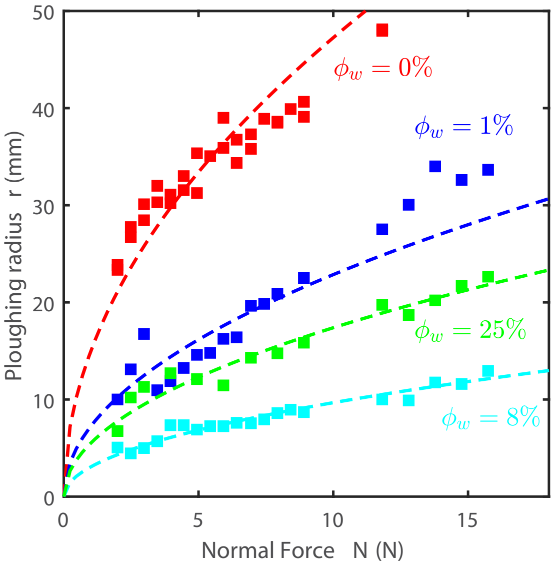

Figure 3.5: Ploughing radius r as a function of normal force N for various water volume fractions. The squares represent the experimental data and the dashed lines reflects the model ($r = \sqrt{\frac{N}{\frac{1}{2}\pi P_\mathrm{h}(\phi_\mathrm{w})}}$) based on the penetration hardness. The radius increases with the normal force and has a minimum for $\phi_\mathrm{w} = 8\%$. Note that the nonmonotonic behaviour of the track radius for increasing water content holds over the full domain of normal forces.

as $F_\mathrm{P} = P_\mathrm{h} A_\mathrm{P}$ with $A_\mathrm{P} = \frac{2r^3}{3R}$ [see Fig. 3.1(b)]. Subsequently, the friction coefficient is the ratio of the ploughing force to the normal force

$$\mu = \frac{P_\mathrm{h} A_\mathrm{P}}{N} + \mu_0 \, . \tag{3.1}$$

To account for the fact that even in the absence of ploughing a frictional force will resist the sliding, we introduce μ_0 as the surface friction contribution. Using the definition of the penetration hardness and Equation (3.1), the friction coefficient μ can now be expressed in terms of the ploughing track size as

$$\mu = \frac{4\, r(\phi_\mathrm{w}, N)}{3\pi R} + \mu_0 \, . \tag{3.2}$$

Equation (3.2) indeed suggests that the deeper the hemisphere ploughs into the sand the larger the friction, as observed in Figures 3.2 and 3.3. Furthermore, from Equation (3.2) we can now calculate the friction coefficient using the imposed normal force N, the measured track width r and the surface friction contribution μ_0. Indeed, the calculated friction coefficient is in good agreement with the measured friction coefficient (black circles and red triangles in Figure 3.2).

Alternatively, the friction coefficient can be expressed in terms of the penetration hardness P_h, the imposed normal force N and the surface friction coefficient μ_0:

$$\mu = \frac{4\sqrt{2}}{3\pi^{3/2} R} \sqrt{\frac{N}{P_\mathrm{h}(\phi_\mathrm{w})}} + \mu_0 \, . \tag{3.3}$$

In Figure 3.2 we plot this function (dashed line) using the relation between penetration hardness and water content obtained for normal forces ranging from 2.5 N to 16 N in Figure 3.4. Again, we find good agreement between the ploughing model and the experiment. Finally, Equation (3.3) explicitly predicts a super-linear increase of the friction force F as a function of the normal force: $F \sim N^{3/2} + \mu_0 N$. We indeed observe such behaviour for different water-sand mixtures (inset Fig. 3.2); also note that the nonmonotonic behaviour of the friction force for increasing water content is sustained over the full range of imposed normal forces probed here.

The only adjustable parameter in the ploughing model is the surface friction contribution, $\mu_0 = 0.21$, corresponding to the sliding friction between the hemisphere and the sand grains. When there is no permanent deformation of the water-sand packing, we expect the total friction to be equal to μ_0: $\mu = \mu_0$, corresponding to $R = 0$ in Equation (3.2). To obtain exactly this type of sliding motion, we now fix a collection of sand grains to a plate using glue. The hemisphere is then pulled over these immobilised sand grains using normal forces ranging from 2.5 N up to

16 N. The measured friction coefficient, $\mu_0 = 0.19 \pm 0.09$, is in good agreement with the value that was used to match the ploughing model to the experimental data in Figure 3.2: $\mu_0 = 0.21$.

3.4 Discussion

We have shown the influence of the hardness on the friction force when a hemisphere with an imposed normal force ploughs through a water-sand mixture. When the hardness of the granular material is high, the slider has a small indentation depth and a shallow ploughing track which, consequently, results in a low friction coefficient: high hardness is low friction. However, the ploughing model is not limited to load-controlled sphere-on-flat sliding experiments. In Figure 3.6 the influence

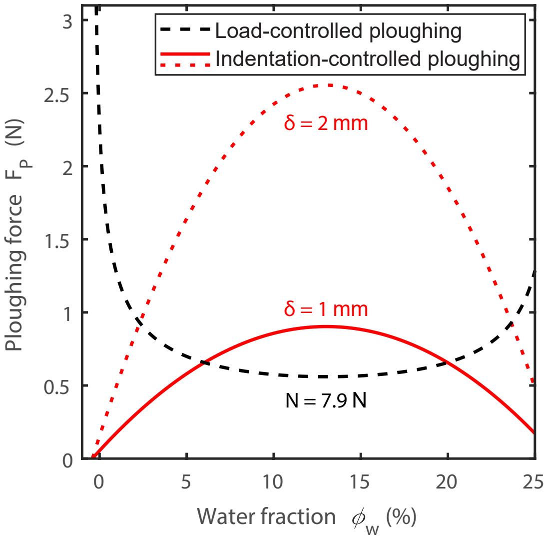

Figure 3.6: Ploughing force F_P as a function of water volume fraction ϕ_w. The black dashed line gives the load-controlled ploughing model [Eq. (3.3)] for sliding a hemisphere ($R = 52.5$ mm) at a load of $N = 7.9$ N over a water-sand mixture with a given hardness P_h (see Fig. 3.4). In the red continuous and dashed lines, the indentation-controlled ploughing model for a set indentation depth of, respectively, $\delta = 1$ mm and $\delta = 2$ mm. The indentation depth and the radius of the hemisphere ($R = 52.5$ mm) sets the ploughing area A_P which are 13.7 mm^2 and 38.6 mm^2 for, respectively, the red continuous and dashed lines.

of load- or indentation-controlled sliding is illustrated where the ploughing force F_P is plotted for increasing water volume fractions. The load-controlled ploughing force is shown in the dashed line for the experimentally set conditions ($N = 7.9$ N, $R = 52.5$ mm) where the red lines represent the indentation-imposed ploughing force for, respectively, $\delta = 1$ mm and $\delta = 2$ mm. For a set indentation the ploughing area A_P is constant and, subsequently, the ploughing force can be written as $F_P(\phi_w) = P_h(\phi_w)A_P$. Therefore, indentation-controlled sliding experiments, where the ploughing area is fixed, result in a ploughing force that is proportional to the hardness.

Here we quantify the penetration hardness based on the ploughing track and normal force when sliding tangentially. The penetration hardness of wetted granular materials can also be measured by performing indentation experiments as introduced in Chapter 2 and performed in Chapter 4 which results in qualitatively similar nonmonotonic behaviour of the penetration hardness as a function of the water content.

The influence of the large variation of the hardness with the water fraction is not restricted to pulling a sphere over wetted sand. For example, the impact cratering of a sphere in a granular material depends strongly on the water fraction. Marston et al. [84] present experimental results for the penetration of a solid sphere when released on a granular material. The minimum penetration depth of the object (corresponding to a zero-impact speed) and yield stress of the granular material reveal qualitatively similar nonmonotonic behaviour as a function of increasing water fractions compared to that found here for the width of the ploughing track and the penetration hardness. Furthermore, the hardness-controlled ploughing quantified here is not specific for granular materials as ploughing is a typical form of wear that is generally encountered when one of the two materials is much harder than the other. In metal-metal systems, the increase of friction with penetration depth is well known [45,46]. Friction on ice for instance, depending on the conditions, can be dominated by ploughing. In Chapter 5 we measure the penetration hardness of ice and the sphere-on-ice sliding friction as a function of temperature and speed. Close to the melting point ploughing behaviour is observed; the slider penetrates the ice and leaves ploughing tracks on the ice surface. Our simple ploughing model also captures the evolution of sphere-on-ice friction.

3.5 Conclusion

We have presented sliding experiments of a hemisphere on wetted sand in which we imposed the normal force and measured the pulling force and the width of the ploughing track. For a given normal force, both the pulling force and the width of the ploughing track show a minimum for a water volume fraction of around 10%, where the measured penetration hardness of the water-sand mixture is maximal. This behaviour is fully consistent with the ploughing model in which the sphere-on-flat geometry is exploited to express the friction coefficient as a function of the normal force and penetration hardness (or ploughing track radius).

CHAPTER 4

Sliding friction on wet sand

In this chapter, we present sliding experiments of a sledge on partially water-saturated sand and show that the frictional response is controlled by the penetration hardness of the granular medium. Adding a small amount of water to sand increases the hardness which results in a decrease of the sliding friction. Pouring even more water onto sand results in a decrease of the hardness and a subsequent increase of the friction. This inverse correlation between hardness of a wetted granular material and its frictional response to sliding is found to be due to ploughing of the sledge. Similar to the sphere-on-flat geometry as presented in the previous chapter, a sledge-on-flat geometry exhibits ploughing when the penetration hardness of the water-sand mixture is exceeded which is evident by a trace of the slider left after its passage. The penetration hardness sets how deep the trace of the slider is which, in turn, controls the ploughing force. Consequently, increasing the hardness of the water-sand mixtures makes pulling a sledge over it easier. In addition, we quantify the critical shear strain which sets the transition of an elastic to plastic response of (wet) granular materials which enables us to directly relate the shear modulus, in the elastic regime, to the hardness, in the plastic regime.

4.1 Introduction

In the previous chapter we have shown that water has a large influence on the mechanical response of sand. With a small amount of water, a pile of sand can be made into a sandcastle where, however, too much water results in a muddy puddle [83]. Similarly, walking on dry or very muddy sand takes effort while, on the other hand, walking on sand that has been wetted with an intermediate water volume fraction is easier.

For a sphere-on-flat geometry the penetration hardness, the critical yielding pressure for plastic flow, as a function of the water volume fraction was quantified in Chapter 3. Initially, adding water increases the hardness of the granular material due to formation of liquid bridges between neighbouring grains, this is the so-called 'pendular regime' [85, 86]. The water-sand mixture can resist a larger load before the penetration hardness is reached whereafter the material will irreversibly deform. Deformation of the granular material results in reorientation of the grains including breaking and rebuilding of capillary bridges. Pouring even more water onto the sand decreases the strength of the capillary bridges [51]; the 'funicular regime' is reached. Furthermore, a high water volume fraction eventually results in coalescence of the liquid bridges, the 'capillary regime', which decreases the plastic response of the

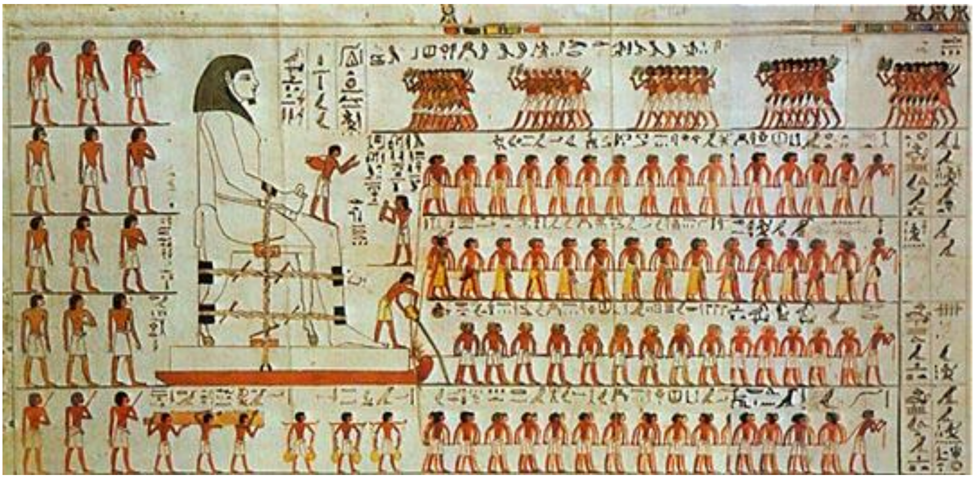

Figure 4.1: A wall painting from 1880 B.C. on the tomb of Djehutihotep [4]. A sledge with a big statue is pulled through the desert, where a person is painted who pours water onto the sand.

granular material even more.

The observed ploughing of a hemisphere through the water-sand mixture (Fig. 3.3) is controlled by the penetration hardness. For a low hardness, the hemisphere sinks into the wetted sand and leaves a deep trace into it for which a high ploughing force is observed. Increasing the hardness by adding some - but not too much - water to the sand decreases the ploughing friction as the slider remains superficial.

For a sledge sliding on sand a qualitatively similar nonmonotonic behaviour of the friction as a function of water fraction has been observed before [6]. Arguably, the ancient Egyptians, who transported statues and pyramid blocks per sledge through the desert, were aware of this as their tomb drawings show a person pouring water onto the ground in front of their sledge [4]. It therefore appears that the nontrivial relation between sliding friction on a granular material and water content of a granular material has been exploited for thousands of years. It was previously shown that the friction decreases roughly linearly with the increase in shear modulus, which suggests that when the sand is 'stiffer', the friction force decreases [6]. The shear modulus G' of a water-sand mixture quantifies the plastic response on deformation which, similar to the penetration hardness, behaves nonmonotonically as a function of the water fraction. Adding some water increases the shear modulus of the wetted sand which, with continuously increasing the water fraction, decreases again [51,87].

However, if the slider leaves a trace in the sand after its passage, the granular medium is responding plastically rather than elastically and the (linear) elastic modulus is not the pertinent quantity to consider. Sand grains irreversibly move when a critical pressure, the penetration hardness P_h, is reached. Therefore, the sliding friction is controlled by the hardness of the material instead of the linear shear modulus. In this chapter, we present sliding experiments coupled with hardness measurements for increasing water volume fractions and show that the sliding friction is a result of the plastic response of the granular material. Furthermore, the transition from the elastic to the plastic regime is unravelled which enables us to explain the link between hardness and stiffness.

4.2 Experiments

The sliding experiment is performed by pulling a wooden sledge (10.3 cm by 6.8 cm with a total mass 273 g) horizontally (as described in Section 2.1.1, although performed with a different stepper motor) at a sliding speed of 2 cm/s over a well-mixed water-sand mixture of known composition. The 'Iranian sand', which contains mainly grains in the $212 - 500$ μm range, is first dried in an oven (150 °C) and cooled down to room temperature. Demineralised water is gradually added up to a given water volume fraction and the thoroughly mixed water-sand mixture is instantly used. The sledge is pulled over a distance of 10 cm; after 2 cm a stable friction force is reached, see Figure 4.2(a). The friction force is monitored and the friction coefficient is calculated.

After sliding, the penetration hardness P_h of the water-sand mixture is measured on the same sample with an indentation-experiment. The indenter, a cone with apex angle $\alpha = 75°$ and base-radius $R = 5.05$ mm, is pushed vertically at an imposed speed of 0.1 mm/s in the water-sand mixture and indentation depth δ for increasing loading force N is monitored [see Fig. 4.2(b)]. The penetration hardness is quantified as described in Section 2.2.

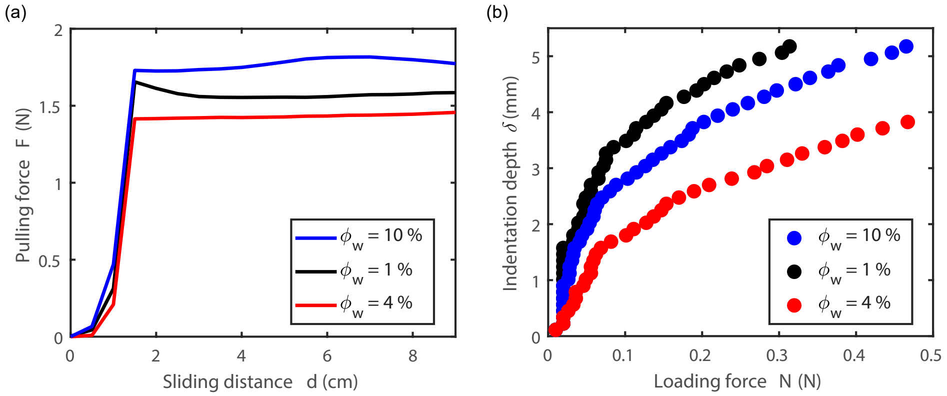

Figure 4.2: Typical results for sliding on and indentation of the water-sand mixtures. (a) The monitored pulling force F as a function of the sliding distance d for water volume fractions ϕ_w of 10%, 1%, and 4% in sand. (b) The measured indentation depth δ as a function of the loading force N measured directly after the sliding experiment. In this hardness test a conical indenter with apex angle $\alpha = 75°$ and base-radius $R = 5.05$ mm is used.

4.3 Results and discussion

4.3.1 A sledge on wet sand

The friction coefficient of a sledge sliding over a water-sand mixture is measured for increasing water volume fractions ϕ_w, see Figure 4.3 (blue squares). Adding some water initially decreases the friction coefficient where, when more water is added, the friction increases again. This nonmonotonic behaviour is qualitatively in agreement with earlier measurements where the optimum volume fraction, here 4%, is set by the grain size distribution of the used granular material [6,88]. After each sliding experiment, the slider leaves a trace in the water-sand mixture marking the width and sliding distance of the sledge. This so-called ploughing track indicates that, indeed, during sliding, the water-sand mixture is plastically deformed.

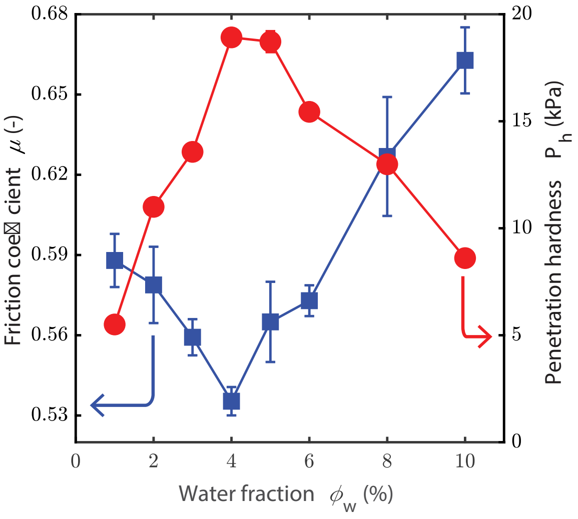

Figure 4.3: Evolution of the friction coefficient μ (blue squares) and the penetration hardness P_h (red circles) for the water volume fraction ϕ_w. The friction coefficient obtained from the measured friction force (for a fixed normal force of 2.7 N) displays a nonmonotonic behaviour for increasing water volume fractions. A similar nonmonotic behaviour for increasing water volume fractions is found for the obtained penetration hardness where the minimum in friction corresponds to the maximum in hardness at the water volume fraction of $\phi_\mathrm{w} = 4\%$. The error bars represent the standard deviation.

The deformation of the water-sand mixture is a result of the pressure exerted by the sledge along the normal direction which exceeds the critical pressure of the granular material. In Chapter 3 the penetration hardness P_h is calculated based on the observed ploughing track and normal force along sliding. By performing an indentation-experiment with a conical indenter, a qualitatively similar dependence of the penetration hardness with the water volume fraction is observed (Fig. 4.3 red circles). Note that both the magnitude and water volume fraction domain is significantly smaller compared to the observed penetration hardness in Chapter 3. We interpret both observed decreases based on the smaller average grain sizes of the used sand here and the less firm packing of the wet sand prior to the tests [51,88,89]. The nonmonotonic behaviour of the sliding friction and the penetration hardness for increasing water volume fractions indicates a direct relation between the two; for increasing hardness of the water-sand mixture, pulling a sledge over it becomes

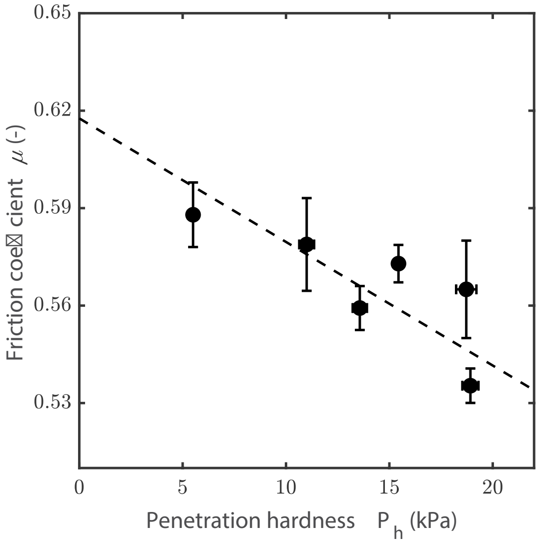

Figure 4.4: Parametric plot of the friction coefficient μ as a function of the penetration hardness P_h, both obtained as a function of the water volume fraction ϕ_w as given in Fig. 4.3. A roughly linear decrease of the friction coefficient for increasing hardness is found; it becomes easier to slide over a hard water-sand mixture. Note that water volume fractions higher than 7% are excluded from the analysis, high water fractions ('slurry sand') results in a very heterogeneous water and air distribution in the sand packing.

easier. This is quantified in Figure 4.4 where the sledge-on-sand friction coefficient is shown to decrease approximately linearly with increasing penetration hardness.

4.3.2 The transition from elastic to plastic response of wet sand

The sliding friction coefficient therefore decreases linearly with increasing shear modulus G' [6]; here we show that this linearity is also retrieved for the penetration hardness P_h of the water sand-mixture. The question then remains how the elastic and plastic response relate to each other. The water-sand mixture can hold a finite

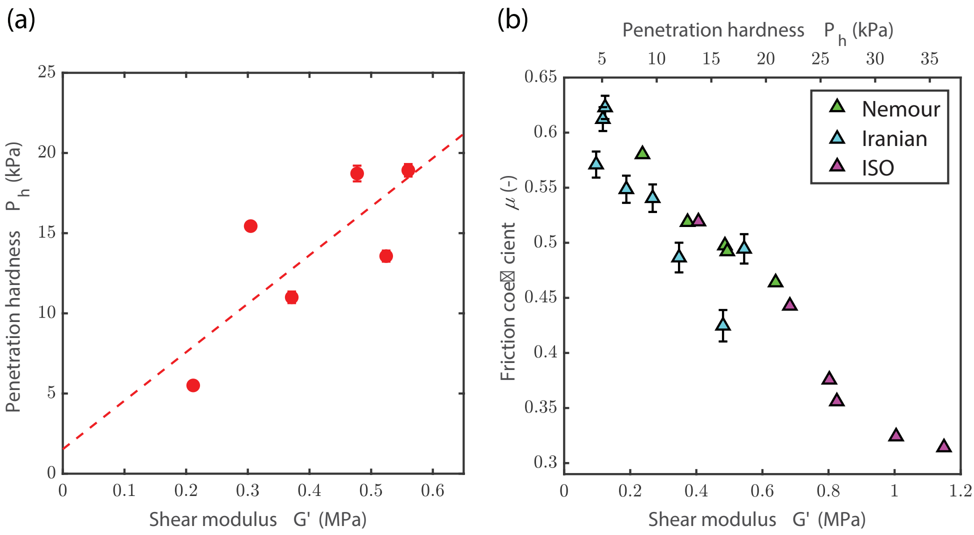

Figure 4.5: **a)** The penetration hardness P_h as a function of the shear modulus G' for different water volume fractions in sand. The shear modulus, reused from Fig. 4*b* in Ref. [6], and the penetration hardness are both obtained with so-called 'Iranian sand' (grain sizes of $212 - 500$ μm). A roughly linear dependence is found: $P_\mathrm{h} = \gamma_\mathrm{c} G' + 1528$ with $\gamma_\mathrm{c} = 0.030$ the critical shear strain. **b)** The friction coefficient μ as a function of the shear modulus G' for three sand types, reused from Fig. 5 in Ref. [6]. Furthermore, on the upper x-axis the penetration hardness P_h is given derived from the linear dependency with the shear modulus. The three sand-types 'Nemour', 'Iranian' and 'ISO', with, respectively, grain sizes in the ranges of $150 - 300$ μm, $212 - 500$ μm and $100 - 1000$ μm, were mixed with varying amounts of water.

deformation in the elastic regime before it fails whereafter a plastic (irreversible) deformation occurs. This finite deformation, the critical shear strain γ_c, defines the transition between elastic and plastic behaviour. To be able to quantify this critical shear strain, we can use the measured penetration hardness and shear modulus as a function of the water volume fraction. The latter was published previously for 'Iranian' sand for the same range of water volume fractions, see Figure 4 from Fall et al. [6]. The penetration hardness increases linearly with the shear modulus, see Figure 4.5(a), as $P_\mathrm{h} \sim \gamma_c G'$ with $\gamma_c = 3\%$ the critical shear strain. The critical strain of yielding is a constant for the given system and does not depend notably on the water volume fraction. For soft solids in general, it has indeed been shown that the critical shear strain for a given system (emulsion, microgel suspensions, foams, gels) is reasonably constant [90].

The puzzle from the data of Fall et al. is that the friction coefficient decreases linearly for increasing shear modulus for different types of sand. Now, using the relationship between penetration hardness and shear modulus, we can calculate the penetration hardness for various types of sand as shown in Figure 4.5(b). The observed linear dependence of the friction coefficient on the hardness is a result of the geometry, in this case a flat slider over a flat sand surface. For a sphere-on-flat geometry, as presented in Chapter 3, a quantitative relation is found for the hardness dependency of the friction coefficient ($\mu \sim P_\mathrm{h}^{-1/2}$). Due to the simple geometry, the relevant contact areas in the normal- and tangential direction can be calculated based on the measured ploughing track which, in the end, controls the friction coefficient for sliding. A peculiar pressure dependent friction was shown before by Crassous et al. [73] for sliding along a sandy slope. Objects on an inclined granular surface close to the avalanche threshold only slide for a narrow range of applied pressures. Sliding occurs only when the granular surface may be slightly deformed by the slider weight, but not enough to create a rim able to stop the object.

These results therefore show that the relation between the sliding friction and the (linear) shear modulus shown in Fall et al. [6] can be understood by considering the (non-linear) penetration hardness that turns out to be roughly proportional to the shear modulus [Fig. 4.5(a)]. The penetration hardness then allows for a quantitative explanation of ploughing friction.

4.4 Conclusion

In conclusion, we have performed sliding experiments of a sledge on wetted sand and measured the penetration hardness of this granular material. A roughly inverse correlation between the penetration hardness and sliding friction coefficient is obtained, which is due to ploughing. During sliding, the sledge irreversibly moves the grains, as is evident by a trace in the sand after the passage of the sledge. This trace is less pronounced if the hardness is increased by adding a small amount of water to the sand which, subsequently, results in less friction. Therefore, increasing the hardness of the water-sand mixtures makes pulling a sledge over it easier. This seems already to be experienced by the ancient Egyptians, where by pouring water in front of a sledge the sliding friction is decreased.

Pulling a sledge over sand results in irreversible movement of the grains and therefore the water-sand mixture is responding plastically. However, the mixture can hold a finite deformation elastically where the ‘stiffness’ can be quantified by the shear modulus G'. We found that the penetration hardness increases linearly with increasing shear modulus as $P_\mathrm{h} \sim \gamma_\mathrm{c} G'$ with $\gamma_\mathrm{c} = 3\%$ the critical shear strain which sets the transition from elastic to plastic response. Therefore, after the critical shear strain, the granular material will respond plastically and ploughing will occur. The transition from elastic to plastic deformation and the amount of ploughing during sliding is of interest in many applications, where sliding of a sledge over sand is one of them.

CHAPTER 5

Sliding friction on ice

We present sphere-on-ice friction experiments as a function of temperature, contact pressure, and speed. At temperatures well below the melting point, friction is strongly temperature dependent and follows an Arrhenius behaviour, which we interpret as resulting from the thermally activated diffusive motion of surface ice molecules. We find that this motion is hindered when the contact pressure is increased; in this case, the friction increases exponentially, and the slipperiness of the ice disappears. Close to the melting point, the ice surface is plastically deformed due to the pressure exerted by the slider, a process depending on the slider geometry and penetration hardness of the ice. The ice penetration hardness is shown to increase approximately linearly with decreasing temperature and sublinearly with indentation speed. We show that the latter results in a nonmonotonic dependence of the ploughing force on sliding speed. Our results thus clarify the complex dependence of ice friction on temperature, contact pressure, and speed.

5.1 Introduction

It is commonly believed that ice is slippery due to the presence of a layer of liquidlike water on the surface of ice which acts as a lubricant. However, the origin of this layer and the resulting lubrication have been and remains debated for more than 150 years [91–104]. The lubricating layer that allows ice skating has been attributed to pressure-induced [92] or friction-induced [93] melting of the ice surface and to the presence of a premelted layer of ice [94]. More recently, authors have suggested that the diffusion of water molecules over the ice surface is responsible for low ice friction at high temperatures and low sliding speeds [105]. Furthermore, reciprocated ball-on-ice friction measurements performed using a tuning fork have recently revealed that -during reciprocated sliding [106] on ice- a lubricating, viscous mixture of liquid water and ice particles dominates the frictional behaviour [107]. In the context of each of these proposed lubrication mechanisms, the local contact pressure exerted at the slider-on-ice interface is a crucial parameter that remains ill understood.

In this chapter, we therefore take a closer look at this local contact pressure and show that (i) the hardness of ice displays a strong temperature and strain rate dependence that, close to melting, leads to rich ploughing behaviour that is controlled by the temperature, sliding speed, surface topography, and surface geometry; (ii) friction on ice increases exponentially with the local contact pressure, suggesting that this pressure frustrates the mobility of the lubricating layer; (iii) in the water-immersed sphere-on-artificial ice experiment, we observe the onset of mixed lubrication at sliding speeds above 1 m/s, indicating that most of our ball-on-ice experiments are likely boundary lubricated.

5.2 Experiments

To investigate the slipperiness of ice, we move a spherical slider over an ice surface. The custom-made circular sliding setup is adapted, see Section 2.1.2 for more details, where the slider is clamped and rotated at a distance of 5 mm from the rotation axis. The imposed rotation speed and the measured torque can thus be converted into a sliding velocity and a friction force, respectively. We vary the sliding speed from 10^{-6} up to 10^{-1} m/s and measure the normal force N and friction force F exerted at the slider-on-ice interface. The flat ice surface with a controlled temperature is established by repeatedly adding a small amount of demineralised water on top of the already-frozen water. As the added water initially melts the top surface of the

Material	Radius (mm)	Roughness (nm)	Hardness (GPa)	Elastic modulus (GPa)	Poisson's ratio (-)
Silicon carbide	0.75, 6.00	140	27.0	410	0.14
Soda-lime glass	1.84	98, 222, 575, 3077	5.7	65	0.22
Sapphire	1.59	28	21.6	2	0.29
Stainless steel	≈ 22	856	2.0	200	0.28

Table 5.1: Mechanical and geometrical details of the sliders used in the friction experiments.

ice, a smooth polycrystalline ice surface is formed.

As sliders, we use silicon-carbide spheres (from Latech), soda-lime glass spheres (from SiLibeads), a sapphire sphere (from Edmund Optics) and a model ice skate (stainless steel), see Table 5.1 for details. The microscopic surface topography of the sliders is measured by laser-scanning profilometry as described in Section 2.3. We do not observe significant changes in the surface topography of the sliders after the friction experiments and therefore conclude that the sliders do not wear during the friction experiments. The surface roughness values listed in Table 5.1 refer to the root-mean-square (rms) height variation S_q from the profilometry experiments, after subtracting the curvature of the spheres. As the surface roughness is known to influence the local contact pressure at interfaces, we vary the surface roughness of the soda-lime sliders by inserting them one at a time in a container with sandpaper walls and shaking them for 2 hours to obtain a roughened surface. By varying the sandpaper grits (P3000, P2500, and P150), the resulting surface topography can be controlled ($S_\mathrm{q} = 222$ nm, 575 nm, and 3077 nm, respectively). To approximate an ice-skate-on-ice interface in the experiments, we cut a 5-mm piece out of an actual ice skate. This model skate has a width of 1.67 mm and a radius of curvature (along the length) of 22 m. The front and back edges of the model skate are rounded off.

To quantify the penetration hardness P_h of the ice, we perform indentation experiments in which a stainless-steel sphere with radius $R = 1.6$ mm is pushed onto the ice at various temperatures and preset indentation speeds v_ind, resulting in plastic deformation of the ice. The indentation depth δ and indentation force N are measured up to a maximum load of 80 N, see the Appendix A.1. The penetration hardness is quantified over the measured indentation range from 25 to 75 N; for more details see Section 2.2.

Using the mechanical properties of the slider and the ice and the surface topography of the slider, we perform contact calculations as described in Section 2.4 to solve the elastoplastic contact equations through a numerical boundary element model. Here, we make use of the fact that the ice surface has an elastic modulus and Poisson's ratio of 0.75 GPa and 0.33, respectively [108]. The hardness is measured independently as a function of temperature and velocity. As the surface roughness of ice is relatively low [$S_\mathrm{q} = 61$ nm, calculated for the measured surface topography of Figure 5.3(b) bottom] and without a long-range curvature, the surface topography of the sliders dominates the contact calculations. Including the ice topography raises the contact pressure only 4%, and, therefore, the surface topography of ice can be neglected.

5.3 Results

5.3.1 Temperature dependence

Figure 5.1 shows the friction coefficient μ as a function of temperature for the two types of SiC spheres and the model skate. In agreement with earlier measurements [108], we find that the temperature dependence of the friction coefficient can be captured by an Arrhenius-type equation:

$$\mu = c\, e^{\Delta E / k_\mathrm{B} T}\,, \tag{5.1}$$

with fitting parameter $c = 1.5 \times 10^{-4}$ and activation energy $\Delta E = 11.5$ kJ/mol. As reported in Reference [108], this activation energy matches the activation energy for ice-surface diffusion [109, 110], suggesting that the diffusion of water molecules over the ice surface plays an important role in ice friction. For temperatures above -20 °C, the spherical slider displays a friction coefficient that is higher than the friction coefficient predicted by the Arrhenius equation and increases with temperature up to the melting point of ice. This increase in friction with temperature is the result of ploughing friction; the slider plastically indents the ice in the normal direction and consequently ploughs through the surface in the lateral direction [111]. The pressure that the slider exerts on the ice surface controls the magnitude of the ploughing force.

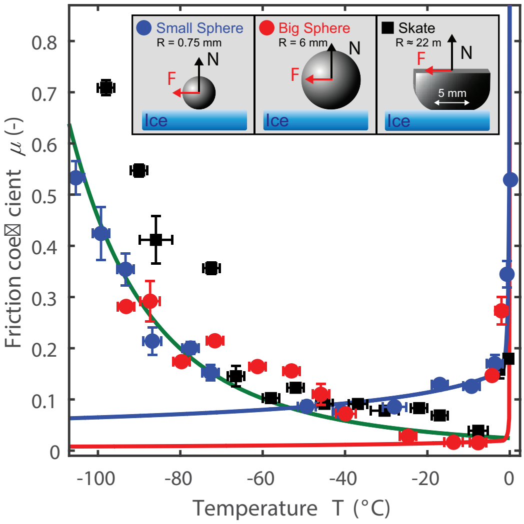

Figure 5.1: Friction coefficient μ as a function of the temperature T for various sliders on ice. At a constant sliding speed v_s of 0.38 mm/s, a small sphere (radius $R = 0.75$ mm, blue circles), a big sphere ($R = 6$ mm, red circles), and a model ice skate ($R \approx 22$ m, width 1.67 m, and length 5 mm; black squares) are slid over an ice surface at a normal force of 2.5 N. Far from the melting point, the friction coefficient follows an Arrhenius temperature dependence with an activation energy of $\Delta E = 11.5$ kJ/mol. Close to the melting point, the friction coefficient increases rapidly as the sliders start to plough through the ice. The error bars represent the standard deviation.

To further investigate the influence of contact pressure and quantify the ploughing force, we vary the contact pressure exerted by the slider by varying its curvature.

5.3.2 Ploughing

In Chapter 3 we have discussed the sliding of a spherical slider ploughing through partially water-saturated granular materials. The presented ploughing model quantitatively reproduces the measured ploughing force based on the geometry and the hardness P_h of the material. The model is not specific for granular materials as ploughing is a typical form of wear that is generically encountered when one of the two contacting materials is much harder than the other. The ploughing force for the measured sphere-on-ice geometry can be calculated by considering plastic indenta-

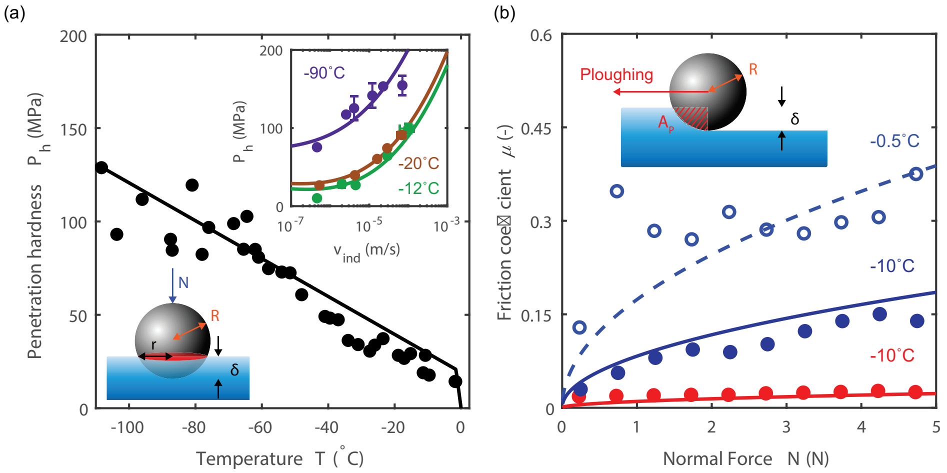

Figure 5.2: (a) Penetration hardness P_h of ice as a function of temperature, obtained from indentation experiments at a speed of $v_\mathrm{ind} = 3.8\ \mu\mathrm{m/s}$. Indentation is performed with a sphere pushed into the ice at various temperatures; see inset (left bottom) for a schematic illustration. The indentation depth δ and force N are monitored to calculate the P_h. The error bars, defined by the standard deviation in the penetration hardness, are smaller than the symbols used. A linear decrease of P_h with temperature is found (black line) up to -1.5 °C when pressure-induced melting sharply decreases the hardness. Upper inset: P_h versus v_ind for various temperatures. (b) Friction coefficient μ as a function of the normal force N for a small (radius $R = 0.75$ mm, blue open and filled circles) and large ($R = 6.00$ mm, red filled circles) SiC spherical slider. The ploughing model [lines, Eq. (5.2)] matches the observed friction coefficient. Inset: schematic illustration of ploughing in ice. The spherical slider of radius R indents the ice in the normal direction with a depth δ and cross section A_P.

tion in the normal direction, which occurs when the contact pressure exceeds the penetration hardness P_h of the ice. This penetration hardness decreases linearly with increasing temperature [see Fig. 5.2(a)] up to -1.5 °C when pressure melting sharply decreases the hardness. Similarly as described in Chapter 3, the sphere plastically indents the ice with a depth δ until the contact area A_c has increased enough to support the imposed normal force N [see inset Fig. 5.2(b) and Appendix A.1]. This indentation results in scratching laterally into the ice with a ploughing area A_P and a ploughing force F_P which, based on the geometry, results in a ploughing friction coefficient:

$$\begin{aligned} \mu_{\mathrm{P}} &= \frac{A_{\mathrm{P}} P_{\mathrm{h}}(T)}{N} \\ &= \frac{4\sqrt{2}}{3\pi^{3/2} R} \sqrt{\frac{N}{P_{\mathrm{h}}(T)}}\,. \end{aligned} \tag{5.2}$$

Figure 5.2(b) indeed confirms that both a decrease of the radius (red-filled compared to blue-filled circles) and a decrease of hardness (blue-filled compared to blue open circles) result in an increase in ploughing force; the ploughing model captures the experimentally measured variations in the friction coefficient without adjustable parameters. This result is also reflected in the different amounts of ploughing for different spherical sliders observed in Figure 5.1.

These insights into the phenomenon of ploughing translate to the practice of ice skating. During ice skating, low sliding friction is desired to achieve a high sliding speed, but, simultaneously high friction is required to enable changing the sliding direction. Therefore, the blades of ice skates have a large radius of curvature in the sliding direction, $R = 3 - 22$ m, and sharp edges with a flat or even negative radius of curvature along the width [112]. A low coefficient of friction can be expected if the skate is perfectly aligned with the ice surface, but if the skate is tilted, a quick increase of the friction coefficient is found [96, 113]. A tilt of the skate results in (deeper) indentation of the ice and therefore an increase of the friction, particularly in the direction perpendicular to the length of the skate because sliding in this direction involves a larger ploughing area. This larger ploughing force gives the skater the opportunity to push forward and make turns. In Figure 5.1, the friction coefficient of a 5-mm section of a long skate blade is measured as a function of temperature (black squares). A large decrease of the friction coefficient with increasing temperature can be found up to -8 °C, whereafter the friction increases again due to ploughing. The minimum friction for the model ice skate is found for $T = -7.7 \pm 2.3$ °C with $\mu = 0.039 \pm 0.003$.

Therefore, sliding on ice is largely temperature dependent and can be captured with an Arrhenius-type equation in the elastic regime. Close to the melting point, when the slider plastically indents the ice surface, the friction coefficient increases due to ploughing, where the magnitude of ploughing is set by (a) the hardness of the ice, (b) the slider geometry (radius of curvature), and (c) the exerted normal force.

5.3.3 Local contact pressure

Conventional liquid lubrication is essentially a competition between squeeze flow and sliding (or rolling) induced entrainment of the lubricant. The squeeze flow is driven by an externally applied normal force, which sets the local pressure experienced by the lubricant. To investigate the influence of this local contact pressure on the slider-on-ice friction, we vary the microscopic surface topography of the spherical slider; the sharper the roughness peaks on the slider, the higher the local contact pressure [114]. In Figure 5.3(a), we report the friction force as a function of normal force, measured for glass spheres with surface roughnesses S_q from 98 nm to 3077 nm. We find that the smoothest sphere displays a friction coefficient that is equal to that reported in Figure 5.1 at the corresponding temperature, here set to -50 °C, and described by the Arrhenius equation, Equation (5.1). The spheres with higher surface roughness, and therefore a higher contact pressure, display a significantly higher friction coefficient. For $T = -30$, -70 and -90 °C, a qualitatively similar result is found.

To quantify the contact pressure P_c, we perform contact calculations in which the mechanical properties of the slider and the ice, and the measured surface topography of the slider form the input. The interfacial gap, at each of the in-plane coordinates defined by the topography, forms the output of the calculation for a given normal force. Those locations at which the interfacial gap is zero form the area of real contact where, in addition, the local contact pressure is quantified. See Section 2.4 for a full description of the contact calculations including the comparison to elastic and plastic contact mechanics models. In Figure 5.3(c), we plot the measured surface topography and the calculated area of real contact for glass spheres with increasing roughness at a temperature of -50 °C. We find that the relatively smooth spheres [$S_\mathrm{q} = 98$ nm; Fig. 5.3(c), left panel] primarily deform the ice elastically at an average contact pressure of 35 MPa. This result is independent of temperature because the elastic modulus of the ice (and the slider) does not change significantly with temperature. The situation is different for balls with a relatively high surface roughness [$S_\mathrm{q} =$ 3077 nm or higher; Fig. 5.3(c), right panel]. As the surface roughness is increased above this level, the calculated average contact pressure increases up to 85 MPa, which equals the hardness of the ice, indicating that plasticity plays an important role in the contact formation for these rougher spheres. The hardness of the ice decreases linearly with temperature and limits the maximal contact pressure; the contact pressure in this regime of plastic deformation varies from 130 MPa at -90 °C to 70 MPa at -30 °C (see Appendix A.3). Note that the contact pressure in both the

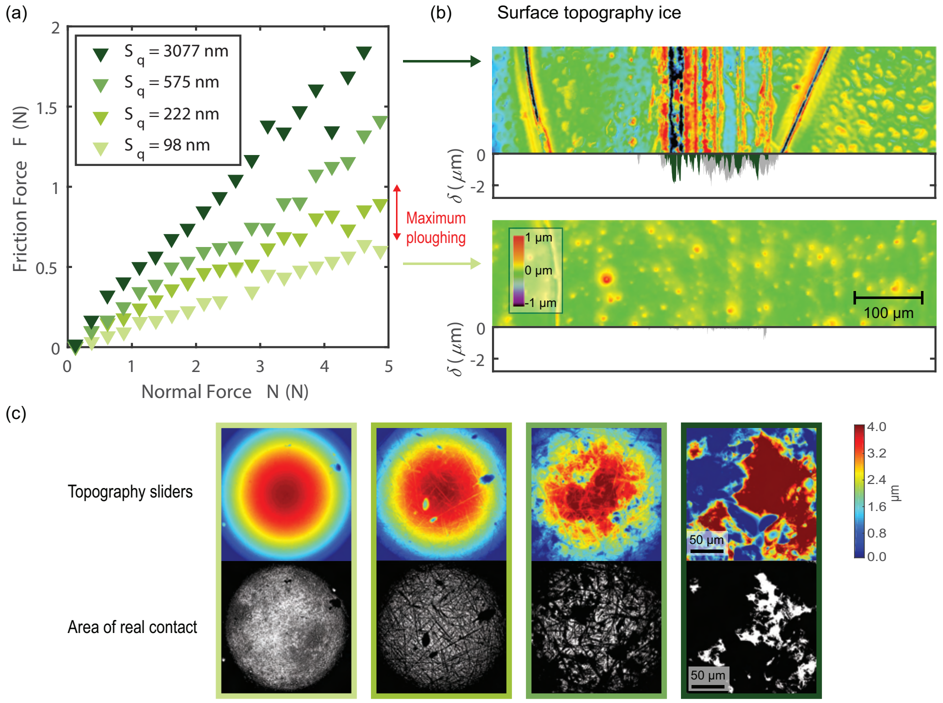

Figure 5.3: (a) Friction force as a function of normal force measured for glass spheres with surface roughness S_q of 98, 222, 575, and 3077 nm at a temperature of -50 °C and sliding speed of 0.38 mm/s. The smoothest sphere displays a friction equal to that reported in Fig. 5.1, which can be described by the Arrhenius equation [Eq. (5.1)]. For increasing surface roughness, a higher friction force is measured. (b) Surface topography and corresponding ploughing depth δ in the ice after a sphere with the highest (top) and lowest (bottom) roughness slides over it at a normal force of 0.21 N. The calculated plastic indentation depth δ for a normal force of 0.21 N is added in light gray in the insets. (c) Surface topography (top) and calculated area of real contact (bottom) for the same glass spheres at $T = -50$ °C at a normal force of 0.5 N. A transition from primarily elastic contact for a smooth slider towards elastoplastic contact for a rough slider can be observed.

plastic and the elastic regime is almost independent of the normal force because the area of real contact increases linearly with normal force; see Appendix A.3.

Spheres that deform the ice plastically will plough through the ice when tangentially loaded. In Figure 5.3(b), top, we plot the ploughing track that was left on the ice after a sphere with high roughness, $S_q = 3077$ nm, slid over the ice surface with a normal force of $N = 0.21$ N and a speed of $v \approx 5$ mm/s. In contrast, spheres with low roughness $S_q = 98$ nm do not leave visible damage after sliding on the ice [Fig. 5.3(b), bottom], as expected based on the fact that the calculated average contact pressure for these balls in contact with ice is smaller than the penetration hardness of the ice. Although the plastification during sliding increases the friction force, it only provides a small contribution. The maximum friction due to ploughing, represented by the arrow in Figure 5.3(a), can only explain 30% of the observed variation in friction with roughness (see Appendix A.4). Therefore, we measure and calculate the interfacial shear stress σ_s, which is the friction force divided by the area of real contact at which the friction force is generated.

Perhaps somewhat surprisingly, in the elastic regime, σ_s increases exponentially for increasing contact pressure P_c; see inset of Figure 5.4 for -50 °C. Qualitatively similar results are found for $T = -30, -70$, and -90 °C; the lowest roughness has a shear stress expected based on the Arrhenius behaviour, while increasing the contact pressure up to the penetration hardness of the ice results in an exponential increase of the shear stress. These results are summarised in Figure 5.4 (triangles), where the contact pressure and shear stress are normalised by, respectively, the penetration hardness of the ice P_h and the Arrhenius temperature dependence of the friction coefficient $e^{\Delta E/k_B T}$. The exponential increase of interfacial shear stress with pressure is also known as piezo-viscosity; the viscosity of a confined lubricant increases exponentially with the mechanical pressure [115,116]. The viscosity η is then described empirically as

$$\eta = \eta_{\text{ref}}\, e^{\frac{P_c}{\beta}} \,. \tag{5.3}$$

Here, the pressure-viscosity parameter β sets the increase of the viscosity with the exerted pressure starting from the unconfined viscosity η_{ref}. For sliding friction on ice, a qualitatively similar process occurs; the shear stress increases when the contact pressure on the mobile layer is increased. From Figure 5.4, we can model the shear stress as:

$$\sigma_s = \sigma_0\, e^{\frac{\Delta E}{k_B T}}\, e^{b \frac{P_c}{P_h(T)}} \,, \tag{5.4}$$

with $\sigma_0 = 2.1$ kPa and $b = 3.4$. The shear stress is set by the mobility of the ice surface, which is decreased, or “frustrated”, for increasing contact pressures up to the plastic limit. The piezo-viscous effect on the shear stress could be interpreted as a result of confinement; the surface water molecules become more strongly confined at the slider-on-ice interface with increasing contact pressure. For nanoconfined water

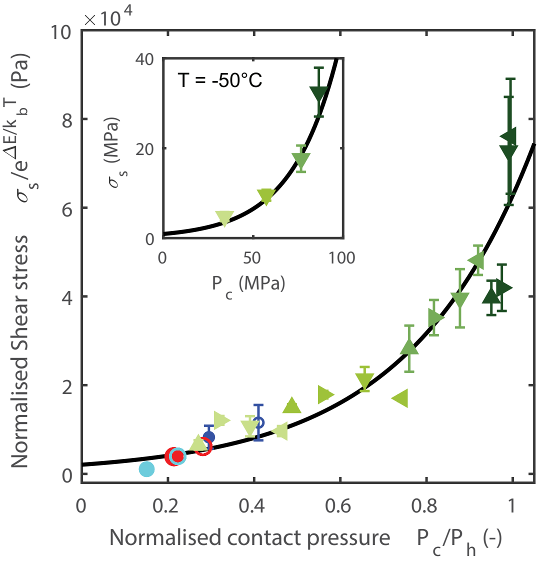

Figure 5.4: Normalised shear stress $\sigma_s/e^{\Delta E/k_B T}$ as a function of the normalised contact pressure P_c/P_h for various sliders, surface roughnesses, and temperatures at a sliding speed of 0.38 mm/s. The solid line is a fit using Eq. (5.4). Triangles from light green to dark green correspond to glass spheres with a surface roughness S_q of 98, 222, 575, and 3077 nm, where upward, right, down, and left-pointing triangles are measurements at $T = -90$, -70, -50, and -30 °C, respectively. The blue, red, and cyan circles correspond to, respectively, small SiC ($R = 0.75$ mm), a large SiC ($R = 6$ mm), and a sapphire sphere ($R = 1.59$ mm) at $T = -90$ °C for closed and -50 °C for open markers. The error bars represent the standard deviation in the measured friction force. Inset: shear stress as a function of the contact pressure for various glass sliders with increasing surface roughness at $T = -50$ °C and a sliding speed of 0.38 mm/s.

molecules, it has been observed that the (apparent) viscosity increases when the gap size is decreased to less than a nanometer [117–119]. Additionally, we include in Figure 5.4 the measurements for the small (0.75-mm radius) and large (6.00-mm radius) SiC spheres and a low-roughness sapphire sphere (1.59-mm radius). For these three spheres, the calculated shear stress and contact pressure based on the measured friction force and surface topography (T = -50 and -90 °C; see Appendix A.3) match well with the fit made for the glass spheres. A "slippery" state can therefore only be reached when the exerted contact pressure is sufficiently small, which is the case for a slider (or skate) with a small surface roughness and a large curvature.

Overall, we observe an increase of the friction force when the local contact pressure is increased. Next to, perhaps, a minor contribution due to ploughing, the increase of friction can be explained by a piezo-viscous effect; for increasing contact pressure up to the plastic limit, the shear stress increases exponentially.

5.3.4 Sliding speed

For a traditional lubricant -for example, a thick grease in a journal bearing- the friction coefficient strongly depends on the sliding velocity. As the sliding speed increases, more lubricant is entrained into the contact resulting in a pressure in the lubricant that can partially support the external load: This process is known as mixed lubrication. At yet higher sliding speeds, the friction may increase with velocity because the lubricant forms a continuous film that separates the solids and undergoes Newtonian flow: Viscous dissipation within the lubricant is responsible for the friction in the hydrodynamic lubrication regime [120, 121].

To investigate the slider-on-ice friction in the context of lubrication, we perform friction experiments at velocities ranging from 1 μm/s to 10 cm/s and find a nonmonotonic relation between friction and sliding velocity at a temperature of -20 °C [Fig. 5.5(a), red triangles]. This velocity dependence of the friction can be fully explained using a velocity-dependent ploughing model: During sliding, the slider plastically indents the ice in the normal direction at an indentation speed v_{ind} which is a fraction of the sliding speed v_{s} (approximately 4%, see Appendix A.2). Consequently, the indentation depth sets the ploughing area A_{P}, the projected cross-sectional area over which the slider ploughs through the ice. Both during indentation and (subsequent) ploughing, the velocity-dependent penetration hardness of the ice controls the normal and tangential pressure at the interface. Remarkably, the penetration hardness is highly speed dependent; for increasing indentation speed, the penetration hardness increases, as can be seen in the inset of Figure 5.2(a) for various temperatures. The hardness of ice for temperatures up to -25 °C has been studied before for various loading times when a sphere is pushed into the ice [122–124] and for various impact velocities with a short contact time when a steel sphere is dropped onto the ice [125, 126]. Although both measurement methods and the used definition of hardness vary, an increase of the hardness with decreasing temperature and increasing speed was also observed in these experiments. This observation is in qualitative agreement with our findings for a broad temperature and indentation speed domain. However, the linear dependence of the hardness on temperature in a broad domain from -110 °C almost up to melting that we report here, to the best of our knowledge, has not been observed before.

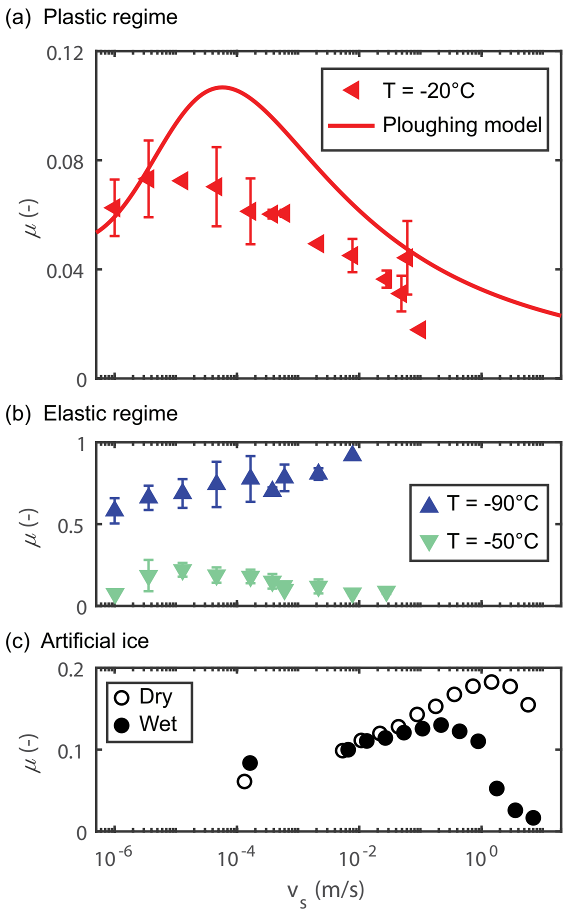

Figure 5.5: Friction coefficient μ as a function of the sliding speed v_s for a smooth glass sphere (surface roughness $S_q = 98$ nm). All measurements were performed with increasing and decreasing sliding velocity to confirm that hysteresis was absent. (a) At -20 °C (red triangles), a nonmonotonic dependence of the friction on the sliding speed is found, which can be understood based on ploughing [Eq. (5.5), red line]. (b) At -50 °C (green triangles) and -90 °C (blue triangles), velocity strengthening of the friction is observed, which can be qualitatively described as a result of a stress-augmented thermal process; the stress exerted by the slider at the interface decreases the effective activation barrier, resulting in a logarithmic increase of the stress with the rate or velocity. (c) Dry (open markers) and water-lubricated (solid markers) friction on artificial ice (HDPE) (using the same glass slider) at room temperature and at a normal force of 1 N. The error bars represent the standard deviation in the measured friction force. In panel (c), the error is of the order of the symbol size.

As the velocity domain during ice skating is broad, from standing still up to moving at about 30 m/s, the velocity dependence of the hardness of the ice is of key importance. Thus far, most calculations of friction on ice used either a constant or linear dependence of the hardness on velocity [99, 101, 127–129]. The ploughing force is set by both the penetration hardness in the normal direction (at v_{ind}) and by the penetration hardness in the tangential direction (at v_{s}). Consequently, we can write, for the friction coefficient,

$$\mu_{\mathrm{P}} = \frac{4\sqrt{2N}}{3\pi^{3/2}R} \frac{P_{\mathrm{h}}(T, v_{\mathrm{s}})}{P_{\mathrm{h}}(T, v_{\mathrm{ind}})^{3/2}} \,. \tag{5.5}$$

For the data shown in Figure 5.5(a), with a set sliding speed v_{s}, the corresponding indentation speed v_{ind} for the spherical slider with radius R and average normal force N can be calculated directly (see Appendix A.2). Therefore, without adjustable parameters, the ploughing contribution can now be calculated for the -20 °C data and, as shown with the red line in Figure 5.5(a), this calculation is in reasonable agreement with the measured friction coefficient; the ploughing model captures the nonmonotonic dependence of friction on sliding speed.

At $T = -50$ and -90 °C [Fig. 5.5(b)], we find velocity-dependencies that cannot be described based on ploughing. This result is expected as, at low temperatures, the penetration hardness of the ice increases and the ice can accommodate the normal force through elastic deformations. At -90 °C (blue markers in Fig. 5.5), we observe -in agreement with earlier measurements [108] - velocity strengthening friction; the friction coefficient increases logarithmically from a friction coefficient of $\mu \approx 0.55$ at μm/s speeds up to $\mu \approx 0.9$ for speeds on the order of cm/s. A logarithmic increase with speed has been described before for Eyring processes; a stress (or force) can effectively decrease the Arrhenius energy barrier and therefore influence the rate of the process; the Arrhenius process for the ice surface is the diffusive motion of the weakly bonded surface water molecules. In such so-called stress-augmented systems, the relation between the applied stress, or force, and the velocity is logarithmic [47, 48], like we observe here. The -50 °C case seems to be in between the behaviour of the -20 and the -90 °C cases, sharing some of the features of both. A detailed (quantitative) understanding of these observations is not available yet.

5.3.5 Substrate

As the large velocity dependence of ice friction is often attributed to water lubrication, we finally investigate the role of water lubrication in our friction experiments. We replace the ice surface with a material that has similar mechanical properties: high-density polyethylene (HDPE, elastic modulus 1.1 GPa, surface roughness of 207 nm; from Simona). In Figure 5.5(c), the dry (open circles) and water-lubricated (closed circles) friction coefficients, measured at a normal force of 1 N, are plotted as a function of sliding speed. The significant decrease of the water-lubricated friction coefficient observed at sliding speeds higher than 1 m/s indicates the onset of mixed lubrication. At larger sliding speeds, which we cannot reach using our current experimental setup, elastohydrodynamic lubrication is expected to occur. These measurements suggest that, at least up to sliding speeds of 1 m/s, the slipperiness of ice is not the result of mixed or hydrodynamic lubrication from a liquid water film. However, we note that the onset of mixed lubrication can also depend on the surface chemistry and would occur at lower speeds if the contact pressure was reduced.

Altogether, the speed dependence of sliding on ice depends strongly on the contact regime, elastic or plastic deformation. When the contact of the slider on ice is mainly elastic, as observed for low temperatures and smooth spherical sliders, the observed friction can be linked to the mobility of confined water. However, for a plastic contact, the friction is set by the amount of ploughing, which largely depends on the hardness, the slider geometry, and the exerted normal force.

5.4 Discussion

One interesting observation that merits discussion is that during ploughing, tracks and debris particles can be formed when the temperatures and contact pressures are high. Under these conditions, the dynamics of ice debris particles are expected to become important, particularly if the sliding motion is reciprocated on a relatively small section of the ice. Indeed, we have observed that when our sphere is made to oscillate over the same surface area (an option that is readily available on the rheometer) at -5 °C, the frictional response does not reached a steady state after 2 minutes. This was measured with a smooth glass sphere oscillating at a frequency of 20 Hz, with an amplitude of 100 μm and normal force of 2 N.

Another point is that the chemical nature of the slider can be of importance for the frictional behaviour. In winter sports, hydrophobic coatings are used to reduce the friction [98, 130]. Although sliding on snow, which is a soft porous media of ice and water, is very different than sliding on an ice surface, an influence of the wetting properties could be expected. In our study, the sliders (Table 5.1) are all hydrophilic, and this may explain why there is little variation in the friction that was measured with the various materials. In this context, it would be interesting to conduct similar ice friction experiments with hydrophobic materials in the future.

The thermally activated diffusive motion of surface molecules could also be interpreted as a result of the presence of a premelted (quasi)liquid water layer. This liquidlike layer, starting from one bilayer up to 45 nm, grows above a critical temperature, which has been experimentally reported in the range of −70 up to −2 °C [103, 104, 131–134]. However, in the given temperature domain, we measure a continuous decrease of the friction, independent of the presence or thickness of a liquidlike water layer. Therefore, we interpret the measured Arrhenius behaviour of the friction coefficient as a result of ice-surface diffusion.

In the mid-20th century, frictional melting of the ice was already been suggested as an explanation for the slipperiness of ice [93]. The heat locally generates a lubricating water film that, with increasing sliding velocity, eventually results in a full water film that separates the surfaces (aquaplaning). We observe that ice remains highly slippery at speeds as low as 1 μm/s for −20 °C; therefore, ice remains slippery down to very low sliding speeds, where the rate at which energy is injected into the interface becomes negligible compared to that at higher sliding speeds. This result indicates that the friction coefficient is not very sensitive to frictional heating. We interpret that, for the given microsurface and macrosurface geometry, the slipperiness up to a speed of at least 1 m/s is not the result of mixed or hydrodynamic lubrication. Additionally, the slipperiness does not vary significantly when a silicon carbide or a glass slider is used, although the thermal conductivity of these materials differs by 2 order of magnitude.

5.5 Conclusion

In summary, temperature, pressure, and speed each have an important impact on ice friction, largely through the hardness of the ice. This hardness increases with decreasing temperature and increasing strain rate (indentation speed). On the other hand, the contact pressure exerted at the slider-on-ice interface is set by the slider topography and geometry. When this contact pressure approaches the ice hardness, ploughing friction becomes dominant. This ploughing friction depends on the sliding speed because the rate at which the slider indents the ice in the normal direction and ploughs through the ice in the tangential direction varies with the sliding speed and the speed-dependent hardness. Alternatively, at contact pressures significantly below the ice hardness, no ploughing occurs, and the friction is adhesive in nature. In this elastic regime, ice friction is low and set by the mobility of the confined water at the slider-on-ice interface. Ice friction in this regime is inversely proportional to the mobility of water molecules at the free ice surface, which can be viewed as an activated process with an Arrhenius temperature dependence. Increasing the local contact pressure exerted at the slider-on-ice interface leads to increased confinement and an exponential increase in interfacial shear stress.

Ice friction is thus low due to the high mobility of the water molecules at the slider-on-ice interface at temperatures close to the ice melting point. This slipperiness can be suppressed by increasing the local contact pressure towards the ice hardness. It is the exceptionally high hardness of ice, close to its melting point, that enables the slipperiness of ice and distinguishes ice from other solids. In practice, this means that the optimal ice skate is very smooth and has sharp edges. When the smooth surface makes contact with the ice, the contact pressure, and therefore the sliding friction, is low. When the skate is tilted, the sharp edge plastically penetrates the ice, leading to high ploughing friction that enables grip, which is necessary to accelerate and turn.

CHAPTER 6

Sliding friction of geometrically controlled surfaces

It is our everyday experience that two smooth surfaces slide more easily over each other than two rough ones. Counterintuitively, roughness at the nanoscale can lead to superlubricity, where the roughness actually decreases friction to extremely low values. Structural superlubricity is a property of periodic surfaces, and is attributed to the commensurability of the two surfaces sliding past each other. Here we investigate surfaces with macroscopic periodic roughness sliding over each other, allowing to directly vary the (in)commensurability of the roughness. We show that the roughness allows to tune the friction coefficient by more than an order of magnitude, which can be explained completely by a simple geometrical model. A Kirigami metamaterial surface allows us to show that this understanding of geometrical friction can be used to externally control the friction in a single system by externally controlling its roughness.

6.1 Introduction

The resistance to sliding of objects is experienced daily, but remains ill-understood. The friction force is often specific to the conditions and, therefore, hard to predict. Various parameters such as geometry, load or surface roughness can alter the sliding friction significantly. Often, low friction is desired in biological and industrial tribological systems; it has been estimated that a third of the world energy consumption is spent on friction and, therefore, a better understanding of it would have a large impact [1]. In contrast, high friction can be beneficial as well; the rubber of a shoe on the pavement or a finger on a tennis racket desire high grip and no slip [135, 136]. A good control of friction is therefore of interest in many applications: high friction for grip and low friction for easy sliding. We show here that direct control may be achieved by controlling the (macroscopic) surface topography.

Surface roughness alters the friction force significantly; in general the larger the roughness, the larger the friction. However, the precise influence of the local surface height variation on the friction is hard to predict and control [137–140]. Often a combination of abrasion (wear, plastic deformation) [48, 141, 142], interlocking [143,144], and squeezing out the lubricant if present [37,145,146] are the main reasons for the increase of friction. At the nanoscale, the potential of controlling friction by surface topography has been shown previously [52, 53, 147–149]. Depending on the commensurability of periodic nanoscale surfaces, the friction force can be modified to extremely low values. This so-called structural lubricity enables the friction force to be controlled over a large domain based on the (in)commensurability of surface roughness [44]. In this chapter, we explore the ability to modify the friction force with macroscopic periodic surface roughness on custom-made surfaces. We show that the friction force for a dry and rigid system can be modified based on well-designed periodic surface roughness.

The use of artificial manufactured surface roughness, or surface patterning, is well established. The ridges on a bottle of water [150] or the grooves in an anti-slip floor surface [151] are designed to increase the grip. These millimetre-size ridges and grooves give the opportunity to squeeze out any (slippery) liquid and, by elastic deformation of the surfaces, they interlock which results in grip. In contrast, surface patterning on the sub-millimetre scale can be manufactured on bearing-shafts to increase the slipperiness: The surface patterning increases the durability of the lubricated system as it entraps wear debris and can act as a lubricant reservoir [152]. However, controlled friction in dry systems based on designed surface roughness is often limited by wear and rigidity.

Based on (digital) fabrication techniques, we design macroscopic roughness on rigid surfaces and measure the friction to slide one patterned surface over the other. With direct control on the (in)commensurability and slope of the periodic surface height variation, we manage to vary the friction force by more than an order of magnitude. In addition, we show that with Kirigami metamaterial surfaces the periodic surface roughness can be varied externally which, subsequently, enables direct control of the sliding friction.

6.2 Experiments

6.2.1 Sawtooth patterned surfaces

We perform sliding experiments with geometrically controlled surfaces to monitor the influence of macroscopic periodic roughness on the friction force. One of the designed surface patterns is the so-called *sawtooth*-pattern: a macroscopic periodic roughness that is based on a row of identical triangular prisms. The prisms are based on isosceles triangles with a controlled interior angle θ and depth of 20 mm. For a fixed height h of 3 mm, we fabricate the sawtooth pattern as macroscopic surface patterning for over a length of 60 mm. The top surface is pulled over a bottom surface where, for simplicity, the top surface pattern is present as a single sawtooth.

The macroscopic periodic roughness is fabricated on the surfaces of plastic, aluminium, and stainless steel objects; see also Table 6.1. The plastic surfaces are manufactured with digital fabrication techniques. A commercially available resin, named *Clear*, is 3D printed with the Form 3 (Formlabs). Based on stereolithogra-

Material name	Material type	Fabrication technique	Resolution (μm)	Roughness (μm)
Plastic	Clear	Stereolithography	25.0	3.454
Aluminium	6082-T6	Wire electrical discharge	5.0	0.705
Stainless steel	AISI 316	Wire electrical discharge	5.0	0.470
Kirigami	Mylar	Laser cutting (2.0″ lens)	1.0	0.073

Table 6.1: Details of the materials used for the custom-made surfaces. The listed resolutions are for the fabrication of flat surfaces. The listed roughness S_q is the root-mean-square surface height variation which is quantified as described in Section 2.3.

Material	Patterning	Gravitational force F_G (N)	Friction coefficient μ_0 (-)
Aluminium	Sawtooth	1.18, 1.67, 2.69	0.23 ± 0.02
Aluminium on stainless steel	Sawtooth	1.18, 1.67, 2.69	0.21 ± 0.02
Stainless steel	Sawtooth	1.53, 2.03, 3.00	0.18 ± 0.03
Plastic	Sawtooth	0.61, 1.10, 2.09	0.12 ± 0.01
Plastic	Sinusoidal 1D	0.61, 1.10, 2.09	0.12 ± 0.01
Plastic	Sinusoidal 2D	0.85, 1.34, 2.32	0.12 ± 0.01
Plastic on Kirigami	Sawtooth on Kirigami	0.32, 0.61, 1.10	0.20 ± 0.01

Table 6.2: Details of the sliding experiments performed for the various materials and surface patterns. The gravitational force F_G is controlled by placing dead weights on the slider. The listed microscopic friction coefficient μ_0 is the measured coefficient without the patterning, i.e., the plate-on-plate friction coefficient.

phy, the liquid resin is cured into hardened plastic by photopolymerization with a print-resolution (both axis and lateral) of 25 μm [153]. For the aluminium (6082-T6 aluminium alloy) and stainless steel (AISI 316) surfaces, wire electrical discharge machining is used; the patterning is fabricated by removing material with electrical discharges (sparks) from a 0.25 mm brass wire. This technique has a resolution of 5.0 μm for the fabrication of *mm*-size macroscopic surface roughness. However, the resolution of this technique is significantly less for the fabrication of high surface slopes in μm-size surface patterns. The microscopic surface topography — the microscopic surface roughness — of all materials is measured prior to sliding by laser-scanning profilometry as described in Section 2.3. The calculated root-mean-square surface height variation S_q is listed in Table 6.1.

The sliding experiments are performed with the custom-made horizontal sliding setup as introduced in Chapter 2; we pull the top surface horizontally at an imposed constant sliding speed of 1 mm/s over the bottom surface. The pulling force F_T is monitored as a function of the sliding distance d while the gravitational force F_G is controlled by placing dead weights on the slider; see Table 6.2.

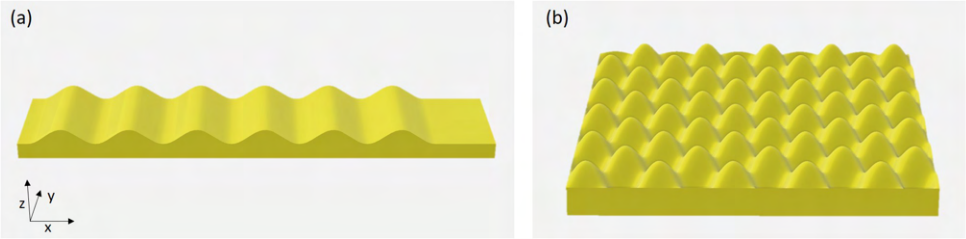

Figure 6.1: Designs for the 1D (a) and 2D (b) sinusoidal patterned surfaces. The height Z of the surface is defined by Equations (6.1) and (6.4).

6.2.2 Sinusoidal patterned surfaces

In order to study the influence of commensurability, we also design a sinusoidal pattern, 3D printed with the hardened resin *Clear*, with a length and width of, respectively, 60 mm and 20 mm (which are the same as for the sawtooth patterned surfaces). The height profile Z is defined as

$$Z(x) = b \sin(\frac{2\pi}{a} x) \,, \tag{6.1}$$

with b the amplitude and a the wavelength; see Figure 6.1(a) for the design. The angle θ of this sinusoidal patterning can be defined based on the surface slope $\tan(\theta) = \frac{\partial Z}{\partial x}$ which can be written as

$$\theta = \tan^{-1}\left(\frac{2\pi}{a} b \cos(\frac{2\pi}{a} x)\right) \,. \tag{6.2}$$

Consequently, the maximum angle of the surface pattern is:

$$\theta_{\text{max}} = \tan^{-1}\left(\frac{2\pi b}{a}\right) \,. \tag{6.3}$$

The manufactured top surface has a wavelength of $a_{\text{top}} = 5.44$ mm and amplitude $b = 1.5$ mm which results in $\theta_{\text{max}} = 60°$. Several bottom surfaces are fabricated with wavelengths starting from $a_{\text{bottom}}/a_{\text{top}} = 0.8$ up to $a_{\text{bottom}}/a_{\text{top}} = 2.4$ with a constant amplitude b of 1.5 mm.

In addition, surfaces with a macroscopic periodic roughness in 2D are fabricated, as can be seen in Figure 6.1(b). The height Z can be described as

$$Z(x, y) = b_{\text{x}} \sin(\frac{2\pi}{a_{\text{x}}} x)\, b_{\text{y}} \sin(\frac{2\pi}{a_{\text{y}}} y) \,, \tag{6.4}$$

with $a_x = a_y = 10.88$ mm, and $b_x = b_y = \sqrt{3}$ mm which results in a maximum patterning angle of $\theta_{max} = 60°$. The top and bottom surfaces have the same patterning with 5 periods in the x and y direction. For both sinusoidal patterns, the pulling force F_T are measured for sliding horizontally at a preset sliding speed of 1 mm/s for various applied gravitational forces F_G; see Table 6.2.

6.2.3 Kirigami metamaterial

We perform sliding tests in which a sawtooth patterned top surface slides on a Kirigami metamaterial surface. Kirigami is the Japanese artform of paper cutting where, with a well-designed pattern, the flat sheet reforms in a 3D structure while stretching out. We laser-cut a pattern in a Mylar sheet that has a thickness of 125 μm, a width of 50.67 mm, and a length of 85 mm. As design we use a triangular pattern, see Figure 6.2. This patterning is based on an array of unit cells (see the black lines in Fig. 6.2) where the unit cell is a rhombus; a quadrilateral where all four sides have the same length l_0. Two straight cuts (red line in Fig. 6.2) along the sides of the unit

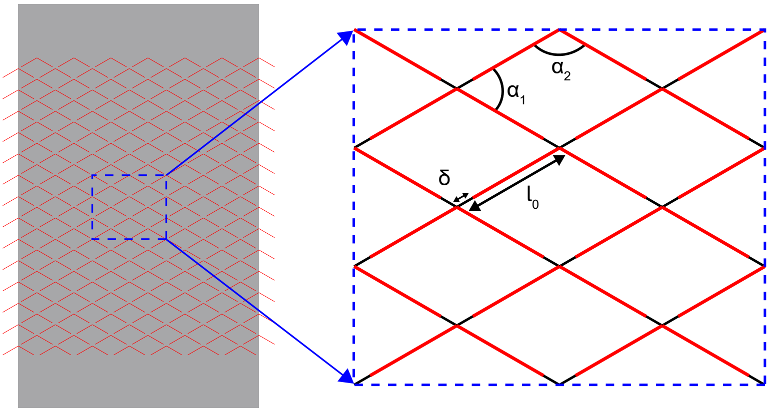

Figure 6.2: Design for the Kirigami metamaterial surface made with a 125 μm thin Mylar (polyethylene) sheet, see the gray area. The red lines represent the cuts fabricated in the sheet; the periodic patterning is based on a unit cell that is arranged in a triangular lattice. The unit cell (black lines) is a rhombus, the four sides have a length $l_0 = 4.5$ mm and the interior angles are $\alpha_1 = 60°$ and $\alpha_2 = 120°$. Two straight cuts, as represented by red lines, are made along the top two sides and, therefore, connect at the top and leave a length of $\delta = 0.7$ mm intact.

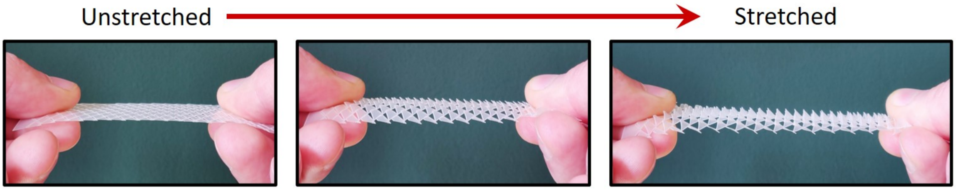

Figure 6.3: A fabricated Kirigami metamaterial surface. When the thin sheet is stretched uniaxially, the surface exhibits a roughness which consists of triangular scales pointing out-of-plane.

cell were made which are connected at the top corner and leave a length δ intact. Inspired by Reference [154], we design the Kirigami pattern with interior angles of the unit cell of $\alpha_1 = 60°$ and $\alpha_2 = 120°$, side length of $l_0 = 4.5$ mm and cuts with a length of 3.8 mm ($\delta = 0.7$ mm). The patterning is made along the full width of the sheet and for a length of $L_0 = 63.08$ mm.

The Kirigami sheets exhibit an out-of-plane roughness when stretched uniaxially; triangular 'scales' are formed where the height of the formed roughness can be amplified with the set strain as can be seen in Figure 6.3. In the sliding experiments, we have clamped both long sides of the Kirigami patterned sheet and, with the use of a micro-screw, stretch it uniaxially up to a length L. Consequently, we monitor the strain ϵ which is defined as

$$\epsilon := \frac{L - L_0}{L_0}\,, \tag{6.5}$$

where L and L_0 are, respectively, the deformed and undeformed length of the Kirigami patterned part of the surface. For a set strain, we quantify the horizontal pull force F_T when sliding against and along the formed Kirigami-scales at various applied gravitational forces F_G, see Table 6.2.

6.3 Results

6.3.1 Macroscopic periodic roughness controls friction

Experimental results

We start by discussing the results for the *sawtooth* patterned surfaces. A top surface with a single triangular prism is slid horizontally over a surface with the designed sawtooth pattern [Fig. 6.4(a) top]. The pulling force F_T as a function of the sliding distance d is monitored which results in a square-wave function [Fig. 6.4(a) bottom]. When the slider moves uphill over the bottom surface, a high and constant tangential force is measured. Subsequently, when the top of the sawtooth pattern is reached, the force drops and a constant (negative) force is found up until the slider is back down again.

The plateau values F_{max} and F_{min} for, respectively, uphill and downhill sliding

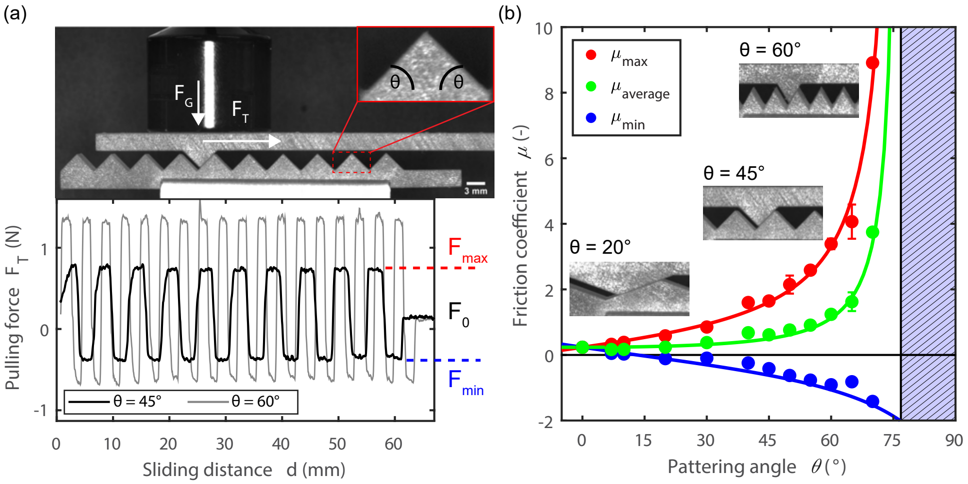

Figure 6.4: Sliding experiments with sawtooth patterned surfaces. (a) Experimental setup visualised from the side of the sliding experiment and the monitored pulling force F_T as a function of distance d. As macroscopic roughness, a sawtooth pattern is fabricated with a fixed height of 3 mm and controlled angle θ. The observed square wave of the pulling force is shown for $\theta = 45°$ and $\theta = 60°$ in, respectively, black and gray. (b) Friction coefficient μ as a function of the angle θ for the maximum (red), average (green) and minimum (blue) friction, either measured (circles) or calculated (continuous lines) with Eqs. (6.8) to (6.10).

are set by the angle θ of the sawtooth pattern. The magnitude of both F_{max} and F_{min} increase when the patterning angle θ increase. In Figure 6.4(b) the influence of the angle θ is observed for maximum (red), minimum (blue) and average (green) macroscopic friction coefficient μ which is defined as the ratio of the measured tangential to the normal (gravitational) force. The gravitational force F_{G} is given by the mass of the dead weights on top of the slider and the slider itself, see Table 6.2. The friction depends strongly on the angle θ of the macroscopic periodic roughness of the sliders; for example, the maximum friction coefficient for $\theta = 60°$ is $\mu_{\mathrm{max}} = 3.4$. Furthermore, the average friction coefficient can increase by more than an order of magnitude when the patterning angle θ is varied from 20° to 60°.

A simple geometrical model for the measured sliding friction

The significant influence of the angle θ on the friction coefficient can be understood by considering the force balance, illustrated in Figure 6.5. The maximum macroscopic friction coefficient, defined as the ratio of tangential to gravitational force, can be written as

$$\begin{aligned} \mu_{\mathrm{max}} &= \frac{F_{\mathrm{T}}}{F_{\mathrm{G}}} \\ &= \frac{F_{\mathrm{N}} \sin(\theta) + F_{\mathrm{F}} \cos(\theta)}{F_{\mathrm{N}} \cos(\theta) - F_{\mathrm{F}} \sin(\theta)} , \end{aligned} \tag{6.6}$$

where F_{N} and F_{F} are, respectively, the normal and friction force for sliding the patterned top surface uphill. In the uphill direction, the friction force is set by the microscopic friction coefficient μ_0: $F_{\mathrm{F}} = \mu_0 F_{\mathrm{N}}$. The microscopic friction coefficient is measured during flat-on-flat sliding, i.e., $\theta = 0°$, with the same materials under the same conditions and is found to be 0.23 ± 0.02 for the aluminium sliders; see Table 6.2. Alternatively, this flat-on-flat friction coefficient can be derived from the tilt angle θ_0. A flat surface will continuously slide over a tilted bottom surface for a minimum angle θ_0 which results in a definition of the microscopic friction coefficient of

$$\mu_0 = \tan(\theta_0) . \tag{6.7}$$

Note that the tilt angle here is defined for the dynamic sliding condition. For the quantification of the static macroscopic friction coefficient, we expect that the related static tilt angle can be used that is defined based on the — slightly higher — static friction coefficient. Consequently, Equation (6.6) can be rewritten in terms of the microscopic angle θ_0:

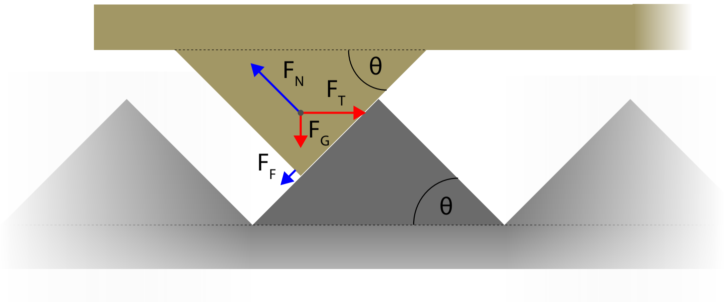

Figure 6.5: Schematic illustration, including a force balance, for sliding two sawtooth patterned surfaces with patterning angle θ over each other. F_G is the gravitational force, F_N the normal force, F_F the friction force and F_T the horizontal pulling force.

$$\mu_{\mathrm{max}} = \tan(\theta + \theta_0)\ . \tag{6.8}$$

Similar to the maximum friction coefficient, the minimum friction coefficient can be derived likewise where the patterning angle is negative:

$$\mu_{\mathrm{min}} = \tan(-\theta + \theta_0)\ . \tag{6.9}$$

Furthermore, the average macroscopic friction coefficient is

$$\mu_{\mathrm{average}} = \frac{\tan(\theta + \theta_0) + \tan(-\theta + \theta_0)}{2}\ . \tag{6.10}$$

In Figure 6.4 the model is shown as the continuous lines and captures the frictional behaviour of sawtooth patterned surfaces. The measured microscopic friction coefficient μ_0 for the aluminium sliders was used to calculate the microscopic angle $\theta_0 = 13°$ [Table 6.2 and Eq. (6.7)]. The blue dashed area in Figure 6.4 represents the zone which is experimentally unreachable; due to the nonzero microscopic angle θ_0 of the surface, the macroscopic friction coefficient reaches infinity at the critical angle $\theta_c = 90 - \theta_0 = 77°$. Above this critical angle, the interlocking of the surfaces results in suppressing the sliding motion.

The friction can therefore be modelled based on the patterning angle θ of the macroscopic periodic surface roughness, and the microscopic sliding friction which can be represented with the microscopic angle θ_0 of the sliders. The latter can be varied by using different slider materials (see Table 6.1) which indeed have various microscopic friction coefficients μ_0 as listed in Table 6.2. These materials, aluminium

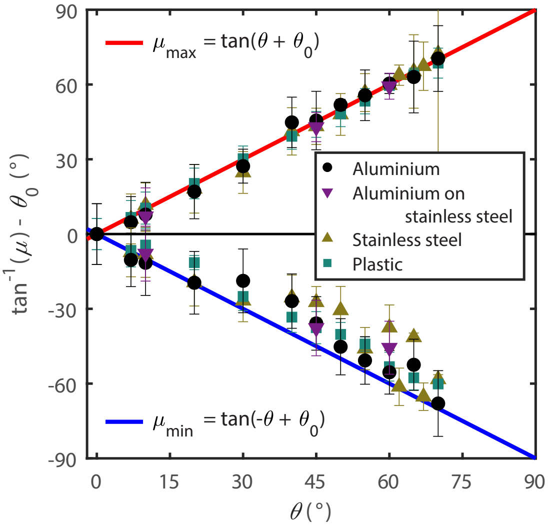

Figure 6.6: The maximum and minimum friction coefficient, normalised with the material-specific angle $\theta_0 = \tan^{-1}(\mu_0)$ where μ_0 is the microscopic friction coefficient, for increasing angle θ. For various materials, aluminium, aluminium on stainless steel, stainless steel, and plastic sliders (more details listed in Table 6.1) the sliding experiments are performed (see Table 6.2 for more details). The red and blue continuous lines represent, respectively, the calculated maximum [Eq. (6.8)] and minimum [Eq. (6.9)] friction coefficient.

stainless steel, and plastic, all exhibit the expected increase in friction as a function of the angles θ_0 and θ. In Figure 6.6, the measured maximum and minimum friction coefficient, normalised with the material-dependent angle θ_0, are given for increasing patterning angle θ. In addition, we plot μ_{max} and μ_{min} (continuous lines) calculated from the model that indeed predicts the measured friction. A systematic deviation between the measurements and the calculation for μ_{min} can be observed; we interpret this deviation as a result of a tilt of the slider when it slides down along the sawtooth pattern. The rod pulling on the slider and attached to the stepper motor is compressed when sliding down because of the negative force. Consequently, the rod will slightly buckle which allows the slider to tilt and thereby decreasing its effective angle θ during sliding down the sawtooth pattern.

Size of the macroscopic periodic roughness

We have shown that the friction can be tuned with a designed periodic roughness and can be modelled based on the angle θ of the roughness and the microscopic friction coefficient μ_0 of the sliding surfaces. The measured, and designed, friction coefficient of the sawtooth patterned surfaces is, however, not entirely independent of the height of the patterns. Decreasing the height of the designed sawtooth‘s from 3 mm down to the μm scale would offer the opportunity to implement the tuning of the friction in various tribological applications; lifting up and down the top surface for 3 mm is for many sliding systems impractical. The potential of (periodic) roughness on the μm scale to improve the often-lubricated tribological performance is already known [152]. Artificial roughness can eliminate the influence of wear debris, controls the contact area or improve a lubricated sliding system [152,155–157]. We therefore quantify the influence of the height of the surface patterns on the sliding friction and find that, unfortunately, the resolution of the fabrication technique limits the ability to tune the friction for small-scale sawtooth patterned surfaces.

The pulling force for an aluminium top surface with a single sawtooth, height of 3 mm and angle θ_T of 45°, is measured when sliding over an aluminium surface with decreasing patterning height; see Figure 6.7. We observe plateaus in the measured pulling force when sliding up and down the patterning for approximately the first

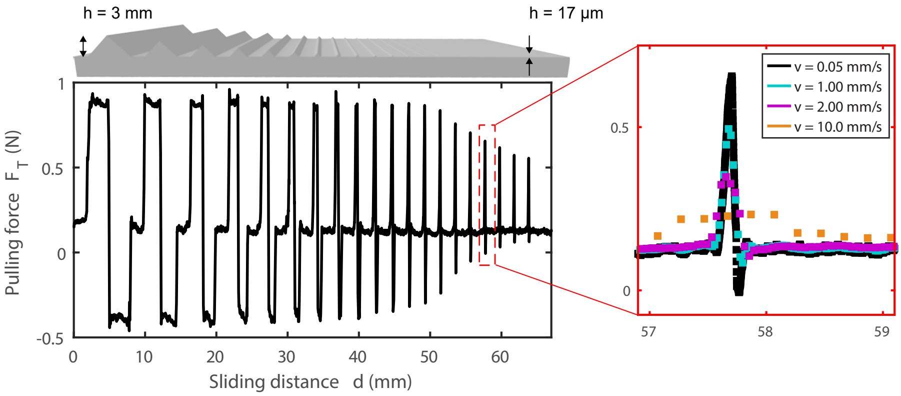

Figure 6.7: Pulling force F_T as a function of the sliding distance d for a sawtooth patterned ($\theta = 45°$) surface fabricated in aluminium with a stepwise decreasing height h. The sliding speed is set at $v = 0.05$ mm/s for an imposed gravitational load of $F_G = 0.72$ N. On the right, the measured pulling force for sliding over a single sawtooth pattern is given for various sliding speed.

8 teeth. However, for the smaller sawtooth‘s with heights down to 17 μm, only peaks in the pulling force are found. To increase the resolution of the monitored friction force, the sliding speed is decreased down to 0.05 mm/s. In Figure 6.7 the effect of speed is shown for sliding over a single sawtooth. As the sampling frequency of the tensile tester is 50 Hz, the sliding distance per datapoint increases from 1 μm/datapoint to 200 μm/datapoint for respectively 0.05 mm/s and 10 mm/s.

We calculate the maximum friction coefficient as a function of the patterning height h, shown as red circles in Figure 6.8(a). The continuous line represents the maximum friction coefficient based on the geometrical model [Eq. (6.8)]. As expected, the sliding friction for a sawtooth pattern with a height of 3 mm is in agreement with the model. However, a significant decrease of the sliding friction is observed when the height of the sawtooth is smaller than 200 μm. This can be explained

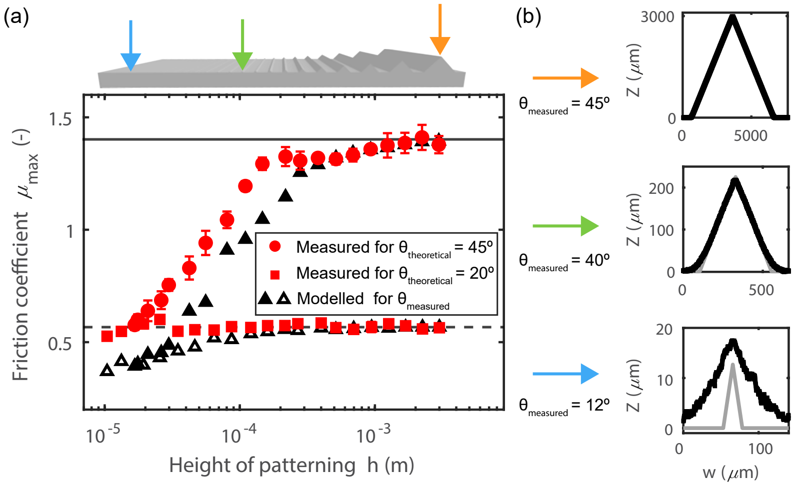

Figure 6.8: (a) Friction coefficient μ for sliding on a sawtooth patterned surface as a function of the pattern height h. The measured maximum friction coefficient is presented as circles and squares for surfaces where patterning angle $\theta_{\text{theoretical}}$ was attempted to hold constant at, respectively, 45° and 20°. The lines show the theoretical friction coefficient μ_{max} [Eq. (6.8)]. As a result of the limited resolution of the fabrication technique, the angle θ decreases significantly for decreasing patterning height. The black triangles are the friction coefficient μ_{max} calculated based on the measured angle θ_{measured}. (b) The line profiles, the height Z as a function of the width, for three sawtooth patterns with decreasing height. The black line represents the measured line profile where the gray line shows the profile that was attempted to be fabricated. The angle θ_{measured} can be quantified based on the slope of the line profiles.

with the limited resolution of the fabrication technique. When an angle $\theta = 45°$ is aimed for, the actual angle is smaller when the patterns are small. We characterise the angles of the manufactured sawtooth patterned surfaces with 3D laser-scanning profilometry (see Section 2.3 for more details) prior to the sliding test. In Figure 6.8(b) the measured height profile Z as a function of the width w is given, shown as black continuous line for three sawtooth patterns with decreasing height. Indeed, for a sawtooth with a height of 3 mm, the angle is 45° as can be calculated based on the slope of the measured height profile. However, the angle decreases to 40° when the height is lowered to 218 μm and gradually decreases further to 12° for a patterning height of 17 μm. Based on the measured angle θ_{measured} for a given height of the sawtooth pattern, the expected maximum friction coefficient μ_{max} can be calculated [Eq. (6.8)] and is given in Figure 6.8 as the black-filled triangles. This is in reasonable agreement with the measured sliding friction and, therefore, explains that when a high angle of 45° can not be achieved for sub-mm patterning, the sliding friction decreases. The influence of the limited fabrication resolution is smaller when a smaller angle θ is designed; the red squares in Figure 6.8 represent the measured maximum friction coefficient for a sawtooth patterned surface with an angle of 20°. Up to a height of 35 μm the patterning can be fabricated with only a small decrease of the angle down to 15°.

Although the decrease of friction for decreasing height of the patterning can be qualitatively explained with the decrease in the fabricated angle θ, full agreement between the measured and calculated friction coefficient is not achieved. We interpret this discrepancy as a result of the surface roughness on the sawtooth pattern; the 3 mm high sawtooth has the expected root-mean-square surface roughness of $S_q = 0.705$ μm (Table 6.1) where, however, the smallest designed sawtooth (a height of 17 μm) has an increased roughness of $S_q = 1.695$ μm (measured for a limited area of 32.7 μm by 208 μm). The increase of surface roughness could explain the underestimation of the friction coefficient of, on average, 0.21 for the model compared with the data of $\theta = 45°$ for patterning heights lower than 200 μm. We therefore suggest that the increased roughness results also in an increased microscopic friction coefficient μ_0 which, in general, for flat-on-flat sliding experiments can be expected; two rough surfaces slide less easy over each other than two smooth ones.

We can therefore decrease the height of the designed periodic surface roughness to tune friction, but the fabrication technique limits the design. We interpret the observed decrease of the maximum friction coefficient for surface patterns below a height of 200 μm as a result of not reaching the high target angle θ. The decrease of friction for decreasing patterning height is partly compensated with the increase in surface roughness. We therefore would expect that with an increase of the fabrication precision the tuning of friction could also be performed for smaller patterns.

6.3.2 (In)commensurability of macroscopic periodic roughness

In reality two surfaces are rarely commensurable, and it is therefore interesting to study the sliding friction of incommensurable surfaces. Perhaps the most interesting observation is that when the sliders are incommensurable, the sliding friction is controlled by the lowest angle θ of the two related surfaces. In Figure 6.9 (in)commensurable sawtooth patterned surfaces are shown; in (a) the friction coefficient is plotted for increasing angle of the top surface θ_T when sliding over a surface with a set angle $\theta_B = 45°$. In the domain $\theta_T < \theta_B$, the measured friction varies with the angle θ_T and agrees with the model [Eqs. (6.8) to (6.10)]. However, for $\theta_T > \theta_B$

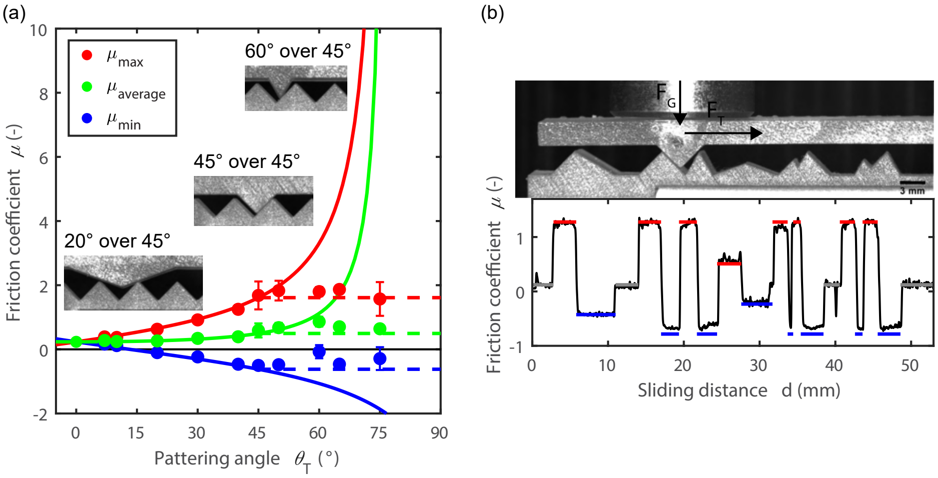

Figure 6.9: (a) Friction coefficient μ as a function of the patterning angle θ_T of the top surface which is pulled over a surface with a constant patterning angle of $\theta_B = 45°$. The maximum, average and minimum friction coefficient are represented in, respectively, red, green, and blue. The observed sliding friction is set by the lowest angle of the top and bottom surface. The continuous lines and dashed lines represents the expected friction based on, respectively, θ_T and θ_B [Eqs. (6.8) to (6.10)]. (b) Friction coefficient μ for sliding on a surface with a quasi-random surface roughness as a function of the sliding distance d. The sliding friction can be predicted based on the lowest angle of the top and bottom surface (continuous lines).

the friction remains constant and is set by the patterning angle of the bottom surface; the horizontal dashed lines represent the expected friction coefficient for a constant angle $\theta_B = 45°$ [Eqs. (6.8) to (6.10)]. This suggests that sliding on a surface with a quasi-randomly macroscopic surface roughness can be understood based on the lowest angle of the two surfaces. As an example, we perform a sliding experiment on a quasi-random patterned surface; see Figure 6.9(b). We slide a top surface with $\theta_T = 45°$ over this designed surface and plot the friction coefficient as a function of the sliding distance d together with the calculated friction coefficient based on the lowest angle of the two surfaces. The model is indeed in agreement with the measured sliding friction coefficient and show that the maximum tuning is limited by the top surface; although sliding over a high angle as $\theta_B = 60°$, the maximum friction is set by the top surface with $\theta_T = 45°$.

Incommensurability therefore restricts the domain of tuning; the friction is set by the lowest angle of the macroscopic roughness of the surfaces. The influence of mismatching surfaces is not restricted to sawtooth patterned surfaces. In Figure 6.10(a) the influence of commensurability is shown for sliding surfaces with a sinusoidal patterned surface. The height Z of the sinusoidal pattern is designed with a controlled wavelength a and a fixed amplitude $b = 1.5$ mm [Eq. (6.1)]. A top surface, which contains 6 periods with a set wavelength ($a_{\text{top}} = 5.44$ mm), is pushed over several bottom surfaces where the wavelengths a_{bottom} is varied. We observe a peak in the friction coefficient when the two surfaces have a commensurable periodicity of surface patterns: $a_{\text{bottom}}/a_{\text{top}} = 1$ and 2. The increase of friction is the result of a matching periodicity of the patterns; when the surfaces fit into each other, the high surface angle θ of the sinusoidal patterning can be reached and increases the sliding friction. The maximum, minimum, and average friction coefficient for commensurable sliding can be calculated based on the simple geometrical model [Eqs. (6.8) to (6.10)] and the angle θ of the sinusoidal patterned surfaces [Eq. 6.3]. The model, represented as the open circles in Figure 6.10, matches the measured sliding friction. Note that the tuning of the friction coefficient is limited when high ratios $a_{\text{bottom}}/a_{\text{top}}$ are set; the maximum angle $\theta_{\max}$ of the sinusoidal surfaces decreases for increasing wavelength a_{bottom}. Tuning with commensurable sinusoidal surfaces is therefore possible, although for higher ratios $a_{\text{bottom}}/a_{\text{top}}$ limited due to the significant decrease of the angle θ. When the two sinusoidal surfaces are incommensurable, we observe a decrease of the sliding friction. When the designed surfaces do not fit into each other, and therefore the surface angles θ in contact are small, the resulting sliding friction is low. The average friction coefficient converges to the lowest limit for these sliding surfaces: the microscopic friction coefficient, i.e., the flat-on-flat

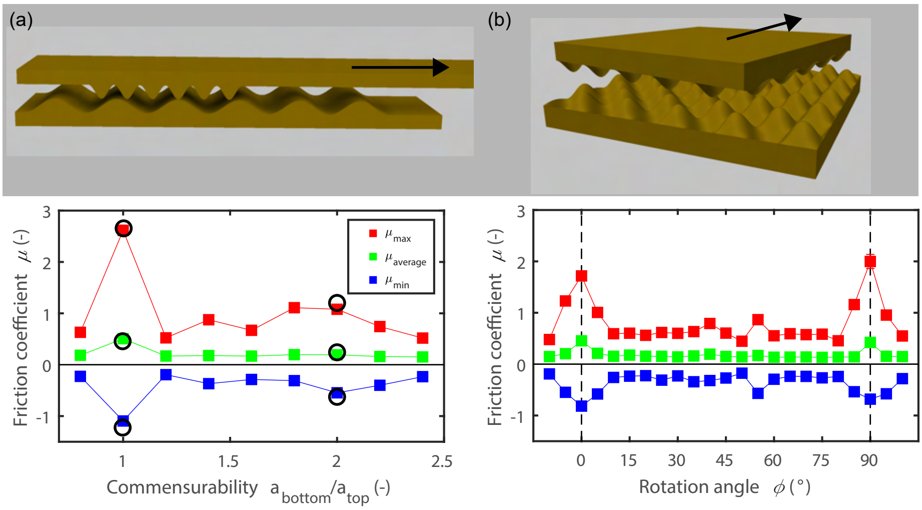

Figure 6.10: Friction coefficient μ for 1D and 2D patterned surfaces as a function of the commensurability. (a) The sliding friction as a function of the ratio of wavelengths of the 1D sinusoidal patterned surfaces. The open circles show the friction coefficient expected for full-commensurable sinusoidal patterned surfaces (at $a_{\text{bottom}}/a_{\text{top}} = 1$ and 2 based on Eq. (6.3). (b) The sliding friction as a function of the rotation angle ϕ between the 2D sinusoidal patterned surfaces.

sliding friction $\mu_0 = 0.12$.

A similar influence of commensurability has been observed in nanotribology and is called structural lubricity: the friction force approaches zero when sliding two atomically incommensurable surfaces over each other [52,158–160]. The structural superlubricity of two graphite surfaces has been shown by Dienwiebel et al. [52]. Graphite has an atomic hill-and-valley landscape in a hexagonal manner which, when rotated, only is commensurable every 60°. The graphite-on-graphite friction reaches ultralow values which, when rotated, shortly increases every 60°. In Figure 6.10(b), we show that structural lubricity is not limited to the microscale; 2D macroscopic surface roughness based on a hill-and-valley landscape [see Eq. (6.4)] permits control on the friction coefficient through the rotation angle ϕ. We perform sliding experiments with the custom-made 2D patterned surfaces and measure the sliding friction as a function of the rotation angle ϕ between the two surfaces. Only when the surfaces are in registry, i.e., at $\phi = 0°$ and every following 90° rotation, a high friction coefficient can be observed. Similarly as to what was observed for the 1D sinusoidal patterned surfaces, the friction coefficient decreases when rotated out of registry.

In general, tuning sliding friction is limited when the designed surfaces are incommensurable. However, with the use of 2D macroscopic surface patterns, the commensurability can be controlled with the rotation of the sliding surface and, subsequently, the sliding friction can be tuned. We continue the exploration of tuning (asymmetric) sliding friction with external parameters with sliding on a Kirigami metamaterial surface. This patterned surface allows us to control the surfaces roughness externally by applying a tensile stress.

6.3.3 Sliding friction on a Kirigami metamaterial

Tuning friction with macroscopic surface topography does also facilitate asymmetric sliding friction; an asymmetry in the surface patterning can result in a different sliding friction based on the sliding direction [161, 162]. With the use of Kirigami metamaterial surfaces, the surface roughness can be controlled externally which results in an asymmetric surface patterning and, consequently, an asymmetric sliding friction [163, 164]. Kirigami is a Japanese artform of paper cutting where, with repetitive patterns, highly stretchable and 3D objects can be achieved from a flat sheet [165–167]. With a well-designed patterning of cuts, out-of-plane texturing can be formed for increasing in-plane uniaxial strain. Rafsanjani et al. made use of this technique to tune on-demand the texturing of a Kirigami metamaterial sheet [154]. The authors designed a bioinspired 'snake' that, due to repeated stretching and releasing of the Kirigami skin, can crawl forward; this is indeed very similar to the scaled skin of snakes which enable them to propel themselves [168, 169]. This metamaterial crawler was fabricated by attaching a Kirigami-pattered sheet to the surface of a soft cylindrical actuator that extends axially upon inflation. When inflated, the Kirigami skin, due to the increase of strain, forms an out-of-plane texturing. The formed texture interlocks at the rough substrate where it is placed on and, with cycled inflation, the crawler performs locomotion. The formation of on-demand texturing, based on Kirigami 'scales' point out-of-plane, is very similar to the sawtooth patterns. Therefore, in addition to interlocking due to the formation of anchoring points, the Kirigami metamaterial surface does allow tuning the friction by externally controlling its roughness.

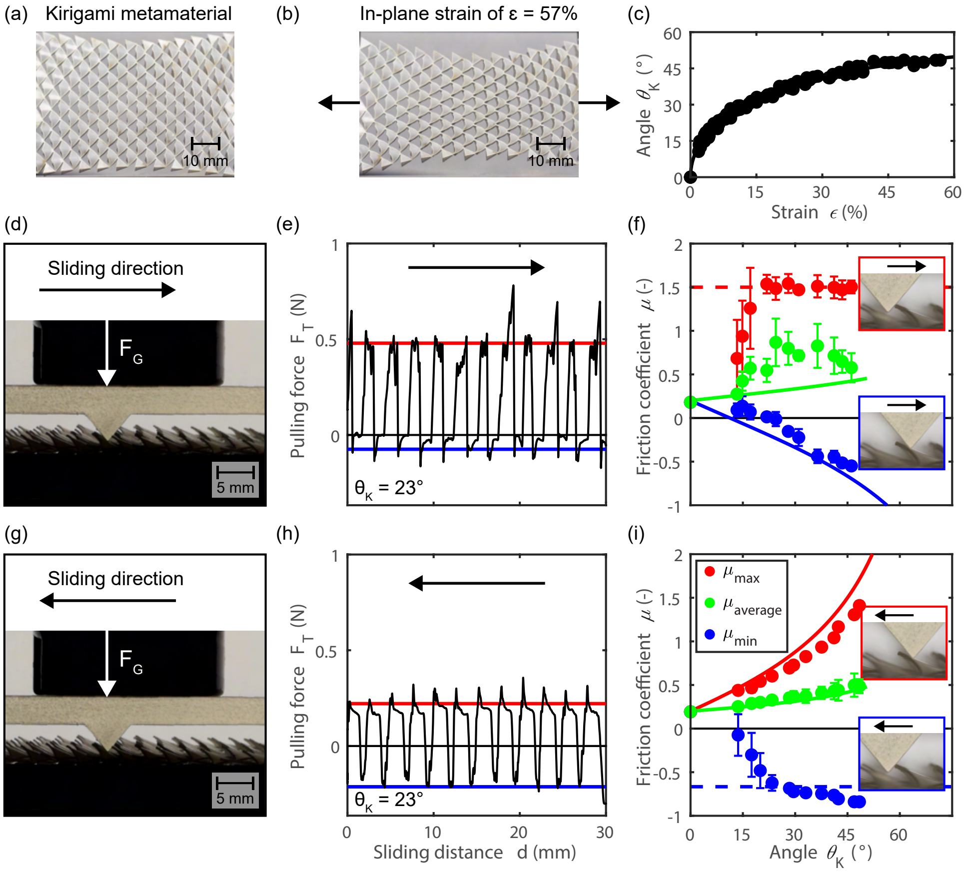

Figure 6.11: Sliding experiments on a Kirigami metamaterial. (a) A Kirigami patterning is laser-cut in a Mylar sheet. (b) A macroscopic out-of-plane surface roughness, i.e., scales pointing outwards, can be actuated for increasing in-plane uniaxial strain ϵ. (c) Kirigami angle θ_K for increasing strain ϵ. The black continuous line is a fit, see Appendix B.1 for more details. (d) Side-view of the sliding experiment when sliding against the formed Kirigami scales. The slider has a single sawtooth pattern with an angle of $\theta_T = 45°$. (e) Pulling force F_T as a function of the sliding distance d when the slider is pulled against the Kirigami scales pointing upward with an angle of $\theta_K = 23°$. In continuous red and blue lines, the calculated friction coefficient for, respectively, the maximum [Eq. (6.8)] and minimum [Eq. (6.8)]. (f) Friction coefficient μ as a function of the measured Kirigami angle θ_K for sliding against the scales. In continuous lines the calculated friction coefficients are shown [Eqs. (6.8), (6.9), and (B.2)]. (g-i) The sliding experiment when performed along the Kirigami scales.

To demonstrate the capability of Kirigami metamaterials to tune the friction, we laser cut a Mylar sheet with a triangular pattern (see Section 6.2 for more experimental details) and perform sliding experiments while controlling the in-plane uniaxial strain ϵ. In Figure 6.11(a) and (b) we visualise from top the response of the Kirigami metamaterial for increasing strain. The scales point upwards with an angle θ_K that can be quantified visually from the side; see Figure 6.11(c). We perform sliding experiments with a single sawtooth ($\theta_T = 45°$) patterned plastic surface pulled horizontally against and along the Kirigami scales as visualised in, respectively, Figure 6.11(d) and (g). The pulling force F_T for sliding on the Kirigami surface, at a controlled angle of $\theta_K = 23°$, as a function of the sliding distance is given in Figure 6.11(e) and (h) for, respectively, sliding against and along the scales. The measured pulling forces indeed roughly have a square wave shape, similarly as was found for the sawtooth patterned surfaces. The square wave is disturbed by periodic peaks in the pulling force, located when the slider reaches the top of the Kirigami scales. The end of the Kirigami scale acts as an anchoring point, i.e., it grips the top surface. Only when the pulling force has been sufficiently increased, the slider jumps over the scale and the interlocking is released. With the remaining plateaus in the square wave, that can again be quantified with F_{max} and F_{min}, the upward and downward macroscopic friction coefficient can be calculated for the set gravitational force F_G.

In Figure 6.11(f) and (i), the maximum, minimum, and average friction coefficient is given as a function of θ_K when sliding against and along the Kirigami scales. Similar as for the sawtooth patterned sliders, the maximum and minimum friction coefficient can be modelled with Equations (6.8) and (6.9), shown as the red and blue continuous lines. Again, the smallest angle θ, that is either the Kirigami scale angle θ_K or the angle of the top surface θ_T, sets the friction coefficient. The measured maximum and minimum friction coefficient is, therefore, very anisotropic: it depends on the sliding direction and shows strongly asymmetric friction.

In addition, the measured average friction coefficient [shown as the green circles in Fig. 6.11(f)] is very high and seems to be rather θ_K-independent when sliding against the pattern. It increases smoothly with θ_K when sliding with the pattern, shown as the green circles in Figure 6.11(i). The high and rather constant value of the friction when sliding against the pattern is likely due to sticking of the material on the top. This asymmetry of the Kirigami metamaterial decreases with increasing strain and can be geometrically calculated, as discussed in Appendix B.1. The green lines in Figure 6.11(f) and (i) are the weighted average friction coefficient based on the asymmetric path lengths [respectively Eqs. (B.2) and (B.3)].

Kirigami metamaterial surfaces, or even metamaterials in general [170], allows us to control the sliding friction externally based on the formation of 3D texturing. Next to the asymmetric friction based on interlocking, a Kirigami metamaterial does also facilitate sliding friction with an on-demand tunable friction coefficient.

6.4 Discussion and conclusion

We have presented sliding experiments of sliders with various macroscopic surface patterning and shown the influence of the patterning slope and the commensurability of the surfaces. A simple geometrical model describes the measured sliding friction based on the macroscopic geometry together with the microscopic friction coefficient μ_0. The influence of macroscopic geometrical patterns on friction can be applied to various tribological systems; earthquake dynamics [143] and anisotropic friction by surface patterns [171, 172] have been modelled based on their macroscopic surface geometry. A similar model has been introduced to describe the microscopic friction coefficient based on the surface height variations of surfaces [173, 174]. However, modelling the influence of the surface roughness with this geometrical model was not satisfactory; the real contact area that is formed and the shear stress prior to sliding on the asperity-level is rather more complex [114]. In the model presented here, we separate the rather complex (adhesive) friction coefficient μ_0 from the geometrical part for macroscopic surface roughness.

In summary, with artificial macroscopic surface roughness the sliding friction can be tuned by more than an order of magnitude which can be explained using a simple geometrical model that takes into account the interlocking between the two surfaces. The slope, quantified with the angle, of the surface patterning and the commensurability of patterned surfaces enables direct control on the sliding friction. In addition, a Kirigami metamaterial surface allows to apply this understanding of geometrical friction to enable external and on-demand control of the friction force.

Appendices

APPENDIX A

Sliding friction on ice

A.1 The penetration hardness of ice

The penetration hardness P_h is quantified with an indentation experiment where a sphere with a radius of $R = 1.6$ mm is pushed into the ice surface, see Section 2.2 for more details. For an indentation velocity v_ind of 3.8 μm/s the indentation depth δ as a function of the loading force N is plotted in Figure A.1 for several temperatures.

The measured penetration hardness, see Figure 5.2, is fitted with a polynomial regression on the variables temperature T (in °C) and the logarithm of the indentation speed $\ln(v_\mathrm{ind})$ with, respectively, 1 and 3 degrees:

$$\begin{aligned} P_\mathrm{h}(T, v_\mathrm{ind}) = {} & P_{00} + P_{10}T + P_{01}\ln(v_\mathrm{ind}) \\ & + P_{11}\, T \ln(v_\mathrm{ind}) + P_{02}\ln(v_\mathrm{ind})^2 \\ & + P_{12}\, T\ln(v_\mathrm{ind})^2 + P_{03}\ln(v_\mathrm{ind})^3 \,. \end{aligned} \tag{A.1}$$

The fit parameters found, with a resulting coefficient of determination of $R^2 = 0.8885$, are $P_{00} = 8.041 \times 10^8$, $P_{10} = -3.337 \times 10^6$, $P_{01} = 1.465 \times 10^8$, $P_{11} = -2.645 \times 10^5$, $P_{02} = 8.936 \times 10^6$, $P_{12} = -6.282 \times 10^3$, and $P_{03} = 1.792 \times 10^5$. For a constant indentation speed of $v_\mathrm{ind} = 3.8$ μm/s, as used in Figures 5.2 and A.1, this fit results in a penetration hardness that linearly decreases with temperature as $P_\mathrm{h} = (-1.01\, T + 19.2) \times 10^6$.

Close to the melting point, pressure melting occurs; the melting temperature of ice decreases with increasing pressure because the liquid-phase density is lower than the solid phase. The pressure that has to be exceeded to melt ice is described by the Clausius-Clapeyron equation [175]:

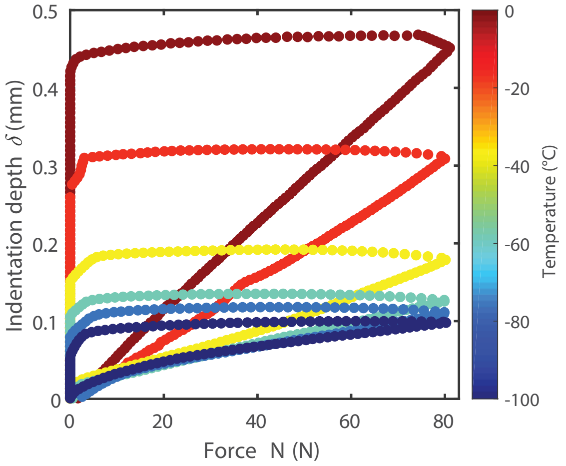

Figure A.1: Indentation depth δ as a function of the force N for an indentation speed of 3.8 μm/s captured with a hardness test for various temperatures.

$$P_\mathrm{m} = \frac{L}{T_0 \Delta V} T = -13.5 \times 10^6 \; T \, , \tag{A.2}$$

with $L = 3.34 \times 10^5$ J/kg the latent heat of fusion, $T_0 = 0$ °C the freezing point of water at a pressure of 1 bar, and $\Delta V = -9.05 \times 10^{-5}$ m^3/kg the change in specific volume from solid to liquid. For temperatures higher than -1.5 °C, the pressure necessary for pressure melting is lower than the penetration hardness. Therefore, the limiting pressure for -1.5 °C up to 0 °C in Figure 5.2 is described by the Clausius-Clapeyron equation.

A.2 Ploughing model

A spherical slider ploughing through ice, similar as ploughing through granular materials as described in Chapter 3, occurs when the contact pressure exceed the penetration hardness. In this plastic regime, the sphere indents into ice up to the contact area A_c can support the normal force: $A_\mathrm{c} = \frac{N}{P_\mathrm{h}(T)}$. This contact area, the projected area of contact in the normal direction, which is in contact with the ice surface, is $A_\mathrm{c} = \frac{1}{2}\pi r^2$, with r the radius of the ploughing track. The final depth of indentation δ can be written, with the use of $\delta \approx \frac{r^2}{2R}$ for $\delta << R$, as $\delta = \frac{N}{\pi R P_\mathrm{h}(T)}$. Consequently, this indentation results in scratching ice with a ploughing area A_P and a ploughing force $F_\mathrm{P} = A_\mathrm{P} P_\mathrm{h}(T)$. The ploughing area is the cross-sectional area $A_\mathrm{P} \approx \frac{4}{3} r\delta$, and it can be rewritten as

$$A_\mathrm{P} = \frac{4\sqrt{2}}{3\pi^{3/2}R} \frac{N^{3/2}}{P_\mathrm{h}(T)^{3/2}} , \tag{A.3}$$

which results in a ploughing force of

$$F_\mathrm{P} = A_\mathrm{P} P_\mathrm{h}(T) = \frac{4\sqrt{2}}{3\pi^{3/2}R} \frac{N^{3/2}}{\sqrt{P_\mathrm{h}(T)}} . \tag{A.4}$$

With $\mu_\mathrm{P} = F_\mathrm{P}/N$, we get Equation (5.2).

Velocity-dependent ploughing model

To take into account the velocity dependency of the penetration hardness, as is shown in the inset of Figure 5.2(a) and fitted with Equation (A.1), the ploughing model has to be modified. Two velocities, and therefore two penetration hardnesses, are involved in ploughing: the indentation speed v_ind in the normal direction, where the ice is indented by the slider; and the sliding speed v_s in the tangential direction, the speed at which the final ploughing occurs. As the ploughing area A_P is set by the indentation in the normal direction, the corresponding penetration hardness is at the indentation speed:

$$A_\mathrm{P} = \frac{4\sqrt{2}}{3\pi^{3/2}R} \frac{N^{3/2}}{P_\mathrm{h}(T, v_\mathrm{ind})^{3/2}} . \tag{A.5}$$

The subsequent ploughing force is then based on the penetration hardness at the sliding speed and the calculated ploughing area A_P:

$$F_\mathrm{P} = \frac{4\sqrt{2}}{3\pi^{3/2}R} \frac{P_\mathrm{h}(T, v_\mathrm{s})}{P_\mathrm{h}(T, v_\mathrm{ind})^{3/2}} N^{3/2} . \tag{A.6}$$

Based on the sphere-on-ice geometry, we can calculate the indentation speed corresponding to the sliding speed and subsequently calculate the related penetration hardness for the ploughing force. The ratio of the related speeds is:

$$\frac{v_\mathrm{ind}}{v_\mathrm{s}} = \frac{\delta}{r} = \sqrt{\frac{N}{2\pi R^2 P_\mathrm{h}(T, v_\mathrm{ind})}} . \tag{A.7}$$

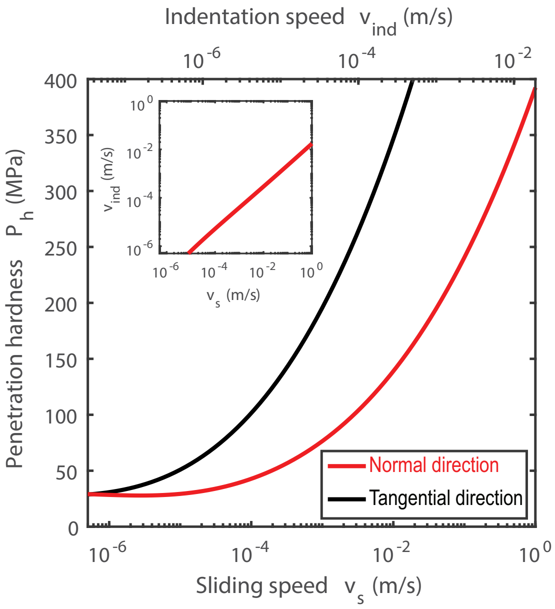

Figure A.2: Penetration hardness in the normal direction (red) and tangential direction (black) as a function of sliding speed for ice at a temperature of −20 °C based on Eq. (A.1). The calculated indentation speed corresponding to the set sliding speed is given in the inset and as top axes for sliding a glass sphere ($R = 1.84$ mm) at a normal force of 2.5 N over ice at −20 °C, Eq. (A.7). The indentation speed is around 4% of the sliding speed, and consequently, the penetration hardness in the normal direction is smaller than the penetration hardness in the tangential direction.

This nonlinear equation can be numerically solved to yield an indentation speed v_{ind} for a given sliding speed v_{s}. For a glass sphere sliding over ice at −20 °C, the resulting indentation speed as a function of the sliding speed is given in the inset of Figure A.2; the indentation speed is, in general, a fraction of the sliding speed, around 4%. Consequently, for a given sliding speed, we can calculate the penetration hardness in the normal and tangential directions; see Figure A.2. Finally, the friction force and friction coefficient can be calculated based on Equation (A.6), where the indentation speed is based on numerically solving Equation (A.7).

A.3 Contact mechanics

Soda-lime glass

To quantify the real contact area (RCA) and the average contact pressure P_c of the spherical sliders on ice, we use the Tribology Simulator (from Tribonet [62]). Based on the surface topography of the slider and the mechanical properties of the slider and the ice surface, the simulator solves the elastoplastic contact equations through a numerical boundary element model. The plastic limit is set by the penetration hardness of the ice in the normal direction, calculated for the set sliding speed $v_s = 0.38$ mm/s and temperature T, with the use of Equations (A.1) and (A.7).

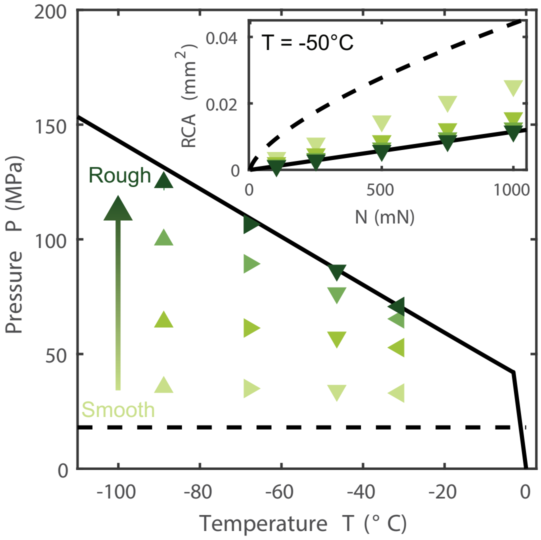

Figure A.3: Pressure P as function of the temperature T for glass spheres with surface roughnesses 98, 222, 575, and 3077 nm at a normal force of 500 mN. The smoothest sphere is mainly elastic where, for increasing surface roughnesses, the pressure increases until the plastic limit is reached. The dashed and solid lines are, respectively, the elastic Hertzian pressure and the penetration hardness P_h of the ice. For the latter, the penetration hardness in the normal direction for the set sliding speed of 0.38 mm/s is used. Inset: RCA as a function of the normal force N. Indenpendent of the surface roughness, the real contact area increases linearly with the normal force. Therefore, the contact pressure is almost independent of the normal force.

In Figure A.3, the contact pressure as a function of temperature is given for glass spheres with surface roughness S_q from 98 nm to 3077 nm. The dashed and solid lines represent, respectively, the elastic Hertzian contact pressure [176] and the plastic limit given by the penetration hardness as N/P_h. For increasing surface roughnesses, the contact mechanics convert from a mainly elastic contact to a plastic contact. The RCA increases linearly, even for the relatively smooth sphere, with the normal force, as is given in the inset of Figure A.3. Therefore, the contact pressure is almost independent of the normal force.

Silicon carbide

In Figure A.4, the real contact area for the SiC spheres is given as a function of the normal force. Both spheres, with radii of 6.00 (red) and 0.75 mm (blue), have a mainly elastic contact with the ice surface at −50 °C (open circles) and at −90 °C (closed circles). The large sphere has a large RCA and, due to the finite size of the measured surface topography (208 by 208 μm), can only be calculated up to 400 mN.

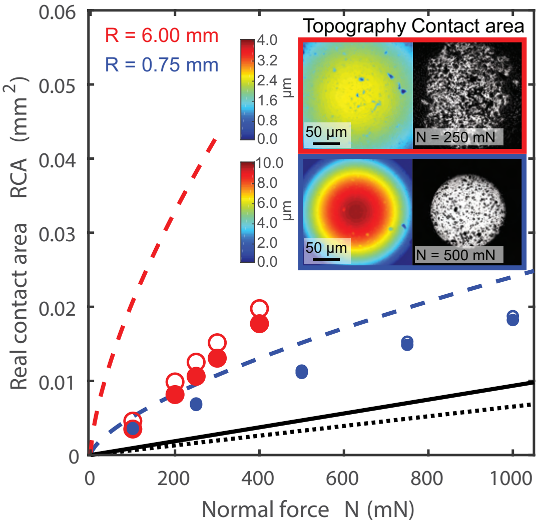

Figure A.4: Contact mechanics of the SiC spheres sliding on ice and RCA as a function of normal force N for a sphere with a radius of 6.00 mm (red) and 0.75 mm (blue) at temperatures of −50 °C (open circles) and −90 °C (closed circles). The dashed lines represent the elastic Hertzian pressure. The solid and dotted lines are, respectively, the plastic limit set by the penetration hardness at temperatures of −50 °C and −90 °C. Inset: surface topography (left) and calculated area of real contact (right) for the SiC spheres.

Sapphire

The contact mechanics for a sapphire sphere on ice are given in Figure A.5. The contact is mainly elastic due to the low surface roughness (28 nm). Therefore, the RCA increases, as expected for an elastic Hertzian contact [176], sublinearly with the normal force. The RCA for a normal force of 500 mN is used to quantify the shear stress and contact pressure.

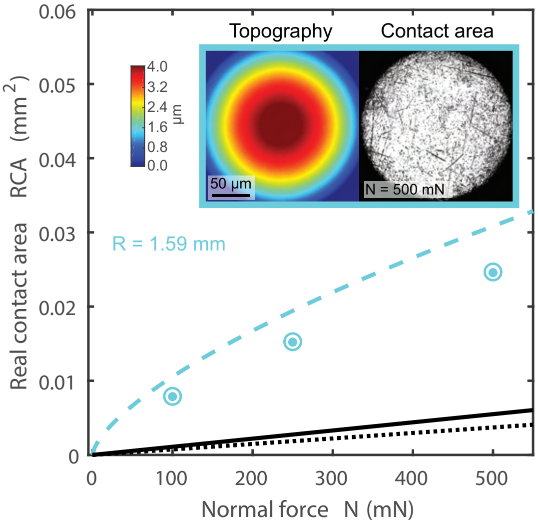

Figure A.5: Contact mechanics of a sapphire sphere (radius of 1.59 mm) sliding on ice and RCA as a function of the normal force N at temperatures of -50 °C (open circles) and -90 °C (closed circles). The dashed line represents the elastic Hertzian pressure and the solid and dotted lines are, respectively, the plastic limit set by the penetration hardness at temperatures of -50 °C and -90 °C. Inset: surface topography (left) and calculated area of real contact (right) for the sapphire sphere.

A.4 Ploughing on the microroughness scale

Ploughing not only occurs on the macroscale of the slider-on-ice contact; single asperities can plastically deform the ice and therefore plough through it tangentially. In Figure 5.3(b), the ploughing tracks that were left on the ice after a sphere slid over the ice surface are given. For a high surface roughness, $S_q = 3077$ nm, the measured ploughing area ($A_P = 7.8 \times 10^{-11}\ m^2$) results in a friction coefficient based on ploughing of $\mu_P = 0.07$ [for $N = 0.21$ N, penetration hardness in the normal direction $P_h = 194$ MPa and using Equation (5.2)]. As the increase in the friction coefficient for the highest surface roughness relative to the lowest surface roughness is $\Delta\mu = 0.24$, the ploughing can only explain 30% of the increased friction. Based on the measured surface topography, a ploughing area of ($A_P = 12.2 \times 10^{-11}\ m^2$)

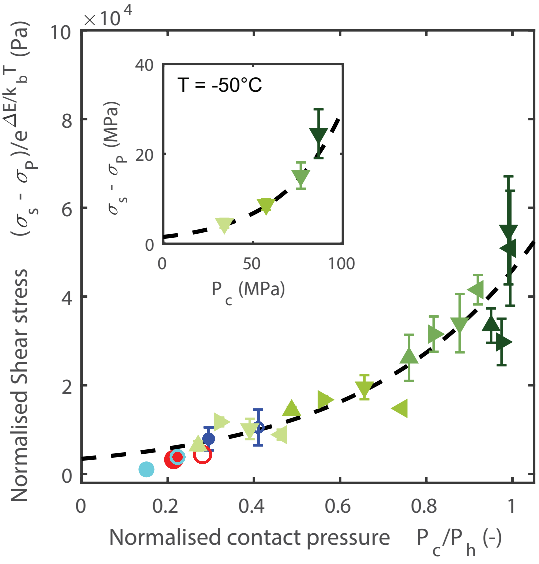

Figure A.6: Normalised effective shear stress $(\sigma_s - \sigma_P)/e^{\Delta E/k_B T}$ as a function of the normalised contact pressure P_c/P_h for various sliders, surface roughnesses, and temperatures at a sliding speed of 0.38 mm/s. Here, the effective shear stress is based on the measured friction force, excluding the ploughing contribution. The ploughing can explain up to 40% of the observed increased friction. The dashed line is a fit using Eq. (5.4). The same symbols and colours are used as in Fig. 5.4. Inset: effective shear stress $\sigma_s - \sigma_P$ as a function of the contact pressure P_c for various glass sliders with increasing surface roughness at $T = -50$ °C and a sliding speed of 0.38 mm/s.

can be calculated [see gray area in the top panel of Fig. 5.3(b)]. As the orientation of the sphere on ice is not the same, a small difference is found compared with the measurements in both the ploughing track and the ploughing area. Now, the ploughing can explain 40% of the observed increased friction.

In Figure A.6, the increase of shear stress with increasing contact pressure where the ploughing is excluded is given. For the ploughing stress $\sigma_P = F_P/\mathrm{RCA}$, a ploughing force based on the quantified plastic indentation of the surface topography is used. We can model the effective shear stress $\sigma_s - \sigma_P$ as Equation (5.4) with $\sigma_0 = 3.4$ kPa and $b = 2.6$. Consequently, if ploughing is taken into account, the shear stress set by the mobility of the ice surface is, although smaller, still the main contribution to the friction force.

APPENDIX B

Sliding friction of geometrically controlled surfaces

B.1 Geometrical friction model for Kirigami metamaterial surfaces

For the sliding experiments on a Kirigami metamaterial surface, we slid a single sawtooth-patterned ($\theta_\mathrm{T} = 45°$) plastic surface horizontally against and along the Kirigami scales. Consequently, the slider moved up and down over the Kirigami patterned surface. The resulting Kirigami texturing was asymmetric; as such, the horizontal sliding lengths for moving up and down the scales were not equal. In order to calculate the average macroscopic friction coefficient based on the simple geometrical model, a weighted average friction coefficient had to be quantified for the specific geometry.

In Figure B.1, a schematic representation of the sliding experiment is given from a side view. The formed scales of length l_0 (thick black and red lines) point out of the plane with an angle θ_K, which is set by the strain ϵ. In Figure 6.11(c) the angle θ_K is quantified for increasing uniaxial strain and fitted with the use of

$$\theta_\mathrm{K} = p_1\sqrt{\epsilon} + b\epsilon + c \, , \tag{B.1}$$

with $p_1 = 102.40$, $p_2 = -48.89$, and $p_3 = -0.21$ and θ_K in degrees. The Kirigami patterned sheet has, as seen from the side, two overlapping rows of Kirigami scales, which are represented as black and red triangles in Figure B.1. The top surface made the transition between sliding up and down when it was in contact with both overlaying rows (the black and red scales as presented in Fig. B.1). Consequently,

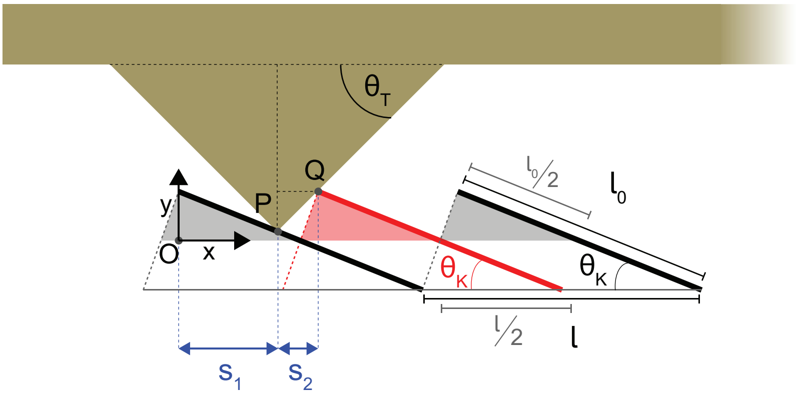

Figure B.1: Schematic illustration of the performed sliding experiments on a Kirigami metamaterial, illustrated from the side. A slider with a sawtooth-patterned surface with angle of θ_T was pulled horizontally over the scales of the Kirigami patterned surface. Consecutive lines of scales were formed which halfway overlapped in depth; see the thick black and red lines.

the sliding lengths s_1 and s_2 for sliding up and down can be defined. The weighted average friction coefficient for sliding against and along the Kirigami patterned surface can be defined as

$$\mu_{\text{against}} = \frac{s_2}{s_1+s_2}\tan\left(\theta_T+\theta_0\right) + \frac{s_1}{s_1+s_2}\tan\left(-\theta_K+\theta_0\right) \tag{B.2}$$

$$\mu_{\text{along}} = \frac{s_1}{s_1+s_2}\tan\left(\theta_K+\theta_0\right) + \frac{s_2}{s_1+s_2}\tan\left(-\theta_T+\theta_0\right)\,. \tag{B.3}$$

To calculate the weighted average friction coefficient, we expressed the sliding lengths s_1 and s_2 in terms of the quantified strain ϵ and angles θ_K and θ_T. The overlap between the Kirigami patterning is half of the triangle base length l. Therefore, sliding only occurred on the top part of the pattern, as shown by the red- and grey-filled triangles in Figure B.1. These top triangles have side lengths of $l/2$ and $l_0/2$ and the same interior angle of θ_K. Consequently, the sliding paths s_1 and s_2 can be written as

$$s_1 + s_2 = l/2\,, \tag{B.4}$$

which can also be defined in terms of ϵ and l_0 with $l = (1+\epsilon)l_0$ as

$$s_1 + s_2 = (1+\epsilon)l_0/2\,. \tag{B.5}$$

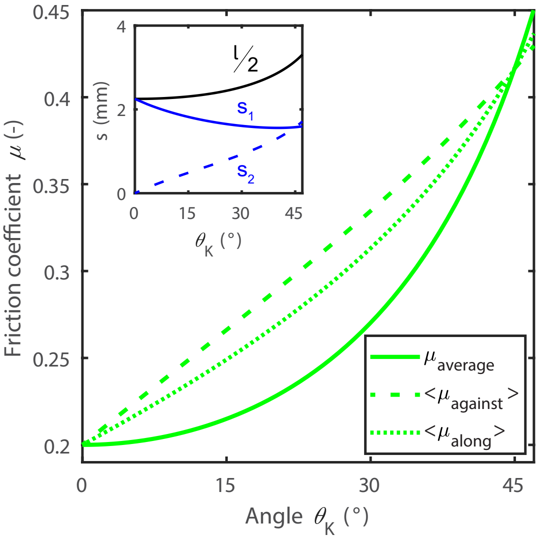

Figure B.2: The average friction coefficient as a function of the Kirigami patterning angle θ_K. The two dashed lines represent the weighted average friction coefficient for sliding a sawtooth patterned top surface with an angle of θ_T of 45° horizontally against or along the formed scales of the Kirigami metamaterial. The Kirigami angle θ_K is calculated with Eq. (B.1) for a given strain ϵ, and the weighted average friction coefficient is subsequently plotted based on Eqs. (B.2) and (B.3). As a reference, the average friction coefficient for a symmetric sliding path, i.e. for $s_1 = s_2$, is included as the continuous line. Inset: the sliding lengths s_1 and s_2 as a function of the Kirigami angle θ_K. In addition, the total length $l/2 = s_1 + s_2$ is included.

The transition for the top surface between sliding up and down the Kirigami patterns can be defined in the condition $\theta_\mathrm{K} < \theta_\mathrm{T}$ when both tips of the surface patterns are in contact with the opposite surface. The tangent points are defined as *P* and *Q* (see Fig. B.1). With the use of the origin *O*, the (x,y) coordinates for both points can be written as

$$\begin{pmatrix} x_\mathrm{P} \\ y_\mathrm{P} \end{pmatrix} = \begin{pmatrix} s_1 \\ l_0 \sin(\theta_\mathrm{K})/2 - s_1 \tan(\theta_\mathrm{K}) \end{pmatrix} \tag{B.6}$$

$$\begin{pmatrix} x_\mathrm{Q} \\ y_\mathrm{Q} \end{pmatrix} = \begin{pmatrix} s_1 + s_2 \\ l_0 \sin(\theta_\mathrm{K})/2 \end{pmatrix} \tag{B.7}$$

In addition, the points P and Q can be related to the geometry of the slider as

$$\tan(\theta_{\mathrm{T}}) = \frac{y_{\mathrm{Q}} - y_{\mathrm{P}}}{x_{\mathrm{Q}} - x_{\mathrm{P}}} \, . \tag{B.8}$$

Therefore, with the use of Equations (B.5) through (B.8), the lengths s_1 and s_2 can be written as

$$s_1 = \frac{(1+\epsilon)l_0}{2[1+\tan(\theta_{\mathrm{K}})/\tan(\theta_{\mathrm{T}})]} \tag{B.9}$$

$$s_2 = \frac{(1+\epsilon)l_0}{2[1+\tan(\theta_{\mathrm{T}})/\tan(\theta_{\mathrm{K}})]} \, . \tag{B.10}$$

In the inset of Figure B.2, the sliding lengths as a function of the angle θ_{K} are given. Here, s_1, s_2 and the total length $l/2 = s_1 + s_2$ are plotted, where the increasing strain ϵ is transferred to the found angle θ_{K} with Equation (B.1). Using the calculated sliding lengths s_1 and s_2, the weighted average friction coefficient for sliding against and along the Kirigami surface can be derived (see Fig. B.2). As a reference, the average friction coefficient for a symmetric sliding path ($s_1 = s_2$) is included as the continuous line. Due to the sharp scale when sliding against, and the long upward path s_1 when sliding along the Kirigami surfaces, the average friction coefficients for Kirigami are higher than for a symmetric commensurable case.

References

[1] K. Holmberg and A. Erdemir, “Influence of tribology on global energy consumption, costs and emissions,” *Friction*, vol. 5, no. 3, pp. 263–284, 2017.

[2] H. P. Jost, *Lubrication: Tribology; Education and Research; Report on the Present Position and Industry's Needs (submitted to the Department of Education and Science by the Lubrication Engineering and Research) Working Group*. HM Stationery Office, 1966.

[3] A. H. Layard, “Discoveries in the ruins of nineveh and babylon, with travels in armenia,” *Kurdistan and the desert, London*, 1853.

[4] P. E. Newberry, *El Bersheh: The tomb of Tehuti-Hetep*, vol. 1. Egypt Exploration Fund, 1895.

[5] R. F. Heizer, “Ancient heavy transport, methods and achievements,” *Science*, vol. 153, no. 3738, pp. 821–830, 1966.

[6] A. Fall, B. Weber, M. Pakpour, N. Lenoir, N. Shahidzadeh, J. Fiscina, C. Wagner, and D. Bonn, “Sliding friction on wet and dry sand,” *Physical Review letters*, vol. 112, no. 17, p. 175502, 2014.

[7] C. S. C. Davison, “Transporting sixty-ton statues in early assyria and egypt,” *Technology and Culture*, pp. 11–16, 1961.

[8] A. B. Lloyd, *A companion to ancient Egypt*, vol. 52. John Wiley & Sons, 2010.

[9] S. Ayrinhac, “The transportation of the djehutihotep statue revisited,” *Tribology Online*, vol. 11, no. 3, pp. 466–473, 2016.

[10] J. Li and H. Chen, “Lubrication for transporting heavy objects in the history,” *Tribology Online*, vol. 11, no. 2, pp. 242–248, 2016.

[11] J. Li, H. Chen, and H. A. Stone, “Ice lubrication for moving heavy stones to the forbidden city in 15th-and 16th-century china,” *Proceedings of the National Academy of Sciences*, vol. 110, no. 50, pp. 20023–20027, 2013.

[12] D. Dowson, *History of tribology*. Addison-Wesley Longman Limited, 1978.

[13] `https://www.leonardodigitale.com`. Accessed: 2021-01-21.

[14] I. M. Hutchings, "Leonardo da vinci's studies of friction," *Wear*, vol. 360, pp. 51–66, 2016.

[15] E. Popova and V. L. Popov, "The research works of coulomb and amontons and generalized laws of friction," *Friction*, vol. 3, no. 2, pp. 183–190, 2015.

[16] A. A. Pitenis, D. Dowson, and W. G. Sawyer, "Leonardo da vinci's friction experiments: An old story acknowledged and repeated," *Tribology Letters*, vol. 56, no. 3, pp. 509–515, 2014.

[17] C. Pedretti *et al.*, *The Codex Atlanticus of Leonardo da Vinci*. Johnson, 1978.

[18] F. P. Bowden and D. Tabor, "The area of contact between stationary and moving surfaces," *Proceedings of the Royal Society of London. Series A. Mathematical and Physical Sciences*, vol. 169, no. 938, pp. 391–413, 1939.

[19] F. P. Bowden and D. Tabor, *Friction: an introduction to tribology*. Anchor, 1973.

[20] B. Armstrong-Hélouvry, *Friction in Machines*, pp. 7–42. Boston: Springer, 1991.

[21] H. Hertz, "Über die berührung fester elastischer körper," *Journal für die reine und angewandte Mathematik*, vol. 1882, no. 92, pp. 156 – 171, 1882.

[22] K. L. Johnson, *Contact Mechanics*. Cambridge University Press, 1985.

[23] J. A. Greenwood and J. B. P. Williamson, "Contact of nominally flat surfaces," *Proceedings of the royal society of London. Series A. Mathematical and physical sciences*, vol. 295, no. 1442, pp. 300–319, 1966.

[24] J. A. Greenwood and J. J. Wu, "Surface roughness and contact: an apology," *Meccanica*, vol. 36, no. 6, pp. 617–630, 2001.

[25] T. D. B. Jacobs, T. Junge, and L. Pastewka, "Quantitative characterization of surface topography using spectral analysis," *Surface Topography: Metrology and Properties*, vol. 5, no. 1, p. 013001, 2017.

[26] J. Gao, W. D. Luedtke, D. Gourdon, M. Ruths, J. N. Israelachvili, and U. Landman, "Frictional forces and amontons' law: from the molecular to the macroscopic scale," 2004.

[27] J. F. Archard, “Elastic deformation and the laws of friction,” *Proceedings of the Royal Society of London. Series A. Mathematical and Physical Sciences*, vol. 243, no. 1233, pp. 190–205, 1957.

[28] K. L. Johnson, K. Kendall, and A. D. Roberts, “Surface energy and the contact of elastic solids,” *Proceedings of the royal society of London. A. mathematical and physical sciences*, vol. 324, no. 1558, pp. 301–313, 1971.

[29] A. W. Bush, R. D. Gibson, and T. R. Thomas, “The elastic contact of a rough surface,” *Wear*, vol. 35, no. 1, pp. 87–111, 1975.

[30] B. V. Derjaguin, V. M. Muller, and Y. P. Toporov, “Effect of contact deformations on the adhesion of particles,” *Journal of Colloid and interface science*, vol. 53, no. 2, pp. 314–326, 1975.

[31] D. Tabor, “Surface forces and surface interactions,” in *Plenary and invited lectures*, pp. 3–14, Elsevier, 1977.

[32] G. Carbone and F. Bottiglione, “Asperity contact theories: Do they predict linearity between contact area and load?,” *Journal of the Mechanics and Physics of Solids*, vol. 56, no. 8, pp. 2555–2572, 2008.

[33] B. N. J. Persson, *Sliding friction: physical principles and applications*. Springer Science & Business Media, 2013.

[34] J. H. Dieterich and B. D. Kilgore, “Direct observation of frictional contacts: New insights for state-dependent properties,” *Pure and Applied Geophysics*, vol. 143, no. 1, pp. 283–302, 1994.

[35] S. M. Rubinstein, G. Cohen, and J. Fineberg, “Detachment fronts and the onset of dynamic friction,” *Nature*, vol. 430, no. 7003, pp. 1005–1009, 2004.

[36] T. Suhina, B. Weber, C. E. Carpentier, K. Lorincz, P. Schall, D. Bonn, and A. M. Brouwer, “Fluorescence microscopy visualization of contacts between objects,” *Angewandte Chemie*, vol. 127, no. 12, pp. 3759–3762, 2015.

[37] D. Petrova, B. Weber, C. Allain, P. Audebert, C. H. Venner, A. M. Brouwer, and D. Bonn, “Fluorescence microscopy visualization of the roughness-induced transition between lubrication regimes,” *Science advances*, vol. 5, no. 12, p. eaaw4761, 2019.

[38] M. H. Müser, W. B. Dapp, R. Bugnicourt, P. Sainsot, N. Lesaffre, T. A. Lubrecht, B. N. J. Persson, K. Harris, A. Bennett, K. Schulze, *et al.*, "Meeting the contact-mechanics challenge," *Tribology Letters*, vol. 65, no. 4, p. 118, 2017.

[39] D. Tabor and R. H. S. Winterton, "The direct measurement of normal and retarded van der waals forces," *Proceedings of the Royal Society of London. A. Mathematical and Physical Sciences*, vol. 312, no. 1511, pp. 435–450, 1969.

[40] S. Y. Krylov and J. W. Frenken, "The physics of atomic-scale friction: Basic considerations and open questions," *physica status solidi (b)*, vol. 251, no. 4, pp. 711–736, 2014.

[41] J. Krim, "Friction and energy dissipation mechanisms in adsorbed molecules and molecularly thin films," *Advances in Physics*, vol. 61, no. 3, pp. 155–323, 2012.

[42] R. Hu, S. Y. Krylov, and J. W. Frenken, "On the origin of frictional energy dissipation," *Tribology Letters*, vol. 68, no. 1, pp. 1–13, 2020.

[43] K. Grosch, "The relation between the friction and visco-elastic properties of rubber," *Proceedings of the Royal Society of London. Series A. Mathematical and Physical Sciences*, vol. 274, no. 1356, pp. 21–39, 1963.

[44] M. Z. Baykara, M. R. Vazirisereshk, and A. Martini, "Emerging superlubricity: A review of the state of the art and perspectives on future research," *Applied Physics Reviews*, vol. 5, no. 4, p. 041102, 2018.

[45] F. P. Bowden, A. J. W. Moore, and D. Tabor, "The ploughing and adhesion of sliding metals," *Journal of Applied Physics*, vol. 14, no. 2, pp. 80–91, 1943.

[46] R. T. Spurr, "The "ploughing" contribution to friction," *British Journal of Applied Physics*, vol. 7, no. 7, p. 260, 1956.

[47] T. D. B. Jacobs and R. W. Carpick, "Nanoscale wear as a stress-assisted chemical reaction," *Nature nanotechnology*, vol. 8, no. 2, pp. 108–112, 2013.

[48] H. Spikes, "Stress-augmented thermal activation: Tribology feels the force," *Friction*, vol. 6, no. 1, pp. 1–31, 2018.

[49] M. A. Mekicha, M. B. de Rooij, T. Mishra, D. T. A. Matthews, L. Jacobs, and D. Schipper, "Study of wear particles formation at single asperity contact: An experimental and numerical approach," *Wear*, p. 203644, 2021.

[50] N. Mitarai and F. Nori, "Wet granular materials," *Advances in Physics*, vol. 55, no. 1-2, pp. 1–45, 2006.

[51] P. C. F. Møller and D. Bonn, "The shear modulus of wet granular matter," *Europhysics Letters*, vol. 80, no. 3, p. 38002, 2007.

[52] M. Dienwiebel, G. S. Verhoeven, N. Pradeep, J. W. Frenken, J. A. Heimberg, and H. W. Zandbergen, "Superlubricity of graphite," *Physical review letters*, vol. 92, no. 12, p. 126101, 2004.

[53] S. Zhang, Y. Hou, S. Li, L. Liu, Z. Zhang, X.-Q. Feng, and Q. Li, "Tuning friction to a superlubric state via in-plane straining," *Proceedings of the National Academy of Sciences*, vol. 116, no. 49, pp. 24452–24456, 2019.

[54] D. Tabor, "The hardness of solids," *Review of physics in technology*, vol. 1, no. 3, p. 145, 1970.

[55] Y.-T. Cheng and C.-M. Cheng, "Scaling, dimensional analysis, and indentation measurements," *Materials Science and Engineering: R: Reports*, vol. 44, no. 4-5, pp. 91–149, 2004.

[56] J. R. Trelewicz and C. A. Schuh, "The hall–petch breakdown in nanocrystalline metals: a crossover to glass-like deformation," *Acta Materialia*, vol. 55, no. 17, pp. 5948–5958, 2007.

[57] J. R. Greer, W. C. Oliver, and W. D. Nix, "Size dependence of mechanical properties of gold at the micron scale in the absence of strain gradients," *Acta Materialia*, vol. 53, no. 6, pp. 1821–1830, 2005.

[58] J. R. Greer and J. T. M. De Hosson, "Plasticity in small-sized metallic systems: Intrinsic versus extrinsic size effect," *Progress in Materials Science*, vol. 56, no. 6, pp. 654–724, 2011.

[59] D. Tabor, "Mohs's hardness scale-a physical interpretation," *Proceedings of the Physical Society. Section B*, vol. 67, no. 3, p. 249, 1954.

[60] K. Herrmann *et al.*, *Hardness testing: principles and applications*. ASM international, 2011.

[61] S. N. Petrenko, *Relationships Between the Rockwell and Brinell Numbers*. US Government Printing Office, 1927.

[62] `https://www.tribonet.org/`. Accessed: 2021-02-13.

[63] I. A. Polonsky and L. M. Keer, “A numerical method for solving rough contact problems based on the multi-level multi-summation and conjugate gradient techniques,” *Wear*, vol. 231, no. 2, pp. 206–219, 1999.

[64] K. L. Johnson, J. A. Greenwood, and S. Y. Poon, “A simple theory of asperity contact in elastohydro-dynamic lubrication,” *Wear*, vol. 19, no. 1, pp. 91–108, 1972.

[65] C. Jacq, D. Nélias, G. Lormand, and D. Girodin, “Development of a three-dimensional semi-analytical elastic-plastic contact code,” *Journal of Tribology*, vol. 124, no. 4, pp. 653–667, 2002.

[66] A. Akchurin, R. Bosman, P. M. Lugt, and M. van Drogen, “On a model for the prediction of the friction coefficient in mixed lubrication based on a load-sharing concept with measured surface roughness,” *Tribology letters*, vol. 59, no. 1, p. 19, 2015.

[67] A. Akchurin, *Generation of wear particles in lubricated contacts during running-in*. PhD thesis, University of Twente, 2017.

[68] A. G. Bengough, B. M. McKenzie, P. D. Hallett, and T. A. Valentine, “Root elongation, water stress, and mechanical impedance: a review of limiting stresses and beneficial root tip traits,” *Journal of Experimental Botany*, vol. 62, no. 1, pp. 59–68, 2011.

[69] A. M. Abdalla, D. R. P. Hettiaratchi, and A. R. Reece, “The mechanics of root growth in granular media,” *Journal of Agricultural Engineering Research*, vol. 14, no. 3, pp. 236–248, 1969.

[70] B. D. Texier, A. Ibarra, and F. Melo, “Low-resistive vibratory penetration in granular media,” *PloS one*, vol. 12, no. 4, p. e0175412, 2017.

[71] C. Li, T. Zhang, and D. I. Goldman, “A terradynamics of legged locomotion on granular media,” *Science*, vol. 339, no. 6126, pp. 1408–1412, 2013.

[72] D. Griffiths, “The feeding biology of ant-lion larvae: prey capture, handling and utilization,” *The Journal of Animal Ecology*, pp. 99–125, 1980.

[73] J. Crassous, A. Humeau, S. Boury, and J. Casas, “Pressure-dependent friction on granular slopes close to avalanche,” *Physical Review letters*, vol. 119, no. 5, p. 058003, 2017.

[74] J. P. Hambleton, S. Stanier, D. J. White, and S. W. Sloan, “Modelling ploughing and cutting processes in soils,” *Australian Geomechanics Journal*, vol. 49, no. 4, pp. 147–156, 2014.

[75] F. J. Muzzio, T. Shinbrot, and B. J. Glasser, “Powder technology in the pharmaceutical industry: the need to catch up fast,” 2002.

[76] V. Matousek, “Pressure drops and flow patterns in sand-mixture pipes,” *Experimental thermal and fluid science*, vol. 26, no. 6-7, pp. 693–702, 2002.

[77] J. Duran, *Sands, powders, and grains: an introduction to the physics of granular materials*. New York: Springer, 2000.

[78] M. Badetti, A. Fall, F. Chevoir, and J.-N. Roux, “Shear strength of wet granular materials: Macroscopic cohesion and effective stress,” *The European Physical Journal E*, vol. 41, no. 5, p. 68, 2018.

[79] K. M. Frye and C. Marone, “Effect of humidity on granular friction at room temperature,” *Journal of Geophysical Research: Solid Earth*, vol. 107, no. B11, 2002.

[80] O. Dorostkar, R. A. Guyer, P. A. Johnson, C. Marone, and J. Carmeliet, “Cohesion-induced stabilization in stick-slip dynamics of weakly wet, sheared granular fault gouge,” *Journal of Geophysical Research: Solid Earth*, vol. 123, no. 3, pp. 2115–2126, 2018.

[81] L. Kovalcinova, S. Karmakar, M. Schaber, A.-L. Schuhmacher, M. Scheel, M. DiMichiel, M. Brinkmann, R. Seemann, and L. Kondic, “Energy dissipation in sheared wet granular assemblies,” *Physical Review E*, vol. 98, no. 3, p. 032905, 2018.

[82] J. Duriez, M. Eghbalian, R. Wan, and F. Darve, “The micromechanical nature of stresses in triphasic granular media with interfaces,” *Journal of the Mechanics and Physics of Solids*, vol. 99, pp. 495–511, 2017.

[83] M. Pakpour, M. Habibi, P. Møller, and D. Bonn, “How to construct the perfect sandcastle,” *Scientific reports*, vol. 2, p. 549, 2012.

[84] J. O. Marston, I. U. Vakarelski, and S. T. Thoroddsen, “Sphere impact and penetration into wet sand,” *Physical Review E*, vol. 86, no. 2, p. 020301, 2012.

[85] M. Scheel, R. Seemann, M. D. M. M. Brinkmann, M. Di Michiel, A. Sheppard, B. Breidenbach, and S. Herminghaus, “Morphological clues to wet granular pile stability,” *Nature materials*, vol. 7, no. 3, p. 189, 2008.

[86] M. Badetti, A. Fall, D. Hautemayou, F. Chevoir, P. Aimedieu, S. Rodts, and J.-N. Roux, “Rheology and microstructure of unsaturated wet granular materials: Experiments and simulations,” *Journal of Rheology*, vol. 62, no. 5, pp. 1175–1186, 2018.

[87] V. Richefeu, M. S. El Youssoufi, and F. Radjai, “Shear strength properties of wet granular materials,” *Physical Review E*, vol. 73, no. 5, p. 051304, 2006.

[88] M. Aliasgari, N. Maleki-Jirsaraei, and S. Rouhani, “The effect of grain size and shape on sliding friction of wet granular media,” *Zeitschrift für Physikalische Chemie*, 2019.

[89] Z. Fournier, D. Geromichalos, S. Herminghaus, M. M. Kohonen, F. Mugele, M. Scheel, M. Schulz, B. Schulz, C. Schier, R. Seemann, *et al.*, “Mechanical properties of wet granular materials,” *Journal of Physics: Condensed Matter*, vol. 17, no. 9, p. S477, 2005.

[90] M. Dinkgreve, J. Paredes, M. M. Denn, and D. Bonn, “On different ways of measuring “the” yield stress,” *Journal of non-Newtonian fluid mechanics*, vol. 238, pp. 233–241, 2016.

[91] R. Rosenberg, “Why is ice slippery?,” *Physics Today*, vol. 58, no. 12, p. 50, 2005.

[92] J. Joly, “The phenomena of skating,” *Scientific Proceedings of the Royal Society*, vol. 5, no. 453, 1886.

[93] F. P. Bowden and T. P. Hughes, “The mechanism of sliding on ice and snow,” *Proceedings of the Royal Society of London. Series A. Mathematical and Physical Sciences*, vol. 172, no. 949, pp. 280–298, 1939.

[94] P. Faraday, “Xxiv. on regelation, and on the conservation of force,” *The London, Edinburgh, and Dublin Philosophical Magazine and Journal of Science*, vol. 17, no. 113, pp. 162–169, 1859.

[95] S. Colbeck, “The kinetic friction of snow,” *Journal of Glaciology*, vol. 34, no. 116, pp. 78–86, 1988.

[96] J. J. de Koning, G. De Groot, and G. J. van Ingen Schenau, “Ice friction during speed skating,” *Journal of biomechanics*, vol. 25, no. 6, pp. 565–571, 1992.

[97] A.-M. Kietzig, S. G. Hatzikiriakos, and P. Englezos, "Ice friction: the effects of surface roughness, structure, and hydrophobicity," *Journal of Applied Physics*, vol. 106, no. 2, p. 024303, 2009.

[98] A.-M. Kietzig, S. G. Hatzikiriakos, and P. Englezos, "Physics of ice friction," *Journal of Applied Physics*, vol. 107, no. 8, p. 4, 2010.

[99] A. J. Tuononen, A. Kriston, and B. Persson, "Multiscale physics of rubber-ice friction," *The Journal of Chemical Physics*, vol. 145, no. 11, p. 114703, 2016.

[100] A. Spagni, A. Berardo, D. Marchetto, E. Gualtieri, N. M. Pugno, and S. Valeri, "Friction of rough surfaces on ice: Experiments and modeling," *Wear*, vol. 368, pp. 258–266, 2016.

[101] J. M. J. van Leeuwen, "Skating on slippery ice," *SciPost Physics*, vol. 3, no. 6, p. 042, 2017.

[102] M. Ovaska and A. J. Tuononen, "Multiscale imaging of wear tracks in ice skate friction," *Tribology International*, vol. 121, pp. 280–286, 2018.

[103] B. Slater and A. Michaelides, "Surface premelting of water ice," *Nature Reviews Chemistry*, p. 1, 2019.

[104] Y. Nagata, T. Hama, E. H. G. Backus, M. Mezger, D. Bonn, M. Bonn, and G. Sazaki, "The surface of ice under equilibrium and nonequilibrium conditions," *Accounts of chemical research*, vol. 52, no. 4, pp. 1006–1015, 2019.

[105] B. Weber, Y. Nagata, S. Ketzetzi, F. Tang, W. J. Smit, H. J. Bakker, E. H. G. Backus, M. Bonn, and D. Bonn, "Molecular insight into the slipperiness of ice," *The journal of physical chemistry letters*, vol. 9, no. 11, pp. 2838–2842, 2018.

[106] F.-C. Hsia, F. M. Elam, D. Bonn, B. Weber, and S. E. Franklin, "Wear particle dynamics drive the difference between repeated and non-repeated reciprocated sliding," *Tribology International*, vol. 142, p. 105983, 2020.

[107] L. Canale, J. Comtet, A. Niguès, C. Cohen, C. Clanet, A. Siria, and L. Bocquet, "Nanorheology of interfacial water during ice gliding," *Physical Review X*, vol. 9, no. 4, p. 041025, 2019.

[108] B. Weber, Y. Nagata, S. Ketzetzi, F. Tang, W. J. Smit, H. J. Bakker, E. H. G. Backus, M. Bonn, and D. Bonn, "Molecular insight into the slipperiness of ice," *The journal of physical chemistry letters*, vol. 9, no. 11, pp. 2838–2842, 2018.

[109] W. D. Kingery, "Regelation, surface diffusion, and ice sintering," *Journal of Applied Physics*, vol. 31, no. 5, pp. 833–838, 1960.

[110] S. Neshyba, I. Gladich, W. Pfalzgraff, O. Maršálek, P. Jungwirth, M. Roeselová, *et al.*, "Arrhenius analysis of anisotropic surface diffusion on the prismatic facet of ice," *Physical Chemistry Chemical Physics*, 2011.

[111] K. Tusima, "Friction of a steel ball on a single crystal of ice," *Journal of Glaciology*, vol. 19, no. 81, pp. 225–235, 1977.

[112] M. Denny, *Gliding for gold: the physics of winter sports*. JHU Press, 2011.

[113] J. M. J. van Leeuwen, "The friction of tilted skates on ice," *SciPost Physics*, vol. 8, no. 4, p. 059, 2020.

[114] B. N. J. Persson, "Theory of rubber friction and contact mechanics," *The Journal of Chemical Physics*, vol. 115, no. 8, pp. 3840–3861, 2001.

[115] C. Barus, "Isothermals, isopiestics and isometrics relative to viscosity," *American Journal of Science*, vol. 45, no. 266, p. 87, 1893.

[116] S. Bair and P. Kottke, "Pressure-viscosity relationships for elastohydrodynamics," *Tribology transactions*, vol. 46, no. 3, pp. 289–295, 2003.

[117] R. C. Major, J. E. Houston, M. J. McGrath, J. I. Siepmann, and X.-Y. Zhu, "Viscous water meniscus under nanoconfinement," *Physical review letters*, vol. 96, no. 17, p. 177803, 2006.

[118] J. Gao, R. Szoszkiewicz, U. Landman, E. Riedo, *et al.*, "Structured and viscous water in subnanometer gaps," *Physical Review B*, vol. 75, no. 11, p. 115415, 2007.

[119] D. Ortiz-Young, H.-C. Chiu, S. Kim, K. Voïtchovsky, and E. Riedo, "The interplay between apparent viscosity and wettability in nanoconfined water," *Nature communications*, vol. 4, no. 1, pp. 1–6, 2013.

[120] B. Jacobson, "The stribeck memorial lecture," *Tribology International*, vol. 36, no. 11, pp. 781–789, 2003.

[121] M. D. Hersey, "The laws of lubrication of horizontal journal bearings," *Journal of the Washington Academy of Sciences*, vol. 4, no. 19, pp. 542–552, 1914.

[122] T. R. Butkovich, "Hardness of single ice crystals," *American Mineralogist: Journal of Earth and Planetary Materials*, vol. 43, no. 1-2, pp. 48–57, 1958.

[123] P. Barnes and D. Tabor, "Plastic flow and pressure melting in the deformation of ice i," *Nature*, vol. 210, no. 5039, pp. 878–882, 1966.

[124] P. Barnes, D. Tabor, and J. C. F. Walker, "The friction and creep of polycrystalline ice," *Proceedings of the Royal Society of London. A. Mathematical and Physical Sciences*, vol. 324, no. 1557, pp. 127–155, 1971.

[125] J. A. Schaefer, R. Ettema, and W. A. Nixon, "Measurements of icing hardness," *Cold regions science and technology*, vol. 17, no. 1, pp. 89–93, 1989.

[126] L. Poirier, E. P. Lozowski, and R. I. Thompson, "Ice hardness in winter sports," *Cold Regions Science and Technology*, vol. 67, no. 3, pp. 129–134, 2011.

[127] E. Lozowski, K. Szilder, and S. Maw, "A model of ice friction for a speed skate blade," *Sports Engineering*, vol. 16, no. 4, pp. 239–253, 2013.

[128] L. Makkonen and M. Tikanmäki, "Modeling the friction of ice," *Cold Regions Science and Technology*, vol. 102, pp. 84–93, 2014.

[129] B. N. J. Persson, "Ice friction: Role of non-uniform frictional heating and ice premelting," *The Journal of chemical physics*, vol. 143, no. 22, p. 224701, 2015.

[130] S. C. Colbeck, "A review of the friction of snow skis," *Journal of sports sciences*, vol. 12, no. 3, pp. 285–295, 1994.

[131] A. Döppenschmidt and H.-J. Butt, "Measuring the thickness of the liquid-like layer on ice surfaces with atomic force microscopy," *Langmuir*, vol. 16, no. 16, pp. 6709–6714, 2000.

[132] H. Bluhm, D. F. Ogletree, C. S. Fadley, Z. Hussain, and M. Salmeron, "The premelting of ice studied with photoelectron spectroscopy," *Journal of Physics: Condensed Matter*, vol. 14, no. 8, p. L227, 2002.

[133] K.-i. Murata, H. Asakawa, K. Nagashima, Y. Furukawa, and G. Sazaki, "Thermodynamic origin of surface melting on ice crystals," *Proceedings of the National Academy of Sciences*, vol. 113, no. 44, pp. E6741–E6748, 2016.

[134] M. A. Sánchez, T. Kling, T. Ishiyama, M.-J. van Zadel, P. J. Bisson, M. Mezger, M. N. Jochum, J. D. Cyran, W. J. Smit, H. J. Bakker, *et al.*, "Experimental and theoretical evidence for bilayer-by-bilayer surface melting of crystalline ice," *Proceedings of the National Academy of Sciences*, vol. 114, no. 2, pp. 227–232, 2017.

[135] R. Grönqvist, "Mechanisms of friction and assessment of slip resistance of new and used footwear soles on contaminated floors," *Ergonomics*, vol. 38, no. 2, pp. 224–241, 1995.

[136] O. Bobjer, S.-E. Johansson, and S. Piguet, "Friction between hand and handle. effects of oil and lard on textured and non-textured surfaces; perception of discomfort," *Applied Ergonomics*, vol. 24, no. 3, pp. 190–202, 1993.

[137] I. Sherrington and E. H. Smith, "The significance of surface topography in engineering," *Precision engineering*, vol. 8, no. 2, pp. 79–87, 1986.

[138] T. R. Thomas and T. R. Thomas, *Rough surfaces*, vol. 278. World Scientific, 1999.

[139] P. L. Menezes, S. V. Kailas, and M. R. Lovell, "Role of surface texture, roughness, and hardness on friction during unidirectional sliding," *Tribology letters*, vol. 41, no. 1, pp. 1–15, 2011.

[140] G. A. Pilkington, E. Thormann, P. M. Claesson, G. M. Fuge, O. J. Fox, M. N. Ashfold, H. Leese, D. Mattia, and W. H. Briscoe, "Amontonian frictional behaviour of nanostructured surfaces," *Physical Chemistry Chemical Physics*, vol. 13, no. 20, pp. 9318–9326, 2011.

[141] J. Archard, "Contact and rubbing of flat surfaces," *Journal of applied physics*, vol. 24, no. 8, pp. 981–988, 1953.

[142] J. Jiang and R. D. Arnell, "The effect of substrate surface roughness on the wear of dlc coatings," *Wear*, vol. 239, no. 1, pp. 1–9, 2000.

[143] T. Pöschel and H. J. Herrmann, "A simple geometrical model for solid friction," *Physica A: Statistical Mechanics and its Applications*, vol. 198, no. 3-4, pp. 441–448, 1993.

[144] S. M. Rubinstein, G. Cohen, and J. Fineberg, "Visualizing stick–slip: experimental observations of processes governing the nucleation of frictional sliding," *Journal of Physics D: Applied Physics*, vol. 42, no. 21, p. 214016, 2009.

[145] J. L. Gupta and G. Deheri, "Effect of roughness on the behavior of squeeze film in a spherical bearing," *Tribology Transactions*, vol. 39, no. 1, pp. 99–102, 1996.

[146] H. A. Spikes, "Mixed lubrication—an overview," *Lubrication Science*, vol. 9, no. 3, pp. 221–253, 1997.

[147] J. M. Martin, C. Donnet, T. Le Mogne, and T. Epicier, "Superlubricity of molybdenum disulphide," *Physical Review B*, vol. 48, no. 14, p. 10583, 1993.

[148] A. Erdemir and O. Eryilmaz, "Achieving superlubricity in dlc films by controlling bulk, surface, and tribochemistry," *Friction*, vol. 2, no. 2, pp. 140–155, 2014.

[149] M. R. Vazirisereshk, K. Hasz, R. W. Carpick, and A. Martini, "Friction anisotropy of mos2: Effect of tip–sample contact quality," *The journal of physical chemistry letters*, vol. 11, no. 16, pp. 6900–6906, 2020.

[150] S. E. Tomlinson, M. Carré, R. Lewis, and S. E. Franklin, "Human finger contact with small, triangular ridged surfaces," *Wear*, vol. 271, no. 9-10, pp. 2346–2353, 2011.

[151] L.-W. Liu, Y. H. Lee, C. J. Lin, K. W. Li, and C. Y. Chen, "Shoe sole tread designs and outcomes of slipping and falling on slippery floor surfaces," *PloS one*, vol. 8, no. 7, p. e68989, 2013.

[152] D. Gropper, L. Wang, and T. J. Harvey, "Hydrodynamic lubrication of textured surfaces: A review of modeling techniques and key findings," *Tribology International*, vol. 94, pp. 509–529, 2016.

[153] "Clear resin, FLGPCL04, from formlabs." `https://formlabs-media.formlabs.com/datasheets/Clear_Resin_Technical.pdf`. Accessed: 2020-10-28.

[154] A. Rafsanjani, Y. Zhang, B. Liu, S. M. Rubinstein, and K. Bertoldi, "Kirigami skins make a simple soft actuator crawl," *Science Robotics*, vol. 3, no. 15, 2018.

[155] H. L. Costa and I. M. Hutchings, "Hydrodynamic lubrication of textured steel surfaces under reciprocating sliding conditions," *Tribology International*, vol. 40, no. 8, pp. 1227–1238, 2007.

[156] T. Ibatan, M. S. Uddin, and M. A. K. Chowdhury, "Recent development on surface texturing in enhancing tribological performance of bearing sliders," *Surface and Coatings Technology*, vol. 272, pp. 102–120, 2015.

[157] Z. Wang, Y.-B. Li, F. Bai, C.-W. Wang, and Q.-Z. Zhao, "Angle-dependent lubricated tribological properties of stainless steel by femtosecond laser surface texturing," *Optics & Laser Technology*, vol. 81, pp. 60–66, 2016.

[158] O. Hod, E. Meyer, Q. Zheng, and M. Urbakh, “Structural superlubricity and ultralow friction across the length scales,” *Nature*, vol. 563, no. 7732, pp. 485–492, 2018.

[159] Z. Liu, J. Yang, F. Grey, J. Z. Liu, Y. Liu, Y. Wang, Y. Yang, Y. Cheng, and Q. Zheng, “Observation of microscale superlubricity in graphite,” *Physical review letters*, vol. 108, no. 20, p. 205503, 2012.

[160] M. Hirano, K. Shinjo, R. Kaneko, and Y. Murata, “Anisotropy of frictional forces in muscovite mica,” *Physical review letters*, vol. 67, no. 19, p. 2642, 1991.

[161] H. T. Tramsen, S. N. Gorb, H. Zhang, P. Manoonpong, Z. Dai, and L. Heepe, “Inversion of friction anisotropy in a bio-inspired asymmetrically structured surface,” *Journal of the Royal Society Interface*, vol. 15, no. 138, p. 20170629, 2018.

[162] S. Ma, M. Scaraggi, C. Yan, X. Wang, S. N. Gorb, D. Dini, and F. Zhou, “Bioinspired 3d printed locomotion devices based on anisotropic friction,” *Small*, vol. 15, no. 1, p. 1802931, 2019.

[163] Y. Yang, M. A. Dias, and D. P. Holmes, “Multistable kirigami for tunable architected materials,” *Physical Review Materials*, vol. 2, no. 11, p. 110601, 2018.

[164] S. Babaee, S. Pajovic, A. Rafsanjani, Y. Shi, K. Bertoldi, and G. Traverso, “Bioinspired kirigami metasurfaces as assistive shoe grips,” *Nature Biomedical Engineering*, pp. 1–9, 2020.

[165] A. Lamoureux, K. Lee, M. Shlian, S. R. Forrest, and M. Shtein, “Dynamic kirigami structures for integrated solar tracking,” *Nature communications*, vol. 6, p. 8092, 2015.

[166] A. Rafsanjani and K. Bertoldi, “Buckling-induced kirigami,” *Physical review letters*, vol. 118, no. 8, p. 084301, 2017.

[167] Y. Tang, G. Lin, S. Yang, Y. K. Yi, R. D. Kamien, and J. Yin, “Programmable kiri-kirigami metamaterials,” *Advanced Materials*, vol. 29, no. 10, p. 1604262, 2017.

[168] D. L. Hu, J. Nirody, T. Scott, and M. J. Shelley, “The mechanics of slithering locomotion,” *Proceedings of the National Academy of Sciences*, vol. 106, no. 25, pp. 10081–10085, 2009.

[169] H. Marvi and D. L. Hu, “Friction enhancement in concertina locomotion of snakes,” *Journal of the Royal Society Interface*, vol. 9, no. 76, pp. 3067–3080, 2012.

[170] A. Ion, R. Kovacs, O. S. Schneider, P. Lopes, and P. Baudisch, "Metamaterial textures," in *Proceedings of the 2018 CHI Conference on Human Factors in Computing Systems*, pp. 1–12, 2018.

[171] Z. Mróz and S. Stupkiewicz, "An anisotropic friction and wear model," *International journal of solids and structures*, vol. 31, no. 8, pp. 1113–1131, 1994.

[172] N. Antoni, J.-L. Ligier, P. Saffré, and J. Pastor, "Asymmetric friction: Modelling and experiments," *International journal of engineering science*, vol. 45, no. 2-8, pp. 587–600, 2007.

[173] J. E. Field, *The properties of diamond*. Academic Press, 1979.

[174] I. J. Ford, "Roughness effect on friction for multi-asperity contact between surfaces," *Journal of Physics D: Applied Physics*, vol. 26, no. 12, p. 2219, 1993.

[175] D. V. Schroeder, *An introduction to thermal physics*. American Association of Physics Teachers, 1999.

[176] K. L. Johnson, "Contact mechanics," *Cambridge*, vol. 95, p. 365, 1985.

Summary

From pushing a bookcase over the floor to the relative motion of tectonic plates or sliding a newly hewn statue over land — as the ancient Egyptians did — to ice skating on frozen canals, a resistance against sliding counteracts all these movements and tries to hold the surfaces in place.

Leonardo Da Vinci already observed that this friction force increases linearly with the normal force, or with the mass of the sliding object. In terms of the opening example, it is therefore better to empty the bookcase prior to sliding it over the floor. The ratio of the friction force and the normal force is known as the friction coefficient μ and can be defined for the specific sliding system. Typically, a bookcase has a friction coefficient in the range of $\mu \approx 0.2 - 0.4$, largely depending on the exact conditions and materials. A wide variety of friction coefficients can be found. For example, ice can be as slippery as $\mu = 0.07$, whereas a rubber shoe on the pavement has good grip due to a friction coefficient around 0.8.

It is complex to predict a friction coefficient and even more difficult to control it. In this thesis, we make a contribution to answering the seemingly simple question, 'What controls sliding friction?' We aimed to bridge the gap between macroscopically observed sliding friction and the underlying microscopic behaviour at the interface between the sliding surfaces. We performed sliding experiments using various shapes — spheres, plates, model ice skates — and various degrees of surface roughness — as smooth as a magnifying glass or as rough as sandpaper — to measure the friction force. We focused on three very different types of surfaces, namely wet sand, ice, and a collection of artificial surfaces whose geometry we can precisely control, to gain a better understanding of the sliding friction and, where possible, control over sliding friction.

After a general introduction and description of the experimental and computational techniques in **Chapters 1 and 2**, **Chapter 3** describes the ploughing friction on wet and dry sand. The mechanics of granular materials such as sand is greatly impacted by the presence of a small amount of water; this dynamic is something that we can experience in daily life as well. For example, walking on the beach is easier on slightly wet sand, but sand that is too muddy or too dry costs more effort. When water is added to sand, liquid bridges form between neighbouring grains which bind them together, resulting in a cohesive material. Adding more water to the mixture generates coalescence of the liquid bridges and thereby decreases the strength of the binding between the grains. In Chapter 3, we study the influence of the water volume fraction in sand on sliding friction and question the role of the slider geometry. To measure this, we slid a hemisphere over partially saturated sand and found that the addition of a small amount of water makes the friction force sharply drop, whereas too much added water causes the friction force to increase again. We found that ploughing is the main mechanism as is evident by a deep trace in the sand after the passage of the slider. How deep the hemisphere sinks into the wet sand is controlled by the hardness of the water-sand mixture which is greatly influenced by the presence of a small amount of water. The hardness sets the size of the ploughing trace and the force required to plough through the water-sand mixture. We present a ploughing model that quantitatively reproduces the observed ploughing friction based on the hardness of the water-sand mixture. Adding some — but not too much — water results in an increase in hardness, a shallow trace in the sand and, consequently, less ploughing friction for the hemisphere.

The influence of water on sand seemed to be known by the ancient Egyptians; a celebrated tomb drawing suggests that for the transportation of a large statue through the desert, one person was pouring water in front of the sledge to decrease the friction. In **Chapter 4**, we recreated the transportation of a 'statue' over wet sand in miniature. We measured the sliding friction of a sledge with a dead weight as the 'statue' on wet sand and measured the hardness of the water-sand mixture directly after sliding. As expected, the sliding friction of a sledge on wet sand is strongly influenced by the water fraction. By adding a small amount of water, the hardness of the wet sand is at its maximum and the sliding sledge will not plough through it, thereby minimising the sliding friction. Thus, pouring a limited amount of water in front of a sledge greatly reduces the manpower necessary to transport a statue.

In **Chapter 5**, we address the slipperiness of ice. We slid various types of ice skates over a miniature ice skating rink while measuring the friction force as a function of temperature, geometry and speed. It is commonly believed that ice is slippery due to the presence of a thin layer of liquid water on top of the ice surface which lubricates the surface. The origin of this liquid water, however, remains highly debated. The first and since disproven explanation was based on pressure melting, wherein the local pressure of a skate on the ice results in the ice melting into liquid water. However, pressure melting requires unrealistically high contact pressures, in particular at ice temperatures below -3.5 °C, which are easily reached in frozen canals and on speed skating rinks. In our experiment, we measured the friction coefficient and, combined with contact mechanics calculations, observed that ice is slippery because of the diffusive motion of surface ice molecules. Ice is not always slippery; the mobility of the surface ice molecules — and therefore the slipperiness of the ice — can be suppressed by a high contact pressure or a low temperature. In addition, we observed rich ploughing close to the melting point, controlled by the hardness of the ice and the surface geometry. A ploughing model can therefore not only reproduce the measured friction when scratching (wet) sand but is also applicable to ice skating. We concluded that it is the high mobility of molecules in the outermost layer of the ice combined with the exceptional hardness of ice close to its melting point that cause its slipperiness. Ice friction can be minimised by curtailing the contact pressure, a factor already controlled by ice skaters: the optimal ice skate has a smooth bottom (low pressure) for low friction and sharp edges (high pressure) for grip.

In **Chapter 6**, we explored how one can tune friction with surfaces whose roughness can be precisely controlled. Roughness influences sliding friction even in everyday scenarios; two smooth surfaces slide more easily over each other than two rough ones. However, the direct influence of surface roughness is often hard to foresee and control. Customising friction for a specific application with a tuning parameter, such as surface roughness, would be of interest; high friction for grip and low friction for easy sliding. In this chapter, we investigated the sliding friction between geometrically patterned surfaces, i.e., surface patterns of a few millimetres in height. We demonstrated that well-designed surface roughness and control of the (mis)match between the surface roughness on the surfaces allows one to vary the friction force by more than an order of magnitude. The sliding friction can therefore be directly controlled by the interface geometry of the macroscopic surface patterns on custom-made surfaces. We include a simple geometrical model that quantitatively reproduces the tuning of friction with macroscopic surface patterns. In addition, we discuss the sliding friction on Kirigami metamaterial surfaces that allow friction to be tuned externally by a direct variation of its roughness. Kirigami is a Japanese artform in which a sheet of paper can be transformed into 3D structures based on cutting. We make use of a Kirigami cutting pattern to increase surface roughness by uniaxially stretching out the flat sheet. External control of surface roughness thus allows the sliding friction to be tuned on a Kirigami metamaterial surface.

Overall, this thesis provides new insights into the slipperiness of sand, ice, and geometrically controlled surfaces, including their dependency on the microscopic behaviour of the sliding interface. We show that the microscopic and macroscopic geometry of the surfaces together with (i) the water fraction in sand, (ii) the temperature of ice and (iii) the (mis)match between the surface roughness on the surfaces, control the sliding friction (see Fig. S.3).

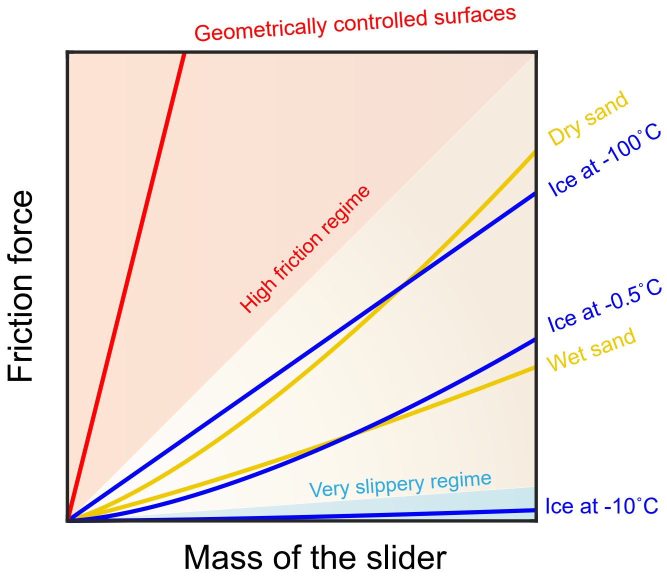

Figure S.3: Friction force as a function of the mass of the slider, summarising the influence of (i) water fraction on the sliding friction of sand, (ii) the temperature of ice on its slipperiness, and (iii) artificial surface roughness on the sliding friction of geometrically controlled surfaces. The continuous lines represent the normalised measured data for sand, ice, and geometrically controlled surfaces as presented in Chapters 3, 5 and 6. The blue and red regimes represent the slippery ($\mu \lesssim 0.07$) and highly non-slippery ($\mu \gtrsim 1$) regimes. 'Dry sand' and 'Wet sand' are the measured friction for sliding a hemisphere over sand with a water volume fraction of $\phi_w = 0\%$ and $\phi_w = 8\%$, respectively (see Fig. 3.2). 'Ice at -0.5 °C', 'Ice at -10 °C', and 'Ice at -100 °C' represent the sliding friction on ice for sliding a small sphere ($R = 0.75$ mm), a big sphere ($R = 6$ mm) and a model ice skate, respectively (see Figs. 5.1 and 5.2). 'Geometrically controlled surfaces' is the measured sliding friction between two aluminium sliders with a sawtooth-patterned surface ($\theta = 70°$, see Fig. 6.4).

Samenvatting

Van het over de vloer duwen van een boekenkast tot het langs elkaar schuren van twee tektonische platen, of van het voortschuiven van een nieuw gebeiteld standbeeld (zoals de oude Egyptenaren het deden) tot schaatsen over bevroren grachten — er is een weerstand die al deze vormen van glijden tegenwerkt en probeert de oppervlakken op hun plaats te houden.

Leonardo Da Vinci observeerde al dat deze wrijvingskracht lineair toeneemt met de normaalkracht, ook wel beschreven met het gewicht van het glijdende object. In het openingsvoorbeeld is het dus beter de boekenkast leeg te ruimen voordat deze over de vloer wordt geschoven. De verhouding van de wrijvingskracht tot de normaalkracht wordt ook wel de wrijvingscoëfficiënt μ genoemd en kan voor elk specifiek wrijvingssysteem worden vastgesteld. Een boekenkast heeft doorgaans een wrijvingscoëfficiënt in het bereik van $\mu \approx 0.2 - 0.4$, afhankelijk van de exacte omstandigheden en materialen. Er bestaan dus grote verschillen in wrijvingscoëfficiënten. IJs bijvoorbeeld kan zo glibberig zijn als $\mu = 0.07$, terwijl een rubberen schoen op de stoep grip heeft met een wrijvingscoëfficiënt rond de 0.8.

Het voorspellen van een wrijvingscoëfficiënt is complex, het regelen ervan nog lastiger. In dit proefschrift wordt een bijdrage geleverd aan het antwoord op de ogenschijnlijk simpele vraag "Waardoor wordt de wrijvingskracht bepaald?" Het onderzoek was erop gericht de kloof te overbruggen tussen de macroscopisch geobserveerde wrijvingskracht en het onderliggende microscopische gedrag op het grensvlak tussen de glijdende oppervlakken. Hiervoor zijn glij-experimenten uitgevoerd met verscheidene vormen (bollen, platen en een modelschaats) en verscheidene gradaties van ruwheid (van zo glad als een lens tot zo ruw als schuurpapier), waarbij steeds de wrijvingskracht werd gemeten. We hebben drie verschillende soorten oppervlakken gebruikt, namelijk nat zand, ijs en een reeks kunstmatige oppervlakken. Van deze laatste kon de precieze geometrie worden ingesteld, om zo meer kennis te vergaren over de wrijvingscoëfficiënt en deze waar mogelijk te beheersen.

Na een algemene introductie en een beschrijving van de toegepaste experimentele en numerieke technieken in **Hoofdstukken 1 en 2**, wordt in **Hoofdstuk 3** de glijweerstand over nat en droog zand beschreven. De mechanica van granulaire materialen zoals zand wordt sterk beïnvloed door de aanwezigheid van water, zelfs in een kleine hoeveelheid — een effect dat in het dagelijks leven ook kan worden ervaren: bij bijvoorbeeld een strandwandeling loopt gedeeltelijk nat zand immers het makkelijkst, terwijl volledig droog of heel modderig zand het wandelen erg moeilijk kan maken. Wanneer water wordt toegevoegd aan zand ontstaan vloeistofbruggen tussen de zandkorrels, die deze aan elkaar binden; daardoor ontstaat een samenhangend materiaal. Het toevoegen van meer water aan het mengsel veroorzaakt echter dat de waterbruggen samenvloeien, waardoor de sterkte van de binding afneemt. In Hoofdstuk 3 wordt daarom verslag gedaan van onderzoek naar de invloed die de volumefractie van water in zand heeft op de wrijvingskracht, en naar de rol van de geometrie van het glijdende object. Hiervoor is een halve bol over gedeeltelijk verzadigd zand getrokken, waaruit bleek dat de toevoeging van een kleine hoeveelheid water de wrijvingskracht sterk doet dalen, terwijl een grotere hoeveelheid toegevoegd water de wrijvingskracht weer laat toenemen. Ploegen is het belangrijkste mechanisme dat hier speelt, wat zichtbaar is aan een diep spoor in het zand wanneer het glijdende object gepasseerd is. Hoe diep de halve bol in het natte zand wegzakt, wordt bepaald door de hardheid van het water-zandmengsel, die weer sterk afhangt van de hoeveelheid water die in dit mengsel aanwezig is. De hardheid bepaalt de grootte van het ploegspoor en de wrijvingskracht die nodig is om door het water-zandmengsel te ploegen. In dit hoofdstuk wordt een ploegmodel gepresenteerd dat de gemeten wrijvingskracht kwantitatief reproduceert, gebaseerd op de gemeten hardheid van het water-zandmengsel. Het toevoegen van een beetje — maar vooral niet te veel — water aan zand geeft een toename van de hardheid, een ondiep spoor in het zand, en daardoor minder ploegfrictie voor de glijdende halve bol.

De invloed van water op de mechanica van zand lijkt al bekend te zijn geweest bij de oude Egyptenaren; een befaamde muurtekening in een tombe suggereert dat tijdens het vervoer van een groot standbeeld door de woestijn een persoon water op de grond voor de gebruikte slede giet om de wrijvingskracht te verlagen. In **Hoofdstuk 4** wordt de wrijvingskracht beschreven van een slede waarop als 'standbeeld' een gewicht is gezet en die over nat zand wordt getrokken. Direct na de wrijvingstest is de hardheid van het gebruikte water-zandmengsel gekwantificeerd. Zoals verwacht, bleek de weerstand die wordt ervaren sterk afhankelijk van de waterfractie in het zand. Wanneer een kleine hoeveelheid water wordt toegevoegd, is de hardheid van het water-zandmengsel maximaal, waardoor de glijweerstand minimaal is. Het toevoegen van een kleine hoeveelheid water, in de glijrichting vóór de slede, geeft dus een sterke afname van de kracht die nodig is om deze voort te trekken.

In **Hoofdstuk 5**, wordt de glibberigheid van ijs besproken. We laten verschillende typen schaatsen over een miniatuur schaatsbaan glijden, terwijl we de wrijvingskracht als functie van de temperatuur, de geometrie en de snelheid hebben gemeten. Algemeen wordt aangenomen dat ijs glibberig is door de aanwezigheid van een dunne laag water op het ijsoppervlak die als smeermiddel dient. Het ontstaan van deze vloeibare waterlaag blijft echter een onderwerp van hevige discussie. De eerste en sindsdien weerlegde verklaring was gebaseerd op smelten door druk: de lokale druk van een schaats op het ijs zou veroorzaken dat het ijs smelt. Voor dit smelteffect is echter een onrealistisch hoge druk nodig, zeker bij temperaturen lager dan -3.5 °C, die veelvuldig voorkomen in bevroren grachten en ijsbanen. In dit onderzoek is de wrijvingscoëfficiënt gemeten, waarna met berekeningen op basis van de contactmechanica is beschreven dat ijs glibberig is door de diffuse beweging van watermoleculen aan het oppervlak. Ook laten we zien dat ijs niet altijd glibberig is; de mobiliteit van de watermoleculen aan het oppervlak en dus de glibberigheid van ijs kan worden onderdrukt door de contactdruk te vergroten of de temperatuur te verlagen. Bovendien treedt nabij het smeltpunt van het ijs ploegen op, als gevolg van de hardheid van het ijs en de geometrie van de oppervlakken. Een ploegmodel is dus niet alleen toepasbaar op krassen door (nat) zand maar ook op schaatsen op ijs. We concluderen dat de hoge mobiliteit van watermoleculen aan het oppervlak en de exceptioneel hoge hardheid van ijs nabij het smeltpunt samen de glibberigheid van ijs veroorzaken. IJswrijving kan worden geminimaliseerd door de contactdruk te beperken, iets wat schaatsers van nature al doen: de optimale schaats heeft een gladde onderkant met door de lage druk een lage wrijvingsweerstand, en scherpe randen die ter plaatse zorgen voor de hoge druk die nodig is voor een goede grip.

In **Hoofdstuk 6** beschrijven we hoe wrijving kan worden geregeld met oppervlakken waarvan de ruwheid kan worden gekozen. De ruwheid heeft invloed op de wrijvingsweerstand, zoals iedereen weet uit dagelijkse situaties: twee gladde oppervlakken glijden gemakkelijker over elkaar dan twee ruwe. Echter, hoe de oppervlakteruwheid de wrijving precies beïnvloedt, is vaak moeilijk te voorzien en te regelen. Het voor een specifiek doeleinde aanpassen van de wrijving, door het instellen van een enkele parameter zoals de oppervlakteruwheid, kan aantrekkelijk zijn. Voor dit hoofdstuk is de wrijvingsweerstand onderzocht tussen oppervlakken met daarop geometrische patronen van een paar millimeter in hoogte. Daaruit blijkt dat goed ontworpen oppervlakteruwheden en een nauwkeurig geregelde (mis)match tussen deze oppervlakteruwheden het mogelijk maken de wrijvingskracht te variëren met meer dan een orde van grootte. De wrijvingsweerstand kan dus worden geregeld door middel van de grensvlak-geometrie van de macroscopische oppervlaktepatronen op de gefabriceerde oppervlakken. In dit hoofdstuk is daarom een simpel geometrisch model toegevoegd dat kwantitatief reproduceert hoe de wrijvingsweerstand kan worden geregeld met de geometrische oppervlaktepatronen. Een voorbeeld van dit regelen van de wrijvingsweerstand is Kirigami. Kirigami is een oude Japanse kunstvorm waarbij papier door snijden kan worden omgevormd in $3D$-constructies. Voor het onderzoek is gebruikgemaakt van een Kirigami-snijpatroon waarbij door in één richting aan het vel papier te trekken de oppervlakteruwheid kan worden vergroot. We laten zien dat deze externe regeling van de oppervlakteruwheid van een metamateriaaloppervlak als Kirigami het mogelijk maakt de glijweerstand te regelen.

Samenvattend, dit proefschrift geeft nieuwe inzichten in de wrijving van zand, ijs en een reeks kunstmatige oppervlakken waarvan de precieze geometrie kan worden ingesteld. Daarbij blijkt de wrijving afhankelijk van het gedrag van de glijdende grensvlakken op microscopische schaal. De microscopische en macroscopische geometrie van de oppervlakken bepalen samen met (i) de waterfractie van zand, (ii) de temperatuur van ijs en (iii) de (mis)match tussen de oppervlakteruwheden van de oppervlakken de glijweerstand (zie Fig. S.4).

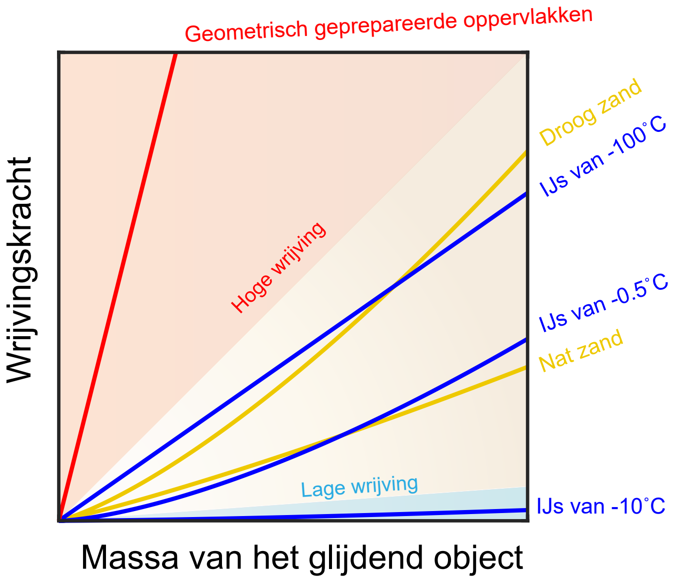

Figure S.4: De wrijvingskracht als functie van de massa van het glijdende object. Dit figuur vat de invloed samen van (i) de waterfractie op de wrijvingskracht van zand, (ii) de temperatuur van ijs op de glibberigheid ervan, en (iii) kunstmatige oppervlakteruwheden op de wrijvingskracht van geometrisch geprepareerde oppervlakken. De lijnen geven de genormaliseerde gemeten data voor zand, ijs en geometrisch geprepareerde oppervlakken weer zoals beschreven in Hoofdstukken 3, 5, en 6. De blauw en rood gekleurde gebieden geven de regimes met lage ($\mu \lesssim 0.07$) en hoge wrijving ($\mu \gtrsim 1$) aan. De lijnen die zijn gemarkeerd met 'Droog zand' en 'Nat zand' geven de gemeten wrijvingskracht voor het schuiven van een halve bol over zand met een waterfractie van respectievelijk $\phi_\mathrm{w} = 0\%$ en $\phi_\mathrm{w} = 8\%$ (zie Fig. 3.2). Bij de lijnen gemarkeerd met 'IJs van -0.5 °C', 'IJs van -10 °C', en 'IJs van -100 °C' is dat de gemeten wrijvingskracht op ijs met de aangegeven temperatuur, van respectievelijk een kleine bol ($R = 0.75$ mm), een grote bol ($R = 6$ mm), en een modelschaats (zie Figuren 5.1 en 5.2). 'Geometrisch geprepareerde oppervlakken' markeert de lijn van de gemeten wrijvingskracht tussen twee glijdende objecten van aluminium met een zaagtand-patroon op het oppervlak ($\theta = 70°$, zie Fig. 6.4).

List of Publications

- R. W. Liefferink, B. Weber, and B. Bonn, "Ploughing friction on wet and dry sand," *Physical Review E*, vol. 98, no. 5, p. 052903, 2018, (Chapter 3)
- R. W. Liefferink, M. Aliasgari, N. Maleki-Jirsaraei, S. Rouhani, and D. Bonn, "Sliding on wet sand," *Granular Matter*, vol. 22, no. 3, p. 1-6, 2020, (Chapter 4)
  R.W.L. and M.A. have contributed equally to this work. M.A. conducted the sliding and hardness experiments, R.W.L. interpreted the data and wrote the manuscript.
- R. W. Liefferink, F. Hsia, B. Weber, and B. Bonn, "Friction on ice: How temperature, pressure, and speed control the slipperiness of ice," *Physical Review X*, vol. 11, no. 1, p. 011025, 2021, (Chapter 5)
- R. W. Liefferink, B. Weber, C. Coulais, and B. Bonn, "Geometrical friction," *In preparation*, (Chapter 6)

Other topics by the author

- M. J. Qazi, R. W. Liefferink, S. J. Schlegel, E. H. Backus, D. Bonn, and N. Shahidzadeh, , "Influence of surfactants on sodium chloride crystallization in confinement," *Langmuir*, vol. 33, no. 17, p. 4260-4268, 2017
- R. W. Liefferink, A. Naillon, D. Bonn, M. Prat, and N. Shahidzadeh, "Single layer porous media with entrapped minerals for microscale studies of multiphase flow," *Lab on a Chip*, vol. 18, no. 7, p. 1094-1104, 2018
- A. Parrenin, R. W. Liefferink, and B. Bonn, "Dry ice hoverboard: Friction reduction by the Leidenfrost effect," *Physical Review E*, vol. 103, no. 2, p. 023002, 2021

Acknowledgements

Writing and finishing my PhD thesis would not have been possible without the help of many colleagues, collaborators, and students along with the support of friends and family. First of all, I would like to thank my three supervisors: Bart, Corentin and Daniel. *Bart*, you always had time for me to discuss and brainstorm. You were always patient and always had new creative ideas, enough ideas to work on for a few weeks. It was a great pleasure working with you. *Corentin*, thank you for your feedback and help from time to time. You often had a fresh perspective on the set goals and I always left meetings with you with new enthusiasm. And last but not least: *Daniel*, it was great working in your research group. You introduced me to many interesting projects and gave me, with the supervision of Bart, the freedom to explore these projects further.

Our work on sand friction, as presented in Chapter 4, was actually started by our collaborators *Mojgan Aliasgari, Nahid Maleki-Jirsaraei* and *Shahin Rouhani*. I was happy to join the project and, although we never actually met, it was a pleasure collaborating on this project.

I also want to thank all bachelor and master students who I worked with in the last 4 years. Especially *Daan* and *Joris* who I, immediately on the first day that I started as PhD-student (and when I was in the middle of moving to a new house), was asked to supervise for their Bachelor projects. It happened a few times that I had to explain an experimental technique which was as much new to me as it was to you guys. More students followed, thank you all for your hard work on the various topics, *Felix, Paul, Kaisa, Sicco, Antoine and Menno.*

During my time in the soft matter group, I have enjoyed the company of many colleagues. *Mohsin*, thank you for the introduction to the research group. I started in September 2015 with a lab project and later my master project under your co-supervision. All questions, lab-related, chemistry related, or just where the group-parties will be, I could ask you. You were always there to help and guide. *Noushine*, my first projects in this research group where together with you as well. It was great working together on the salt crystallization projects. You taught me how to break up the research-goals in small steps and work in an organised way. We also taught several master courses together which I did with great pleasure. Furthermore, I think that we as the 'Christmas committee' organised a few nice evenings with tasty (and way too much) food and drinks. *Thijs*, you always brought the fun in the day. With a bunch of enthusiasm and dedication you always made sure there was beer on Friday for our group or even for the whole institute. I also never had to check when it was lunchtime, you made sure that your office-colleagues always took a break on time and joined together for lunch. You, together with *Bijoy* and *Maureen*, organised many group activities and helped to strengthen the bond in our group. *Antoine*, the one with no No. You were always happy to help and when I had the feeling my results where 'boring' or 'small' you gave a pep-talk to cheer me up. Thank you for the nice (scientific) conversations and biking trips together. I admire your enthusiasm for science, and I think we will hear much more from you, the upcoming prof. Deblais. *Heleen*, when you joined our office you brought in a bunch of energy. In only a few weeks it felt like we knew each other for years, it was great to start the day with a coffee and discuss (and complain) about all small and big things in life. *Marion*, thank you for the great time together. I could always interrupt you from your writing for advice, even the most basics question about photography your answered me patiently. And I'm sorry that in coronatime you several times had the bad luck to have to clean up my messy desk and cupboard in the office because I was not around. I am very grateful to the supporting staff who helped with building (and repairing) my experimental setups. Thank you *Daan*, *Fred*, and *Sven* for all the help you gave, from just a small part of equipment up to brand new and custom-made setups. *Carlos* and *Paul*, thank you for the guidance in lab and making sure that we students don't make too much mess in lab. And Paul, I will never forget the minutes locked together in a walk-in freezer at −20 °C. My gratitude also goes out to all the other colleagues, *Riande, Feng-Chun, Luci, Rozeline, Kasra, David, Andreas, Dina, Hans, Stefan, Rick, Henri, Fiona, Cyrian, Emanuele, Bruce, Etienne, Guillaume, Piet, Janne-Mieke, Marius, Bastiaan, the Dutch Simon, the French Simon, Antoine the second, Antoine the third, Henri, Roland, Menno, Thomas, Martin*, and all other members. Thank you for the great time and support.

Finally, I want to thank all my friends and family who directly and indirectly gave me the support needed to write my thesis. My oldest friends, *Arwin* and *Shaja*, and all friends in Utrecht: *Tim, Stan, Ties, Jan, Erik, Bram* and all the men from *Nobiscum*. Furthermore, I would like to thank *Ruben, Carlijn, Thijs, Guus, Lotte, Cedric*, and *Marina* for all the relaxing evenings we had and board games we played. It was a

welcome distraction from the working days. *Vera*, thank you for helping me out with designing the cover. *Julia, Jan, Aleida, Jorin, Daniël, Sandra, Bauke, Mieke* and *Nienke*, thank you for being a great family. And of course my father, for being the great father you were. You all gave me space and time to develop and search for my own path. Finally, *Hester*, I don't even know where to begin to express my gratitude to you. Your support, patience, and love throughout this journey has been the best help I could have. You know how to calm me down when I am stressed and to cheer me up when I am down. You also were a great officemate for the last year of my PhD! But most important, you make me happy.